CHAOS IN QUANTUM OPTICS

J.R. ACKERHALT

Theoretical Division (T-12), Los Alamos National Laboratory, Los Alamos, New Mexico 87545, U.S.A.

and

P.W. MILONNI and M.-L. SHIH

Department of Physics, University of Arkansas, Fayetteville, Arkansas 72701, U.S.A.

NORTH-HOLLAND–AMSTERDAM

PHYSICS REPORTS (Review Section of Physics Letters) 128, Nos. 4 & 5 (1985) 205–300. North-Holland, Amsterdam

CHAOS IN QUANTUM OPTICS

J.R. ACKERHALT

Theoretical Division (T-12), Los Alamos National Laboratory, Los Alamos, New Mexico 87545, U.S.A.

and

P.W. MILONNI and M.-L. SHIH

Department of Physics, University of Arkansas, Fayetteville, Arkansas 72701, U.S.A.

Received November 1984

Contents:

Abstract:

We describe how chaotic dynamics may appear in some fundamental as well as practical problems of quantum optics. This essay is intended for researchers in the general areas of quantum optics and laser physics, especially those unfamiliar with the basic ideas and implications of "chaos". Our aim is to describe what chaos is, how it may be identified, and why it may be important. We suggest that quantum optics offers an attractive arena for the study of chaotic behavior. To support this suggestion we consider several examples involving Maxwell–Bloch equations, lasers, nonlinear optics, and infrared laser–molecule interactions.

1. Introduction

A very active area of research in physics these days comes under the general heading of "chaos". What this rubric is meant to imply is a more or less random type of behavior in a system described by completely *deterministic* equations of motion (a *dynamical system*). From a practical standpoint the study of chaotic dynamics reflects in part the influence of computers on theoretical physics, for chaotic systems are "nonintegrable", and much of the work in the field involves numerical "experiments". In the grander scheme of things, chaotic dynamics may herald a "new paradigm, a turning point in science" [1].

A glance at the table of contents reveals that this review focuses on a modest collection of examples of chaotic behavior. Specifically, we consider examples in quantum optics and quantum electronics. We believe that researchers in these fields can benefit from some appreciation of what "chaos" is, and this review is written with their needs in mind. It is only peripherally that we discuss various implications of chaotic dynamics in a more general context, in order to provide some indication of why this field is attracting so much general interest among physicists.

Lasers have in several instances been used to test general and fundamental ideas in physics, particularly in statistical mechanics. They may play an equally valuable role in chaotic dynamics, and indeed some observations of chaotic behavior in lasers have recently been reported (section 4). Observations of chaotic behavior have also been made in optically bistable devices (section 5). We emphasize throughout this review that chaos is not an exotic mathematical curiosity, but that it appears in some quite fundamental problems in laser physics and quantum optics.

A general overview of chaos is given in the following section, and the ideas are illustrated with several examples. In section 3 we consider the model of a single-mode field interacting with a collection of two-level atoms, and show that this apparently "simple" model can exhibit chaotic dynamics. Chaos in lasers and nonlinear optics is discussed in sections 4 and 5, respectively, where we describe some results that have been reported by various experimenters. In section 6 we discuss the interesting possibility that chaos, rather than "order", is a prevailing feature of multiple-photon laser–molecule interactions.

We should emphasize at the outset that the literature on chaos is expanding so rapidly that no review at this time is likely to be "complete". Furthermore our own interests are in the general area of quantum optics, and so we apologize in advance to the many authors, either in other fields or on the more mathematical side of chaos, whose work we have not cited.

2. Overview of chaotic dynamics

2.1. Introduction

We will be concerned mainly with chaotic evolution of dynamical systems of differential equations.

However, to introduce some basic ideas it is simpler to begin with discrete mappings. In addition to being easier to work with, discrete mappings can be constructed from systems of differential equations in various ways. For instance, use is frequently made of *Poincaré maps*. For many purposes one might just as well concentrate on discrete mappings rather than "continuous flows". We will begin with two celebrated examples, the logistic and Hénon mappings.

2.2. The logistic mapping

A simple model for the rate of change of some population x is based on the logistic equation, $\dot{x} = Bx - Dx^2$, if the death rate is assumed to vary linearly with the population. Sometimes such a rate equation is replaced by a discrete mapping, $x_{n+1} = f(x_n)$, which is assumed to relate the populations of successive generations. Such a discrete-time variant of the logistic equation is the *logistic mapping* [2–5]

$$x_{n+1} = 4\lambda x_n(1 - x_n), \qquad 0 \le x_0, \quad \lambda \le 1 \tag{2.2.1}$$

which is a noninvertible (because x_{n-1} is not uniquely determined by x_n) mapping of the interval [0, 1] into itself. An important role is played by the parameter λ; for certain values of this "knob", the sequence $\{x_n\}$ is "orderly", for others it is chaotic.

Consider the case $\lambda = 1$. Letting $x_n = \sin^2 \theta_n$, we have from (2.2.1) $\sin^2 \theta_{n+1} = \sin^2 2\theta_n$, or $\theta_{n+1} = 2\theta_n$ (mod $\pi/2$). In this case, therefore, the logistic mapping reduces to

$$\theta_n = 2^n \theta_0 . \tag{2.2.2}$$

In this form it is easy to see that the sequence of numbers generated by the map is very sensitive to the value of the initial seed value θ_0. If $\theta_0 \to \theta_0 + \varepsilon_0$, then $\theta_n \to \theta_n + \varepsilon_n$, where

$$\varepsilon_n = 2^n \varepsilon_0 = \varepsilon_0 \, e^{n(\log 2)} . \tag{2.2.3}$$

The deviation ε_n thus grows exponentially at the rate log 2, which may be called the *Lyapunov exponent*. Since the Lyapunov exponent in this case is positive, the sequence generated by the logistic map is very sensitive to the choice of the initial seed. This *very sensitive dependence on initial conditions* is a hallmark of chaos. Thus the sequence $\{x_n\}$ generated by the logistic map for $\lambda = 1$ is "chaotic" rather than "orderly".

When $\lambda \le 1$ we have $x_n + \varepsilon_n = f^n(x_0 + \varepsilon_0)$, where f^n is the nth iterate of f, i.e., $x_1 = f(x_0) \equiv f^1(x_0)$, $x_2 = f(x_1) = f(f(x_0)) \equiv f^2(x_0)$, etc. Thus

$$x_n + \varepsilon_n \cong f^n(x_0) + \varepsilon_0 f^{n\prime}(x_0) = x_n + \varepsilon_0 f^{n\prime}(x_0) \tag{2.2.4}$$

or $\varepsilon_n = \varepsilon_0 f^{n\prime}(x_0)$, where $f^{n\prime} = \mathrm{d}f^n/\mathrm{d}x$. From the chain rule for derivatives it follows that

$$f^{n\prime}(x_0) = \prod_{i=0}^{n-1} f'(x_i) \tag{2.2.5}$$

and therefore

$$|\varepsilon_n| = |\varepsilon_0| \prod_{i=0}^{n-1} f'(x_i) = |\varepsilon_0| \, e^{n\chi_n} \tag{2.2.6}$$

where

$$\chi_n = \frac{1}{n} \sum_{i=0}^{n-1} \log |f'(x_i)| . \tag{2.2.7}$$

The limit

$$\chi = \lim_{n\to\infty} \chi_n = \lim_{n\to\infty} \frac{1}{n} \sum_{i=0}^{n-1} \log |f'(x_i)| \tag{2.2.8}$$

defines the *Lyapunov characteristic exponent* (*LCE*) of the map. A numerical computation for the logistic mapping with $\lambda = 1$ gives $\chi = \log 2$, in agreement with (2.2.3). If $\chi > 0$ we have very sensitive dependence on initial conditions. For the logistic map with $\lambda = 1$, for instance, we have exponential growth of the deviations ε_n for almost every x_0, i.e., we have a chaotic sequence. Lyapunov characteristic exponents are defined for general dynamical systems, and a positive LCE is a signature of chaotic evolution.

It is found empirically that the limit (2.2.7) exists and is independent of x_0. In the general case the ordinary limit may not exist, and χ should be defined as a limit superior (lim sup). Figure 2.1 shows the result of the computation (2.2.8) for $\lambda = 0.95$, using three different values of x_0. χ has been plotted as a function of λ by Huberman and Rudnick [6].

A closely related characteristic of chaotic systems is the absence of any truly periodic behavior. This has been studied in detail for the case of the logistic map [2–5]. A brief summary is nevertheless essential for our purposes.

The *fixed points* x^* of the mapping $x_{n+1} = f(x_n)$ are defined by $x^* = f(x^*)$. For the logistic map we have the two fixed points, $x_0^* = 0$ and $x_1^* = 1 - 1/4\lambda$. It is important to know whether a fixed point is *stable* against a small perturbation; following the same approach used above, we conclude that x^* is a

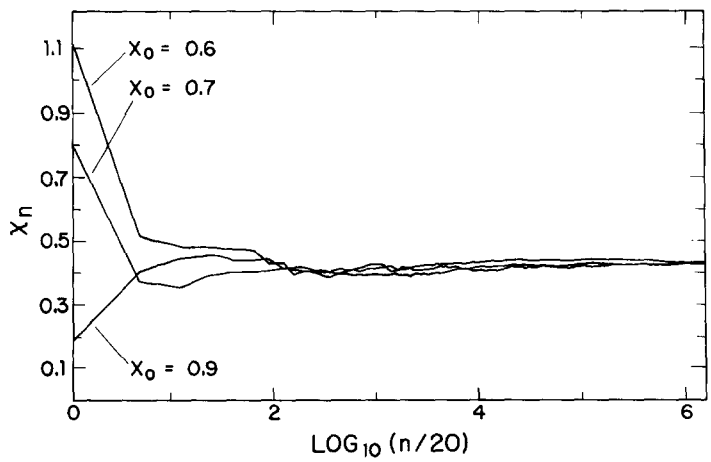

Fig. 2.1. Computation of the Lyapunov characteristic exponent (2.2.8) for the logistic mapping.

stable fixed point if $|f'(x^*)|<1$, an unstable fixed point if $|f'(x^*)|>1$, and a "marginally stable" fixed point if $|f'(x^*)|=1$.

For the logistic map, we deduce from this stability criterion that for $0<\lambda<\frac{1}{4}$ the only fixed point is $x_0^*=0$, and it is stable. Whatever the seed value x_0, we eventually settle on x_0^* after successive iterations of the map; x_0^* is therefore called an *attractor* of period one, or a *one-cycle*. For $\frac{1}{4}<\lambda<\frac{3}{4}$, x_0^* is unstable, but the fixed point x_1^* is stable. For $\lambda>\frac{3}{4}$, however, both fixed points are unstable. The reader who has not already done so may enjoy checking these properties with a programmable pocket calculator.

Just beyond $\lambda=\Lambda_1=\frac{3}{4}$, there appear two stable fixed points, x_2^* and x_3^*, of f^2. After initial "transients", successive iterates x_n bounce to and fro between these fixed points of f^2, so we now have an attractor of period two, or a two-cycle. A *period doubling*, from a one-cycle for $\lambda<\Lambda_1$ to a two-cycle for $\lambda\geq\Lambda_1$, has occurred by "turning the λ knob". The two fixed points of f^2 are stable until λ is increased to $\Lambda_2=\frac{1}{4}(1+\sqrt{6})=0.862372\ldots$, where another period-doubling *bifurcation* occurs, and we then have a four-cycle a, b, c, d, a, b, c, d,... As λ is increased further we continue to see period doublings, and the "window" of λ values associated with a given n-cycle gets rapidly narrower with increasing n. Feigenbaum [3, 4], by a combination of functional and numerical analysis, has established that the sequence $\{\Lambda_n\}$ of λ values, at which period doublings occur, converges geometrically at a rate given by

$$\lim_{n\to\infty}\frac{\Lambda_n-\Lambda_{n-1}}{\Lambda_{n+1}-\Lambda_n}=\delta=4.6692016091\ldots \tag{2.2.9}$$

Feigenbaum's constant δ is universal in the sense that (2.2.9) applies to all maps with quadratic maxima, such as the logistic map or the map $x_{n+1}=\lambda\sin\pi x_n$. The sequence $\{\Lambda_n\}$ has a limit point $\lambda^*=0.892\ldots$ Beyond this value of the "knob", the sequence $\{x_n\}$ appears to be a *chaotic* sequence without a periodic attractor, except for certain "windows" of λ values. The period has doubled *ad infinitum*. Feigenbaum's discovery stimulated a lot of interest because it uncovered a quantitative universality in a *period-doubling route to chaos.*

Thus far we have referred to chaotic behavior in terms of (1) a positive LCE implying very sensitive dependence on initial conditions, and (2) the absence of any periodicity. These two properties are closely related. Suppose, for instance, that λ is such that there does exist a stable n-cycle. Then there are n stable fixed points x_i^*, $i=1,2,\ldots,n$, of f^n, so that $|f^{n\prime}(x_i^*)|<1$, and

$$\begin{aligned}\chi&=\lim_{m\to\infty}\frac{1}{m}\log\prod_{i=1}^{m}|f'(x_i)|\\&=\lim_{m\to\infty}\frac{1}{m}\log\Bigl(\prod_{i=1}^{n}|f'(x_i)|\Bigr)^{m/n}=\frac{1}{n}\log|f^{n\prime}(x_i^*)|<0\,.\end{aligned} \tag{2.2.10}$$

It therefore follows also that a positive LCE implies the absence of any n-cycle. The converse need not be true; aperiodicity does not necessarily imply very sensitive dependence on initial conditions.

Throughout this review we will refer to a dynamical system having properties (1) and (2) above as *chaotic.*

We have mentioned that periodic windows appear in the chaotic regime $\lambda>\lambda^*$ of the logistic mapping. When an n-cycle is found, it is possible to infer the existence (but not the stability) of other

cycles [7–9]. Define the ordered sets $\{2^0 \cdot 3, 2^0 \cdot 5, 2^0 \cdot 7, \ldots 2^1 \cdot 3, 2^1 \cdot 5, 2^1 \cdot 7, \ldots 2^2 \cdot 3, 2^2 \cdot 5, 2^2 \cdot 7, \ldots = 3, 5, 7, \ldots 6, 10, 14, \ldots 12, 20, 28, \ldots\}$ and $\{\ldots, 32, 16, 8, 4, 2, 1\}$. Šarkovskii's theorem [7–9] says that if a continuous unimodal mapping f on an interval of the real line has an n-cycle, then it has an m-cycle for every m such that $n \Leftarrow m$ in the ordering $3 \Leftarrow 5 \Leftarrow 7 \ldots 6 \Leftarrow 10 \Leftarrow 14 \ldots 12 \Leftarrow 20 \Leftarrow 28 \ldots 32 \Leftarrow 16 \Leftarrow 8 \Leftarrow 4 \Leftarrow 2 \Leftarrow 1$. In particular, a 3-cycle implies the existence of *all* n-cycles, including aperiodic sequences associated with period doubling *ad infinitum*. That is, "Period Three Implies Chaos" [9].

Let us return to the case $\lambda = 1$. The sequence $\{x_n\}$ in this case is known to be dense in the interval $[0, 1]$, i.e., it passes arbitrarily close to any point on the interval for almost every x_0 [10]. The fact that the sequence is chaotic, with very sensitive dependence on x_0, means that all memory of the initial seed is eventually lost; an effectively "random" behavior is present even though the mapping itself is perfectly deterministic. However, we can be sure of the way the sequence of iterates is distributed over the interval: Defining a "probability" distribution $P(x)$ such that $P(x)\,dx$ is the relative number of terms appearing in the interval $[0, 1]$, and noting that for large n the θ_n are uniformly distributed on $[0, \pi/2]$, we write $P(x)\,dx = (2/\pi)\,d\theta$, and therefore, since $x = \sin^2\theta$,

$$P(x) = \frac{1/\pi}{\sqrt{x - x^2}}. \tag{2.2.11}$$

Such a probability distribution for a chaotic system would frequently be of interest in physical applications. Unfortunately the logistic map with $\lambda = 1$ is a very special case of a chaotic system; in general it is not known how to determine such probability distributions without numerical "experiments".

There is another universal Feigenbaum constant (denoted α) for maps with quadratic maxima [3–5]. Since we will not discuss this aspect of the logistic map, we refer the interested reader to Feigenbaum's papers. There one can find general conditions on f leading to a period-doubling route to chaos.

2.3. The Hénon mapping

The Hénon mapping is "A Two-Dimensional Mapping with a Strange Attractor" [11]. It has the form

$$\begin{aligned} x_{n+1} &= y_n + 1 - ax_n^2 \\ y_{n+1} &= bx_n \end{aligned} \tag{2.3.1}$$

where a, b are constants, $a > 0$ and $0 < b < 1$. Unlike (2.2.1), the Hénon map is invertible, i.e., x_{n+1}, y_{n+1} determine x_n, y_n uniquely. It has the fixed points $x_\pm^*$, $y_\pm^* = bx_\pm^*$, where

$$x_\pm^* = \frac{1}{2a}\{-(1-b) \pm [(1-b)^2 + 4a]^{1/2}\}. \tag{2.3.2}$$

By proceeding in the same way as for the logistic map, it is found that the fixed point (x_-^*, bx_-^*) is always unstable, whereas (x_+^*, bx_+^*) is unstable if $a > \frac{3}{4}(1-b)^2$.

We will focus our attention on the case $b = 0.3$ [11]. The sequence of points $\{x_n, y_n\}$ generated by (2.3.1) settles onto an attractor or diverges to infinity, depending on the initial seed (x_0, y_0). (The set of

all points (x_0, y_0) for which the sequence $\{x_n, y_n\}$ converges onto an attractor may be called the *basin of attraction* of that attractor.)

For $b = 0.3$, both fixed points of (2.3.1) are unstable when $a > a_1 = 0.3675$. Beyond this value of a the situation is analogous to that for the logistic map with $\lambda > \Lambda_1$. At a_1 a two-cycle (or attractor of period two) is born. Then at $a = a_2 = 0.9125$ this attractor becomes unstable, and a stable four-cycle is born. Successive period-doubling bifurcations are found as a is further increased and, remarkably, the sequence $\{a_n\}$ of a values at which a 2^n-cycle is born converges geometrically at the universal Feigenbaum rate (2.2.9). This is seen from the "experimental" results of table 2.1, following Derrida et al. [12].

The Jacobian of the transformation (2.3.1) is

$$\frac{\partial(x_{n+1}, y_{n+1})}{\partial(x_n, y_n)} = \begin{vmatrix} -2ax_n & 1 \\ b & 0 \end{vmatrix} = -b. \tag{2.3.3}$$

For $b = 0.3$ the map (2.3.1) is therefore area-contracting, i.e., the modulus of the Jacobian determinant is less than unity. The attractors of the map therefore have zero area. With this in mind it is perhaps a little less surprising that the (two-dimensional) Hénon map can undergo the same kind of period-doubling sequence, governed by Feigenbaum's δ, as the one-dimensional logistic map [12].

Because it is a two-dimensional mapping, the Hénon map has two characteristic Lyapunov exponents. These are defined by proceeding along the same lines as for the logistic map. Let $x_0 \to x_0 + \varepsilon_0$, $y_0 \to y_0 + \delta_0$. Then $x_1 \to x_1 + \varepsilon_1$ and $y_1 \to y_1 + \delta_1$, where for small ε_0, δ_0

$$\begin{pmatrix} \varepsilon_1 \\ \delta_1 \end{pmatrix} = J(x_0, y_0) \begin{pmatrix} \varepsilon_0 \\ \delta_0 \end{pmatrix} \tag{2.3.4}$$

and the Jacobian matrix

$$J(x, y) = \begin{pmatrix} \partial f/\partial x & \partial f/\partial y \\ \partial g/\partial x & \partial g/\partial y \end{pmatrix}. \tag{2.3.5}$$

Table 2.1
Values of a at which period-doubling bifurcations occur in the Hénon map with $b = 0.3$

Period (2^n)	a_n	$(a_n - a_{n-1})/(a_{n+1} - a_n)$
2	0.3675	
4	0.9125	4.844
8	1.026	4.3269
16	1.051	4.696
32	1.056536	4.636
64	1.05773083	4.7748
128	1.0579808931	4.6696
256	1.05803445215	4.6691

After n interations the perturbations ε_n, δ_n are similarly

$$\begin{pmatrix} \varepsilon_n \\ \delta_n \end{pmatrix} = J(n) \begin{pmatrix} \varepsilon_0 \\ \delta_0 \end{pmatrix} \tag{2.3.6}$$

where $J(n) = J(x_{n-1}, y_{n-1})\, J(x_{n-2}, y_{n-2}) \cdots J(x_0, y_0)$. In a coordinate system in which $J(n)$ is diagonal we have

$$|\varepsilon_n'| = |\lambda_1(n)\, \varepsilon_0| = |\varepsilon_0| \exp(n\chi_n^{(1)}) \tag{2.3.7}$$

$$|\delta_n'| = |\lambda_2(n)\, \delta_0| = |\delta_0| \exp(n\chi_n^{(2)}) \tag{2.3.8}$$

where $\lambda_1(n)$, $\lambda_2(n)$ are the eigenvalues of $J(n)$. The limits [13, 14]

$$\lambda^{(1,2)} = \lim_{n\to\infty} [\text{magnitude of eigenvalues of } J(n)]^{1/n} \tag{2.3.9}$$

are called the Lyapunov numbers of the mapping, and

$$\chi^{(1,2)} = \log \lambda^{(1,2)} \tag{2.3.10}$$

are the Lyapunov characteristic exponents.

Computations for the Hénon map with $a = 1.4$, $b = 0.3$ yield $\lambda^{(1)} \cong 1.52$, $\lambda^{(2)} \cong 0.197$, $\chi^{(1)} \cong 0.42$, $\chi^{(2)} \cong -1.62$. Mathematical aspects of the LCE for the Hénon map, and numerical results for a range of a, b values, have been described by Feit [15].

The fact that one of the LCE is positive in this example means that in a certain direction the mapping is "stretching", i.e., there is very sensitive dependence on initial conditions. If there is stretching in some directions and contraction (negative LCE) in others, as in this example, we have a situation called *hyperbolicity*. The directions associated with the positive LCE are inside the attractor, the other directions being contracting directions. For our purposes it is sufficient to recognize that there need only be *one* stretching direction for the system to be chaotic (very sensitive dependence on initial conditions). That is, a dynamical system may be regarded as chaotic if there is at least one positive LCE.

The largest LCE is generally much easier to compute than the full spectrum of exponents. Suppose we introduce small perturbations ε_0, δ_0 and proceed to solve (2.3.1) and (2.3.6) simultaneously, computing along the way the quantity

$$\alpha(n) = \frac{1}{n} \log [\varepsilon_n^2 + \delta_n^2]^{1/2}. \tag{2.3.11}$$

For large n this is equivalent to

$$\alpha(n) = \frac{1}{n} \log |\varepsilon_n'| = \chi_n^{(1)}, \tag{2.3.12}$$

since only the stretching direction survives the large-n limit. Thus $\lim_{n\to\infty} \alpha(n)$ gives the largest LCE.

The procedure based on (2.3.11) is much simpler to use than (2.3.10), as it does not require finding eigenvalues. It may be extended to N-dimensional systems. We will see later that an analogous approach may be used to find the largest LCE for a system of differential equations.

We will loosely refer to a chaotic attractor, having the property of hyperbolicity, as a *strange attractor.* Strange attractors have a sort of "structure within structure", or "self-similarity", that is frequently the reason (but not the original reason) for calling them strange. Figure 2.2 shows the Hénon (chaotic) attractor for $a = 1.4$, $b = 0.3$. The structure within structure is seen by expanding the scale, looking in finer and finer detail at the attractor, as in fig. 2.3.

It is interesting that, because the map is area-contracting, the attracting set shown in fig. 2.2 must have zero area. However, the dimension of the attractor is not zero or one, as it would be for an obvious zero-area set in the plane (e.g., a point or a curve). In fact the attractor is closely akin to what Mandelbrot calls a *fractal* [16]. To briefly motivate this idea, consider that a unit cube contains $N(\varepsilon) = \varepsilon^{-3}$ cubes of side ε, a unit square contains $N(\varepsilon) = \varepsilon^{-2}$ squares of side ε, and a unit line segment contains $N(\varepsilon) = \varepsilon^{-1}$ segments of side ε; in each case the dimension of the object is $d = \log N(\varepsilon)/\log(1/\varepsilon)$. We define the fractal dimension, or (loosely) *Hausdorff dimension,* as

$$d = \lim_{\varepsilon \to 0} \frac{\log N(\varepsilon)}{\log (1/\varepsilon)}. \tag{2.3.13}$$

(This is only one of a variety of possible definitions of dimension. To be more precise, we might call d a "capacity".) The definition applies to an n-dimensional space as well, if we take $N(\varepsilon)$ to be the number of n-dimensional hypercubes of side ε needed to cover the object. A fractal may be considered to be an object having nonintegral Hausdorff dimension. The strange attractor of figs. 2.2 and 2.3 is a fractal of

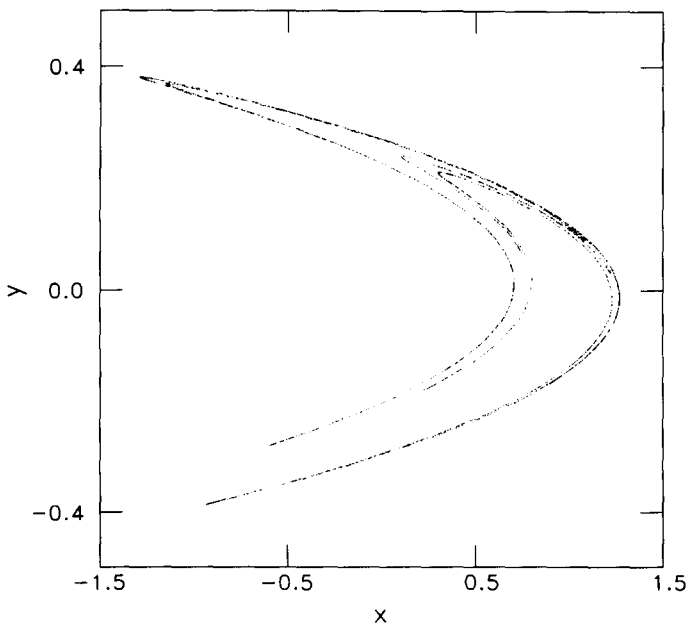

Fig. 2.2. The Hénon attractor for $a = 1.4$, $b = 0.3$.

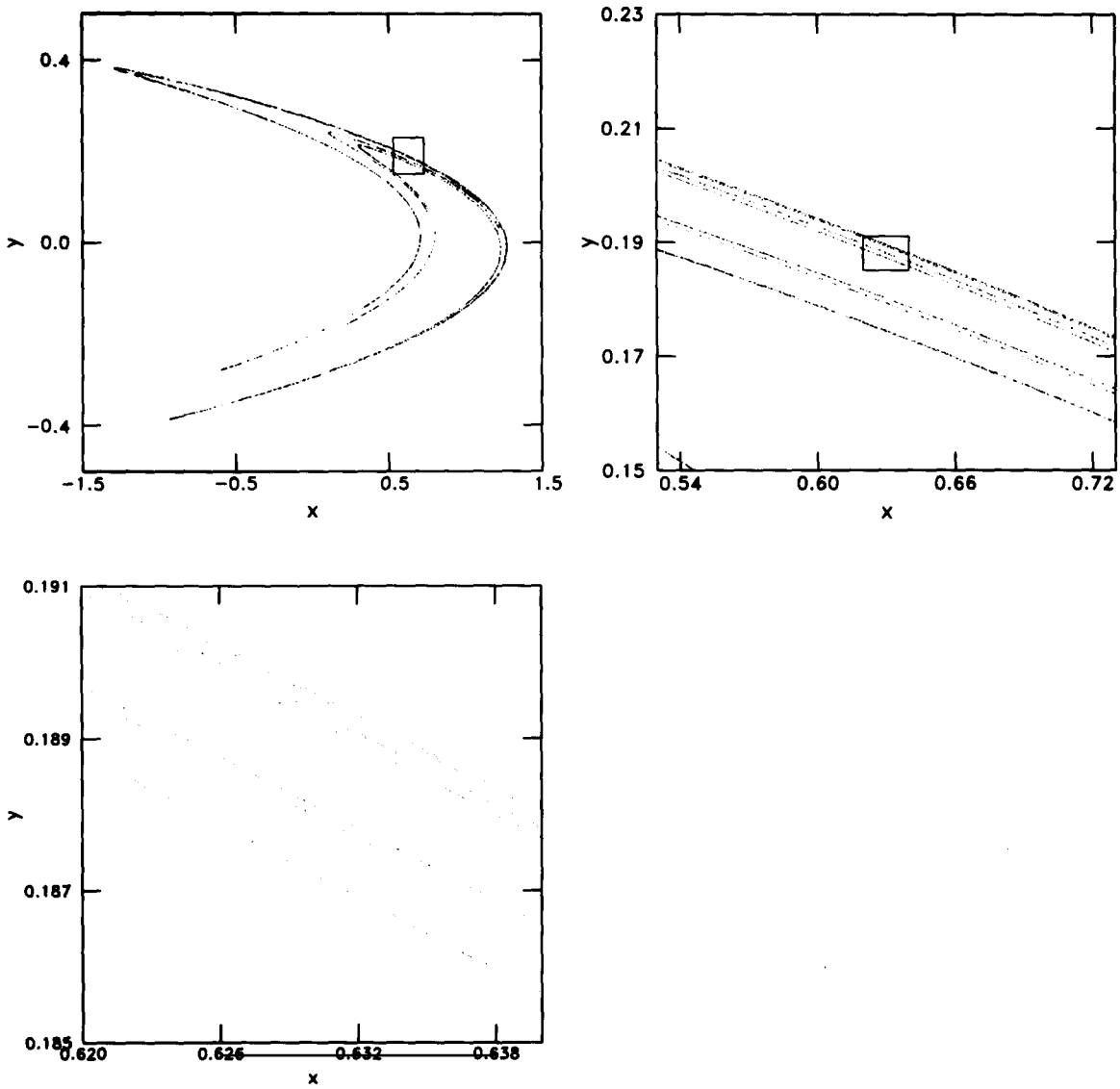

Fig. 2.3. Structure within structure of the Hénon attractor, obtained by expanding the scale of fig. 2.2.

dimension $d \cong 1.26$ [13]. (Mandelbrot [16] defines a fractal as a set having a "fractal" dimension greater than its "topological" dimension.)

A famous example of a set with fractional Hausdorff dimension, and "structure within structure", is the *Cantor set*, which may be defined by the following construction: Divide the line segment [0, 1] into thirds and remove the middle (open) third. Do the same with the remaining two segments, and continue the process of removing middle thirds. The set obtained by continuing the process *ad infinitum* is the Cantor set. It has a number of illustrative mathematical properties; for instance, it is nondenumerable but has measure zero. Using line segments of side $\varepsilon = (1/3)^m$, with $N(\varepsilon) = 2^m$, it follows from (2.3.5) that the Hausdorff dimension of the Cantor set is log 2/log 3. The Hénon strange attractor, with its fractal dimensionality, has a transverse Cantor-like structure. (In general it is very difficult to *prove* that

an attractor is strange. We use "strange attractor" and "chaotic attractor" synonymously, and base our discussions on numerical *evidence* rather than rigorous proofs.) *A chaotic attractor can be simultaneously hyperbolic and of zero-volume because it has a structure within structure, or ribbon-like aspect, that keeps the motion bounded but allows exponential divergence of initially close trajectories.*

2.4. Dynamical systems of differential equations

We now turn our attention to a different type of (deterministic) dynamical system, namely a set of ordinary differential equations. Once again we will have periodic or aperiodic behavior, the latter being chaotic when the system has a positive LCE. Just as the logistic and Hénon maps have become "standard" examples of chaos in one- and two-dimensional mappings, there is a standard example of chaos in systems of ordinary differential equations. This is the *Lorenz model*, which was discussed by Lorenz in 1963 [17]. The Lorenz model has a rich variety of behaviors, and has been the subject of many papers and at least one monograph [18]. Before discussing the Lorenz model, let us quickly review some pertinent features of ordinary differential equations in general.

By solving for the independent variable t in terms of the dependent variables and their derivatives, we can (in principle) write any ordinary differential equation (ODE) as an autonomous one of one higher order. ("Autonomous" means there is no explicit t dependence.) Further, by letting $y_1 = y$, $y_2 = \dot{y}$, $y_3 = \ddot{y}, \ldots$ we can write an autonomous ODE of order N in the form of N first-order autonomous ODE:

$$\dot{y}_n = F_n(y_1, y_2, \ldots y_N), \qquad n = 1, 2, 3, \ldots N. \tag{2.4.1}$$

F_n and $\partial F_n/\partial y_m$ are assumed to be bounded, continuous functions of their arguments. The existence and uniqueness theorem for differential equations is therefore applicable.

We regard the system (2.4.1) as giving the motion of a point in the N-dimensional *phase space* $(y_1, y_2, \ldots y_N)$. This motion is called a *trajectory*. The uniqueness theorem for (2.4.1) guarantees that trajectories associated with different initial conditions cannot intersect. We will only be interested in systems having bounded trajectories in phase space.

Hamiltonian systems are a special case of (2.4.1) in which there exists a function $H(q_1, q_2, \ldots q_m; p_1, p_2, \ldots p_m)$ such that

$$\dot{q}_i = \partial H/\partial p_i \qquad \text{and} \qquad \dot{p}_i = -\partial H/\partial q_i . \tag{2.4.2}$$

In this case the phase space is the usual $2m$-dimensional phase space of classical Hamiltonian mechanics.

We will also be concerned with dissipative systems where, in contrast to Liouville's theorem for Hamiltonian systems, the time evolution of our dynamical system *contracts* volume in phase space. The dissipation arises physically as a result of spontaneous emission, collisional damping, lossy cavities, etc. Even though we deal *fundamentally* with Hamiltonian systems, we restrict our attention to an interesting subsystem and regard everything else as a sink into which the subsystem can irreversibly decay. The dynamics of our subsystem is then non-Hamiltonian.

Just as in the case of discrete mappings, it is convenient to define *fixed points* of the dynamical system (2.4.1). (These are also called critical points or equilibrium points.) These are points $(y_1^*, y_2^*, \ldots y_N^*)$ of phase space for which

$$F_n(y_1^*, y_2^*, \ldots y_N^*) = 0 \qquad \text{for all } n \tag{2.4.3}$$

or in other words the points where all $\dot{y}_n = 0$. Also as in the case of discrete maps, it is useful to know whether the fixed points are stable against small perturbations. This may usually be determined by linearizing about the fixed points.

If trajectories in the neighborhood of a stable fixed point are closed loops, the fixed point is called a *center.* For instance, the equilibrium point of a simple (undamped) harmonic oscillator is a center, the closed loops being just the circles $p^2 + q^2 =$ constant in the phase plane. In fact stable fixed points of Hamiltonian systems are always centers. If all the trajectories in the neighborhood of a stable fixed point approach it along curves which are asymptotically straight lines, the fixed point is called a *stable node*; if neighboring trajectories spiral into the fixed point it is called a *stable spiral point.* If we displace a system away from a stable node or spiral point by a small amount, it will return to the equilibrium point. If the stable equilibrium point is a center, however, the system will remain *near* to it. Similarly we can classify unstable fixed points as unstable nodes, unstable spiral points, or saddle points.

Stable nodes and spiral points are simple examples of attractors. Another important example of an attractor is a stable *limit cycle.* A limit cycle is a closed, periodic trajectory, "isolated" in the sense that no nearby trajectory is also closed. (The closed loops of the harmonic oscillator, for instance, are obviously not isolated.) In numerical computations we find a limit cycle as a periodic motion a nonlinear system settles into after initial transients die out; after the transients decay we are *on* the attractor. The periodicity of the motion implies that the trajectory in phase space is a closed loop.

Limit cycles, which arise only in dissipative *nonlinear* systems, are of great practical importance [19, 20]. Within its "basin of attraction" in phase space a stable limit cycle, like a stable node or spiral point, is independent of initial conditions and is determined by the *parameters* in the equations.

In some physical applications it is not difficult to understand the appearance of a limit cycle as a balance between "self-excitation" and damping. An example is provided by the pendulum clock. Here the anchor clip controlling the rotation of the escape wheel also delivers periodic impulses to the pendulum bob. The damping of the pendulum's oscillations in turn increases with increasing oscillation amplitude, and an equilibrium situation is reached. This limit cycle is independent of the starting impulse and is stable against small perturbations (as occur, for instance, when the clock is moved from one place to another).

Another example is provided by the van der Pol equation [20]

$$\ddot{x} + b(x^2 - 1)\dot{x} + x = 0\,, \qquad b > 0\,. \tag{2.4.4}$$

Here there is positive damping when $|x| > 1$, negative damping when $|x| < 1$. Equation (2.4.4) is equivalent to $\dot{y}_1 = y_2$, $\dot{y}_2 = -b(y_1^2 - 1)y_2 - y_1$. There is one fixed point, $(y_1^*, y_2^*) = 0$, and a linear stability analysis shows that this fixed point is an unstable spiral point. Trajectories in the phase space $(y_1, y_2) = (x, \dot{x})$ near the origin therefore spiral outward, but for $|x| > 1$ there is positive damping. What happens when (2.4.4) is integrated is that a limit cycle is reached as a balance between positive and negative damping. Figure 2.4 shows the trajectory in the phase plane, starting out with initial conditions inside the limit-cycle loop. The limit cycle is obtained for arbitrary initial conditions.

A stable limit cycle should be thought of as an equilibrium state of oscillation of a nonlinear system, just as a stable fixed point represents a stationary equilibrium. Unfortunately, mathematicians at present cannot tell us in general whether a limit cycle exists in a given system, although some definite statements can be made for systems whose phase space is the plane ($N = 2$ in (2.4.1)). For instance,

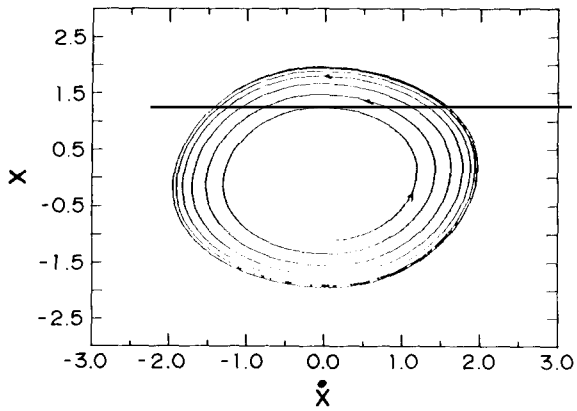

Fig. 2.4. The van der Pol limit cycle obtained by numerical integration of (2.4.4).

Bendixson's Negative Criterion states that if $\partial F_1/\partial y_1 + \partial F_2/\partial y_2$ is of one sign in a simply-connected ("no holes") domain, there are no closed loops. And it is known that a limit-cycle closed loop cannot enclose a region containing no fixed points.

The system (2.4.1) is "chaotic" if it has the property of very sensitive dependence on initial conditions. (We of course exclude systems like $\dot{y}_1 = y_1$, which have a trivial sort of sensitive dependence on initial conditions because the motion is unbounded; we are only interested in bounded trajectories in phase space.) A chaotic system will be nonperiodic. This leads us to the conclusion that systems of the form (2.4.1) with $N \leq 2$ cannot be chaotic. If $N = 1$, for instance, the noncrossing of trajectories severely restricts the motion on the "phase line": The trajectory can be a fixed point, it can approach a fixed point as $t \to \infty$, or it goes to $\pm\infty$ as $t \to \infty$; there are no other possibilities when $N = 1$ if trajectories cannot intersect. If $N = 2$ the Poincaré–Bendixson theorem says that a bounded trajectory can either approach a fixed point as $t \to \infty$ or a closed curve, which may be a limit cycle. Fixed points and closed curves represent regular (periodic) behavior, and so for a system (2.4.1) to have chaotic behavior we must have $N > 2$. The restriction that trajectories do not cross precludes any possibility of chaos for $N = 1$ or 2.

For the Lorenz model, $N = 3$ and there is chaotic behavior. We therefore conclude that we must have $N \geq 3$ as a necessary condition for the system (2.4.1) to be chaotic. Furthermore a linear system is exactly solvable and it is easy to see that bounded motion must be regular in this case, at least for finite N. In summary, then, *systems of the form* (2.4.1) *can be chaotic only if they are nonlinear and if* $N \geq 3$.

Frequently a discrete mapping can be constructed from the continuous flow in phase space represented by (2.4.1). The Poincaré map (or surface of section) technique is one way to accomplish this, and is most useful in the case $N = 3$. Figure 2.5 illustrates the basic idea in this case. We plot $x_3(t)$ vs. $x_2(t)$ (for instance) only at those times t at which $x_1(t) = 0$ and $\dot{x}_1(t) < 0$. The Poincaré map is thus a two-dimensional mapping of the plane into itself, although of course we cannot expect to be able in general to write down an explicit functional form like (2.3.1). If we could, however, the map would be invertible; this follows simply from the uniqueness theorem for (2.4.1).

The Hénon map was originally studied as an approximation to a Poincaré map obtained numerically for the Lorenz model. Because the Lorenz equations contract volume in phase space, the Poincaré maps will be area-contracting. For a Hamiltonian system, on the other hand, the Poincaré maps may be proven to be area-preserving.

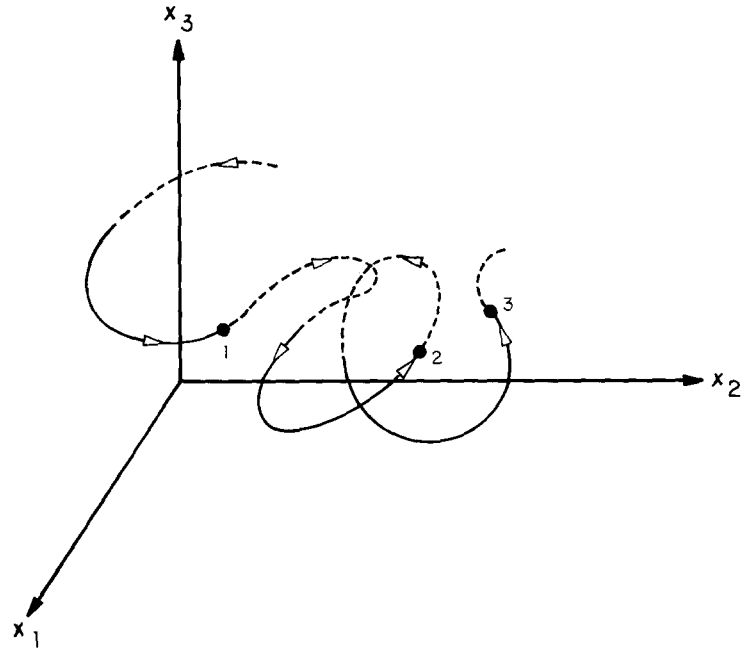

Fig. 2.5. Construction of a Poincaré map with the x_2x_3 plane as the surface of section. In this illustration the Poincaré map takes point 1 into point 2, and point 2 into point 3.

If the system (2.4.1) has regular time evolution, a Poincaré map will consist of a repeating set of points. For chaotic time evolution, on the other hand, successive points will appear to bounce around haphazardly. They may be constrained to a particular attractor, such as in fig. 2.2, but on this attractor they appear to wander erratically.

A simple way to check for periodicity is to compute the (discrete) Fourier transform $\tilde{y}_n(f_k)$ of the time series $y_n(t_l)$ generated by numerical integration of (2.4.1):

$$\tilde{y}_n(f_k) = \sum_{l=0}^{M-1} y_n(t_l) \exp(-2\pi i lk/M), \qquad k = 0, 1, \ldots M-1 \tag{2.4.5}$$

where $t_l = l\,\Delta t$, $f_k = k/M\,\Delta t$, and M is the total number of time points, separated by Δt, sampled from the time series to compute the Fourier transform. Note that the maximum frequency component that can be obtained is determined by the spacing Δt between sampled points of the time series. (Δt need not, of course, be the same as the step size used in the integration.) In practice it is convenient to use the Fast Fourier Transform (FFT) algorithm [21] to evaluate (2.4.5); in this case M is taken to be an integral power of 2, typically 1024, 2048 or 4096. To obtain an accurate FFT, a "cosine bell" function or some other "windowing" function is applied to the sampled time series before the FFT is applied [22]. This eliminates spurious frequency components associated with sharp edges in the time series.

Chaotic systems have a frequency spectrum with a broad-band component, as if there were "noise" present. This is to be expected from our discussion of the logistic mapping, where a positive LCE implies nonperiodicity. We will later see several examples of broad-band spectra for systems of differential equations.

A rigorous test for chaos is to determine whether there is "very sensitive dependence on initial

conditions". Suppose we perturb the initial conditions for (2.4.1) very slightly. The resulting perturbations in the $y_n(t)$ then satisfy the (linearized) equations

$$\delta\dot{y}_n(t) = \sum_{m=1}^{N} \frac{\partial F_n}{\partial y_m} \delta y_m(t) \tag{2.4.6}$$

or in matrix form

$$\delta\dot{y}(t) = J(t)\,\delta y(t)\,. \tag{2.4.7}$$

The solution of this equation is

$$\delta y(t) = \exp\left[\int_0^t \mathrm{d}t_1\, J(t_1)\right] \cdot \delta y(0) \equiv \Lambda(t)\,\delta y(0) \tag{2.4.8}$$

where the $N \times N$ matrix Λ satisfies

$$\dot{\Lambda}(t) = J(t)\,\Lambda(t)\,. \tag{2.4.9}$$

We may define the Lyapunov *type numbers* [23]

$$\lambda_j = \lim_{t\to\infty} \frac{1}{t} \log|\tilde{\lambda}_j(t)| \tag{2.4.10}$$

where the $\tilde{\lambda}_j(t)$ are the eigenvalues of the matrix $\Lambda(t)$. (As mentioned earlier, the limit above need not exist, and we should write lim sup in general.) Note the similarity of (2.4.10) to the LCE (2.3.10) for a discrete mapping.

If one of the λ_j is greater than zero, we have very sensitive dependence on initial conditions. In connection with the Hénon map we noted that the largest LCE may be computed without solving the eigenvalue problem, simply by introducing "random" initial perturbations ε_0, δ_0 and computing (2.3.11) and (2.3.12). Benettin et al. [24] have shown how to compute the largest LCE in the general case; they have also given a procedure for computing the full LCE spectrum [25]. We will only consider the much simpler computation of the largest LCE, which is the main one of interest, of course, in determining whether the system is chaotic or not.

The method of computing the maximal LCE for (2.4.1) is completely analogous to the method based on (2.3.11) and (2.3.12) for the Hénon map. We solve the $2N$ equations (2.4.1) and (2.4.6) simultaneously, assuming "random" values of the initial variations $\delta y_n(0)$. We compute

$$\lambda(t) = \frac{1}{t} \log\|\delta y(t)\| \tag{2.4.11}$$

where $\|\ldots\|$ denotes the Euclidean norm (or any other reasonable norm):

$$\|\delta y\| \equiv \left[\sum_{n=1}^{N} (\delta y_n)^2\right]^{1/2}. \tag{2.4.12}$$

Then $\chi = \lim_{t\to\infty} \lambda(t)$ (or more rigorously $\limsup \lambda(t)$) is the largest LCE of the system. The system is chaotic if and only if $\chi > 0$. We will later see some examples of this numerical procedure.

In connection with the full LCE spectrum, it should be mentioned that there appears to be a relationship between it and the fractal dimension of a chaotic attractor, at least in some cases [13]. In this introductory review, however, it does not seem appropriate to go into this matter. In any case we will only be interested in the largest LCE, which tells us whether the system is chaotic.

2.5. *The Duffing oscillator*

Consider the anharmonic potential (fig. 2.6)

$$V(x) = \tfrac{1}{2}x^2 - \tfrac{1}{4}\beta x^4. \tag{2.5.1}$$

A particle of unit mass in this potential, undergoing a frictional force $-\gamma\dot{x}$ and a sinusoidal driving force $\cos \mu t$, satisfies the equation

$$\ddot{x} + \gamma\dot{x} + x - \beta x^3 = \cos \mu t \tag{2.5.2}$$

which we will call the *Duffing equation.* Chaotic behavior of the Duffing oscillator was first reported by Huberman and Crutchfield [26].

Let us begin by applying to (2.5.2) a well-known approximation of quantum optics, namely the rotating-wave approximation (RWA). We write

$$x(t) = \tfrac{1}{2}[\alpha(t)\, e^{i\mu t} + \alpha^*(t)\, e^{-i\mu t}] \tag{2.5.3}$$

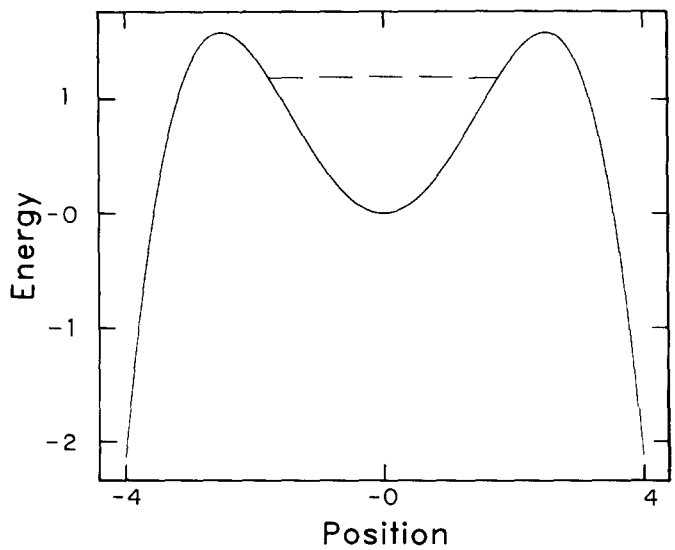

Fig. 2.6. The anharmonic potential (2.5.1) for $\beta = 0.1587$.

and assume that $|\ddot{\alpha}(t)| \ll \mu^2 |\alpha(t)|$. Then the Duffing equation reduces to

$$(\gamma + 2i\mu)\,\dot{\alpha} + (1 - \mu^2 + i\gamma\mu - \tfrac{3}{4}\beta|\alpha|^2)\,\alpha = 1\,. \tag{2.5.4}$$

The steady-state solution of this equation gives the amplitude α_s of the steady-state part of $x(t)$:

$$x_s(t) = \tfrac{1}{2}[\alpha_s\, e^{i\mu t} + \alpha_s^*\, e^{-i\mu t}]\,. \tag{2.5.5}$$

α_s satisfies the equation

$$(1 - \mu^2 + i\gamma\mu - \tfrac{3}{4}\beta|\alpha_s|^2)\,\alpha_s = 1 \tag{2.5.6}$$

which is equivalent to a cubic equation for $|\alpha_s|^2$. As $|\alpha_s|$ is real and positive, there will be either one solution or three solutions to the cubic equation.

Figure 2.7 shows a plot of the solution of (2.5.6) for $|\alpha_s|$, assuming $\beta = 0.1587$ and $\gamma = 0.72$. Also indicated is the "dissociation threshold", i.e., the value of $|\alpha_s|$ at which the potential turns over ($dV/dx = 0$) and the particle is outside the well.

In order to compare the RWA solution (2.5.5) with the exact steady-state dynamics, we note from (2.5.3) that $x^2(t)$ averaged over a driving period is

$$\overline{x^2(t)} = \tfrac{1}{2}|\alpha(t)|^2\,. \tag{2.5.7}$$

We therefore compare $[2\,\overline{x^2(t)}]^{1/2}$, obtained by numerical integration of (2.5.2), with the RWA steady-state amplitude $|\alpha_s|$. The circles in fig. 2.7 are computed values of $[2\,\overline{x^2(t)}]^{1/2}$, and show that the RWA is a good approximation when it predicts an oscillation amplitude below the dissociation threshold.

However, the steady-state RWA solution (2.5.5) predicts a regular oscillation at the driving frequency, whereas the exact solution $x(t)$ has harmonics (and in some cases subharmonics) of the driving frequency. Figure 2.8a shows $x(t)$ obtained by solving (2.5.2) numerically for $\beta = 0.1587$,

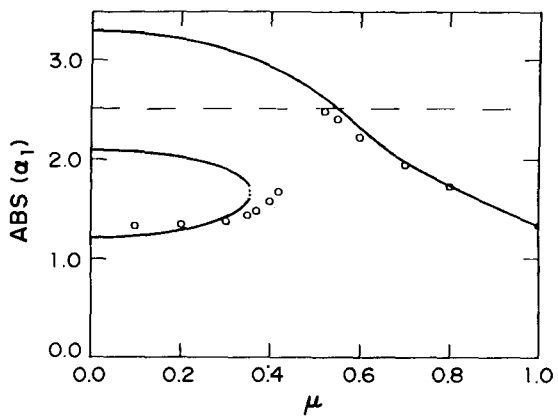

Fig. 2.7. The solution of (2.5.6) for $|\alpha_s|$ with $\beta = 0.1587$ and $\gamma = 0.72$. The dotted line indicates the "dissociation threshold" for escaping from the potential well. The circles are obtained from the integration of the Duffing equation. (See text.)

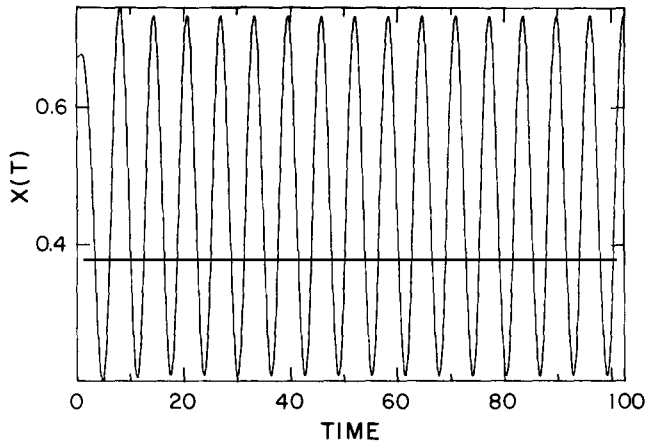

Fig. 2.8a. $x(t)$ obtained by integrating the Duffing equation for $\beta = 0.1587$, $\gamma = 0.728$, $\mu = 1.0$.

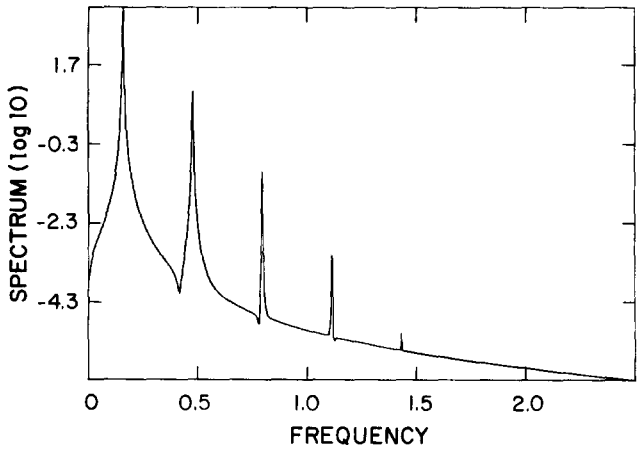

Fig. 2.8b. The power spectrum of the function shown in fig. 2.8a.

$\gamma = 0.728$ and $\mu = 1.0$, and fig. 2.8b shows the power spectrum of this time series obtained with an FFT algorithm. The spectrum clearly indicates the presence of third, fifth, seventh and ninth harmonics of the driving frequency ($\mu/2\pi \cong 0.16$). Note that the power spectrum is plotted on a log scale, indicating that the harmonic components are very weak compared with the fundamental. Of course this is consistent with the high accuracy of the RWA solution.

Figure 2.9a shows $x(t)$ when μ is reduced to 0.53, and fig. 2.9b its power spectrum. Now we notice in the spectrum not only a zero-frequency component, but also a $\mu/2$ subharmonic and its harmonics; the subharmonic and harmonic components are again weak compared with the fundamental. In fig. 2.10a we have reduced μ to 0.515, and a strong period-2 subharmonic (frequency $\mu/2$) is evident both in $x(t)$ and its power spectrum shown in fig. 2.10b. Figure 2.11, for $\mu = 0.5143$, shows a period-4 component (frequency $\mu/4$). What we are seeing is a period-doubling sequence as the "knob" μ is reduced.

Indeed a period-doubling route to *chaos* is found: If μ_n denotes the value of μ at which the nth

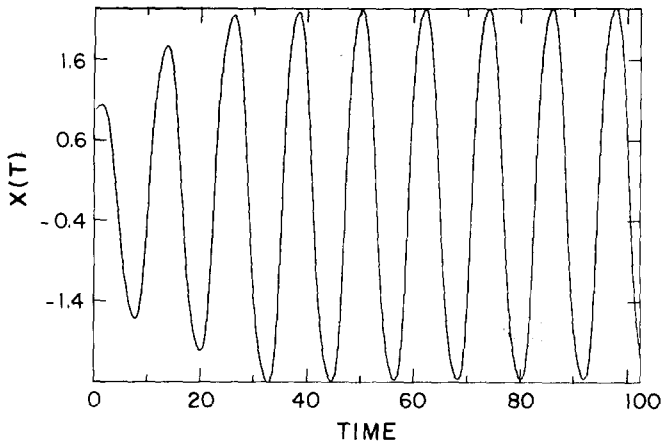

Fig. 2.9a. $x(t)$ obtained by integrating the Duffing equation for $\beta = 0.1587$, $\gamma = 0.728$, $\mu = 0.53$.

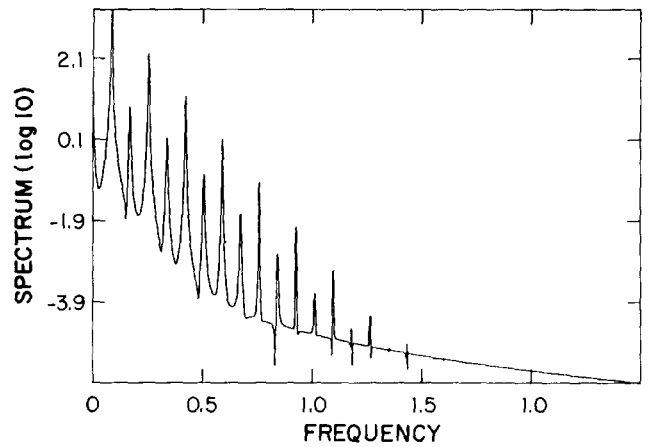

Fig. 2.9b. The power spectrum of the function shown in fig. 2.9a.

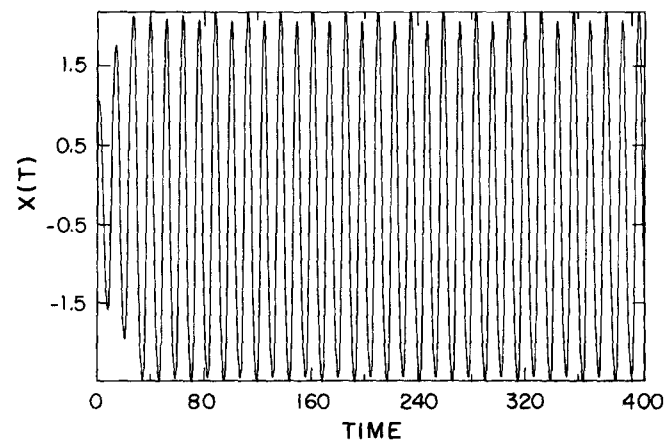

Fig. 2.10a. $x(t)$ obtained by integrating the Duffing equation for $\beta = 0.1587$, $\gamma = 0.728$, $\mu = 0.515$.

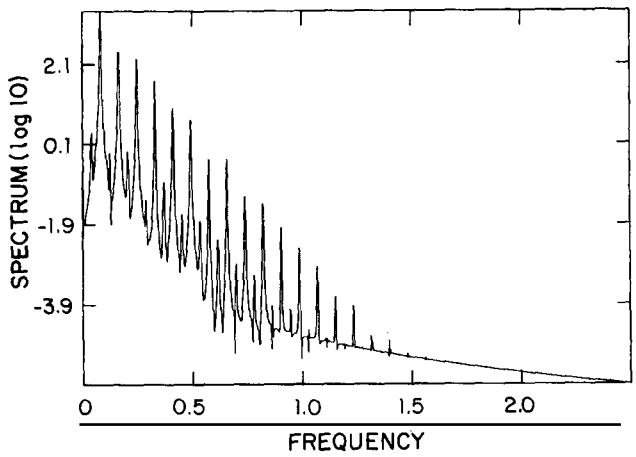

Fig. 2.10b. The power spectrum of the function shown in fig. 2.10a.

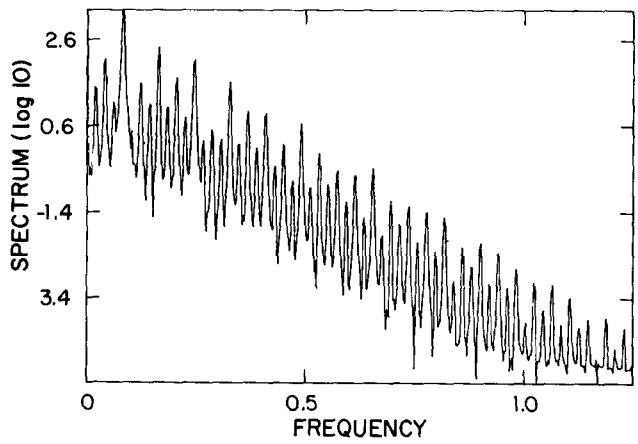

Fig. 2.11. The power spectrum of the solution $x(t)$ of the Duffing equation for $\beta = 0.1587$, $\gamma = 0.728$, $\mu = 0.5143$.

bifurcation occurs, and $\lambda_n = \mu_n^{-1}$, it is found that

$$(\lambda_n - \lambda_{n-1})/(\lambda_{n+1} - \lambda_n) \to \delta$$

as n increases, δ being the Feigenbaum number (2.2.9). For these values of β and γ, a value $\mu = 0.51$, for instance, puts us past the threshold for chaos where the period has doubled *ad infinitum*. Figures 2.12a and 2.12b show $x(t)$ and its power spectrum. Note the broad-band character of the power spectrum, indicating nonperiodic motion. The form of this spectrum is typical of chaotic time evolution.

Sensitive dependence on initial conditions is verified by computing Lyapunov exponents. A "quick and dirty" way of verifying sensitive dependence on initial conditions, however, is to consider some measure of distance between two trajectories originating from two different but nearby initial conditions. In fig. 2.13 we show $x(t)$ computed as in fig. 2.12a for $\mu = 0.51$, but with slightly different initial conditions. Figure 2.14 is a plot of the "distance"

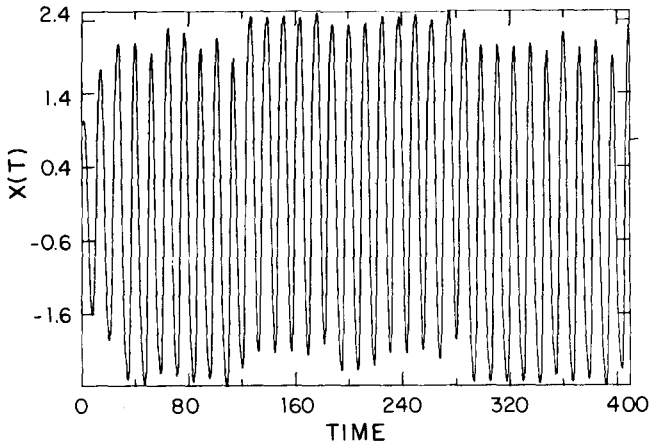

Fig. 2.12a. $x(t)$ obtained by integrating the Duffing equation for $\beta = 0.1587$, $\gamma = 0.728$, $\mu = 0.51$.

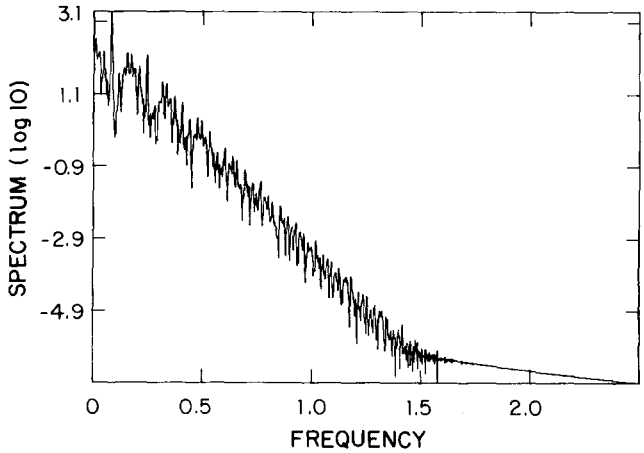

Fig. 2.12b. The power spectrum of the function shown in fig. 2.12a, showing the broad-band structure typical of chaotic time evolution.

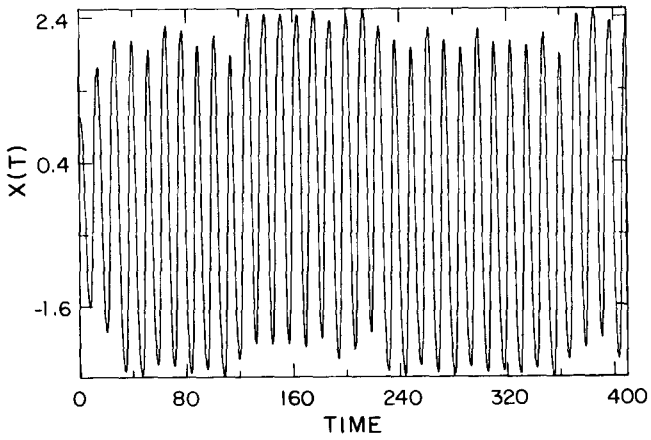

Fig. 2.13. $x(t)$ as in fig. 2.12a but with slightly different initial conditions (differing by less than a tenth of a percent).

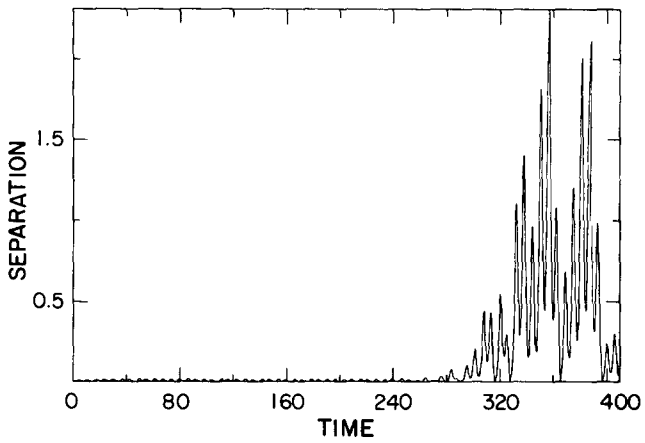

Fig. 2.14. The distance (2.5.8) between the functions $x(t)$ shown in figs. 2.12a and 2.13, illustrating very sensitive dependence on initial conditions.

$$\delta(t) = [(x(t) - x'(t))^2]^{1/2} \tag{2.5.8}$$

where $x(t)$ and $x'(t)$ are given in figs. 2.12a and 2.13, respectively. Figure 2.14 is a nice illustration of what is meant by "very sensitive dependence on initial conditions". Such a degree of sensitivity on initial conditions is never exhibited for regular (bounded) motion.

In connection with the RWA, we have noted that the RWA can be a good approximation even though it fails to account for the chaotic behavior of the Duffing oscillator. This is illustrated particularly well by considering the parameter regime investigated by Huberman and Crutchfield [26]: For the form (2.5.2) of the Duffing equation, take $\gamma = 0.4$ and $\beta = 0.055$. (It may be worth noting that Huberman and Crutchfield's results were obtained with an analog computer, and are subject to small errors. For instance, we find that the onset of chaos occurs at a value of μ different from that in their paper.) Figure 2.15 compares the exact solution of the Duffing equation in this case with the RWA solution, exactly as in fig. 2.7. We see from this figure that for this choice of parameters the RWA is surprisingly accurate.

For the case shown in fig. 2.15 the Duffing oscillator has a range of driving frequencies μ for which three solutions of (2.5.6) exist. However, the middle branch is unstable, as indicated by the pattern of

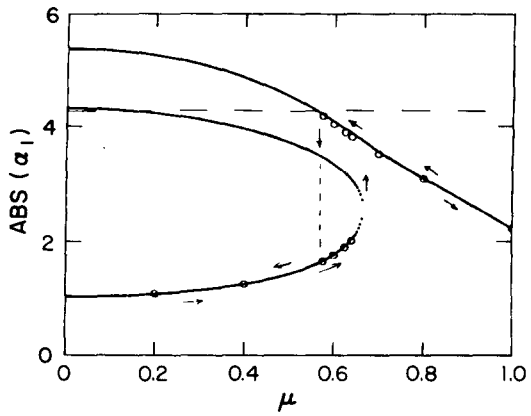

Fig. 2.15. Comparison of exact (O) and RWA solutions (—) of the Duffing equation for $\beta = 0.055$ and $\gamma = 0.4$, as in fig. 2.7.

circles in fig. 2.15. In other words, we have a *bistable* (rather than tristable) regime. Which branch the solution takes depends upon the initial conditions, as implied by the arrows; that is, we have *hysteresis* behavior. It is interesting to note that *the RWA equation* (2.5.4) *also exhibits bistability and hysteresis, but not chaos.* For these parameters, therefore, the RWA is quite accurate, except that it does not predict chaos. This is consistent with fig. 2 of the Huberman–Crutchfield paper, which indicates that the broad-band portion of the power spectrum of $x(t)$ is quite weak. The numerical solution of the Duffing equation in this case has relatively small deviations from periodicity. In this case "very sensitive dependence on initial conditions" is manifested mainly by an eventual dephasing of the oscillations corresponding to two slightly different initial conditions.

The Duffing equation has no known closed-form solution. What we have called the RWA is a well-known approximation in the theory of nonlinear oscillations [27]; it is sometimes called Duffing's approximation. If instead of the RWA we use standard perturbation theory, assuming the nonlinearity to be small, we find only the odd harmonics of the driving frequency in (2.5.2). Some progress has been made in understanding the period doubling, which is always observed to be preceded by the appearance of even harmonics [14, 28–30]. Novak and Frehlich [28], for instance, have interpreted the even harmonics and the period-doubling sequence, in the case of increasing driving amplitude, in terms of parametric resonance.

We have also observed some stable n-cycles in the chaotic regime, and in the order specified by Šarkovskii's theorem. In particular, we have found a 3-cycle ("Period Three Implies Chaos" [9]) followed by a period-doubling sequence (i.e., 3–6–12–24–...) [14, 30].

2.6. The Lorenz model

In 1963 Lorenz [17] published a paper entitled "Deterministic Nonperiodic Flow", in which he discussed the remarkable properties of the system

$$\dot{x} = -\sigma(x - y), \qquad \sigma > 0 \tag{2.6.1a}$$

$$\dot{y} = -y - xz + rx, \qquad r > 0 \tag{2.6.1b}$$

$$\dot{z} = xy - bz, \qquad b > 0. \tag{2.6.1c}$$

Using the present terminology we can say that this system, called the *Lorenz model*, has a chaotic regime, i.e., for certain parameters σ, r and b it has nonperiodic time evolution with very sensitive dependence on initial conditions. Lorenz obtained (2.6.1) as a rather drastic truncation of a set of partial differential equations for fluid flow. The Lorenz model has become a standard example of chaos in a low-dimensional flow in phase space (i.e., chaos in a system of the form (2.4.1) with N a small integer).

As in the case of the Duffing oscillator, the Lorenz model has no known analytical solution, so let us begin by simply making some general observations, and then integrating the equations numerically. First we note that the system (2.6.1) is invariant under the transformation $(x, y, z) \to (-x, -y, z)$. Furthermore the z-axis is invariant in the sense that any trajectory starting at (or passing through) a point $(0, 0, z)$ on the z-axis remains on the z-axis, and moreover all such trajectories approach the origin, $(0, 0, 0)$.

An obvious fixed point of the Lorenz system is $(0, 0, 0)$. If $r > 1$ it is found that there are two additional fixed points in the three-dimensional phase space:

$$x^* = y^* = \pm[b(r-1)]^{1/2}, \qquad z^* = r-1. \tag{2.6.2}$$

The stability of these fixed points may be investigated in the familiar way by linearizing (2.6.1) about a fixed point, and finding the eigenvalues of the resulting 3×3 matrix. For the linearized flow near the origin, these eigenvalues are

$$\lambda = -b, \qquad -\tfrac{1}{2}(\sigma+1) \pm \tfrac{1}{2}[(\sigma-1)^2 + 4\sigma r]^{1/2}. \tag{2.6.3}$$

One of these eigenvalues is positive whenever $r>1$, and so the origin is an unstable fixed point for $r>1$.

(Actually the origin is "nonstable" for $r>1$. The definition of stability – that starting near the set in question we remain near to it – refers to *any* point near the set. But we have seen, for instance, that the z-axis is invariant and that the origin attracts any trajectory starting on the z-axis. Since the origin is unstable for "most" points surrounding it, we will call it "unstable", as is frequently done whenever *one* of the eigenvalues of the linearized flow has a positive real part.)

The other two fixed points are found to be unstable (more precisely, nonstable) when

$$\sigma > b+1 \tag{2.6.4a}$$

and

$$r > \sigma(\sigma+b+3)/(\sigma-b-1). \tag{2.6.4b}$$

For $\sigma = 3$ and $b = 1$, (2.6.4) is satisfied whenever $r>21$. One of the eigenvalues around the linearized flow is real and negative for all r. For $r>21$ the other two eigenvalues have positive real parts. The transition at $r = 21$, where the complex eigenvalues cross the imaginary axis and take on positive real parts, is an example of a *Hopf bifurcation* [31, 32].

Suppose we integrate the Lorenz equations numerically for $\sigma = 3$, $b = 1$, $x(0) = y(0) = z(0) = 1.0$, letting r be our "knob". Figure 2.16 shows the resulting $y(t)$ for $r = \frac{1}{2}$; $y(t)$ approaches $y^* = 0$ in this case, because $(0,0,0)$ is the only stable fixed point. For $r = 4$, $(0,0,0)$ is unstable, but the fixed point

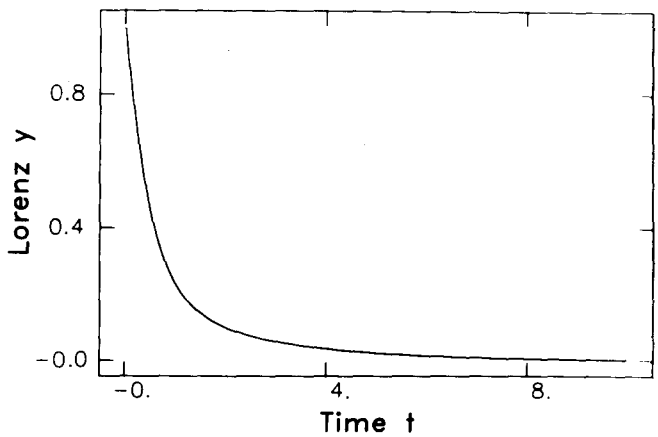

Fig. 2.16. $y(t)$ of the Lorenz model for $\sigma = 3$, $b = 1$, $r = 1/2$, $x(0) = y(0) = z(0) = 1.0$.

$(\sqrt{3}, \sqrt{3}, 3)$ predicted by (2.6.2) is stable, and the solution converges onto this simple attractor, as shown in fig. 2.17. At $r = 21$ for these initial conditions, $y(t)$ begins as an orderly but growing oscillation, then apparently breaks into chaos (fig. 2.18). Similar behavior is observed in fig. 2.19 for $r = 22$.

Consider the divergence of the flow velocity in phase space:

$$\nabla \cdot \boldsymbol{v} = \partial\dot{x}/\partial x + \partial\dot{y}/\partial y + \partial\dot{z}/\partial z = -(\sigma + b + 1)\,. \tag{2.6.5}$$

Thus

$$\int_{V\in S} \mathrm{d}^3x\, \nabla \cdot \boldsymbol{v} = \oint_S \mathrm{d}a\, \boldsymbol{v} \cdot \hat{\boldsymbol{n}} = \frac{\mathrm{d}V}{\mathrm{d}t} = -\int_V \mathrm{d}^3x\, (\sigma + b + 1) = -(\sigma + b + 1)V$$

or

$$V(t) = V(0)\, \mathrm{e}^{-(\sigma+b+1)t}\,. \tag{2.6.6}$$

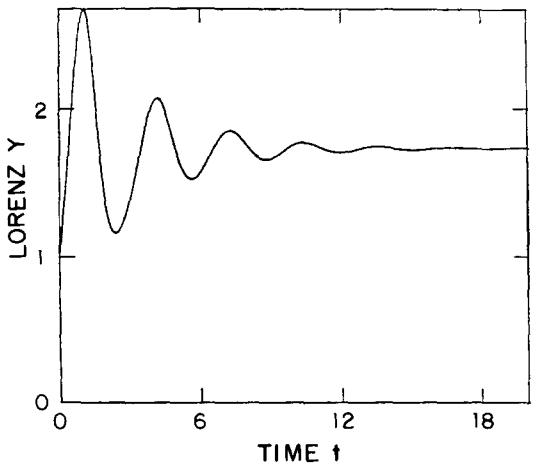

Fig. 2.17. As in fig. 2.16, but with $r = 4$.

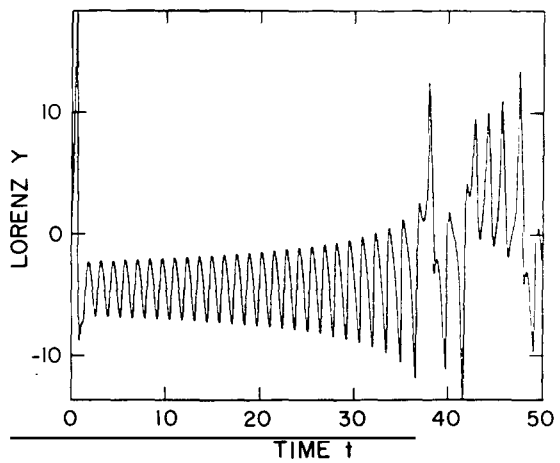

Fig. 2.18. As in fig. 2.16, but with $r = 21$.

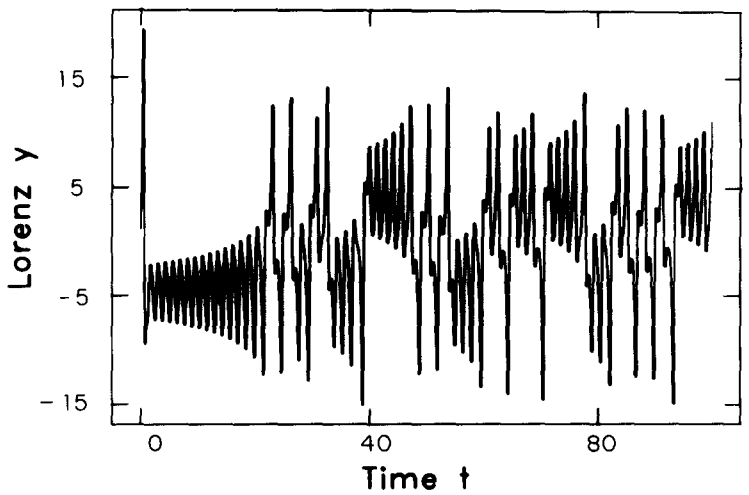

Fig. 2.19. As in fig. 2.16, but with $r = 22$.

That is, if we let each point on some closed surface in phase space evolve in time according to (2.6.1), the enclosed volume contracts exponentially to zero. Lorenz [17] proved the existence of a bounded ellipsoid in phase space that attracts all trajectories. Equation (2.6.6) in turn implies that all trajectories eventually settle onto a zero-volume set within this ellipsoid. In other words, any attractor of (2.6.1) must occupy zero-volume in phase space. This is interesting when $r > 21$, in which case the fixed points of the flow are all unstable. It is precisely in this case that the Lorenz system can be chaotic, and that its attractor can have the property of hyperbolicity (strange attractor). The situation here is much like in the case of the area-contracting Hénon map.

Figure 2.20 shows the power spectrum of $y(t)$ for the case $r = 22$ (fig. 2.19), taken after initial transients have decayed away. We see the characteristic broad-band spectrum of chaos. In fig. 2.21 we illustrate very sensitive dependence on initial conditions by plotting for $r = 22$

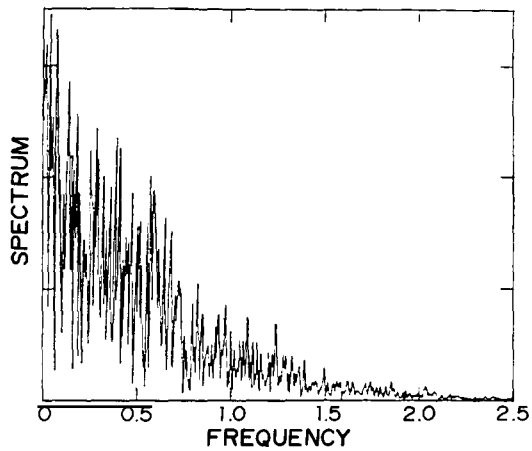

Fig. 2.20. Power spectrum of $y(t)$ shown in fig. 2.19.

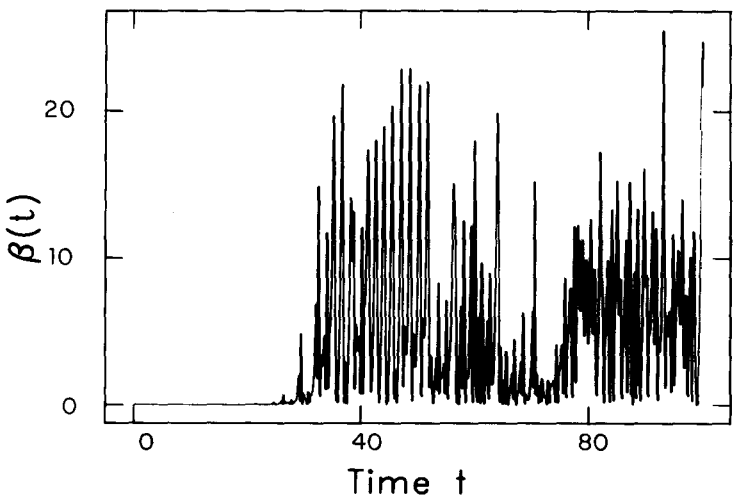

Fig. 2.21. The distance (2.6.7), illustrating very sensitive dependence on initial conditions.

$$d = [(y(t) - y'(t))^2]^{1/2} \tag{2.6.7}$$

where $y(t)$ and $y'(t)$ are obtained from initial conditions (1.0, 1.0, 1.0) and (1.001, 1.001, 1.001). A similar result is found when the difference in initial conditions is very much smaller. *When a system is chaotic, the slightest difference in initial conditions will lead (on average) to exponential separation of initially close trajectories.*

Figure 2.22 shows $z(t)$ corresponding to fig. 2.19. Following Lorenz, we plot in fig. 2.23 the nth maximum of z vz. the $(n-1)$st maximum for $t \gtrsim 20$, i.e., after we have settled onto the chaotic attractor. This map looks something like the parabola of the logistic map, although the maximum is

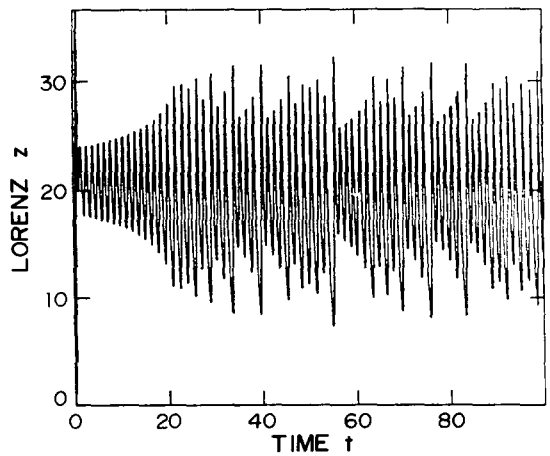

Fig. 2.22. $z(t)$ of the Lorenz model for the parameters of fig. 2.19.

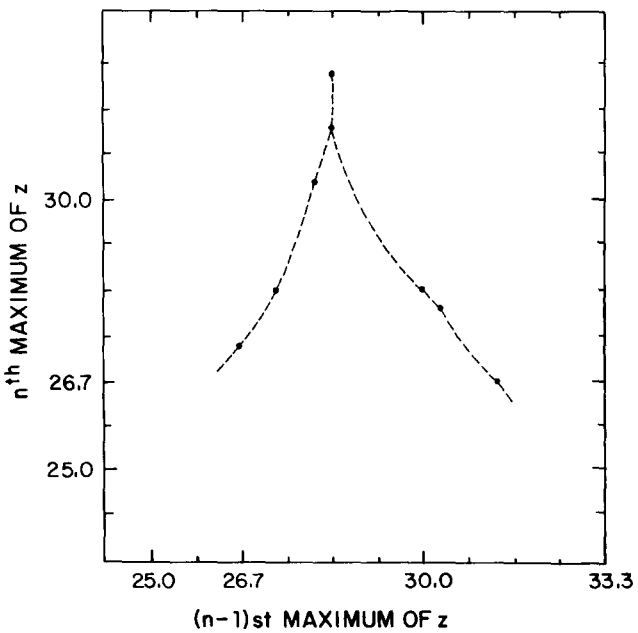

Fig. 2.23. The nth maximum of $z(t)$ (fig. 2.22) vs. the $(n-1)$st maximum, for $t \gtrsim 20$.

much sharper than quadratic. Evidently this mapping has no stable n-cycle, but instead generates a chaotic sequence having the property of very sensitive dependence on initial conditions.

There is a vast literature on the Lorenz model, and we cannot possibly in the space allotted do more than touch upon some of its interesting features. Sparrow's monograph [18] is recommended to the reader wishing to undertake a detailed study of this system. We will end our casual introduction by summarizing some of the behavior of the Lorenz model as r is varied. We will focus on the parameter values studied by Lorenz: $\sigma = 10$ and $b = \frac{8}{3}$. For these values, (2.6.4a) is satisfied and (2.6.4b) becomes $r > 470/19 \cong 24.71 \cong r_c$. Lorenz considered in detail the case $r = 28$.

For $r < 1$ all trajectories approach the origin. Two of the eigenvalues (2.6.3) of the linearized flow about the origin are always negative, indicating that there is a two-dimensional *stable manifold* of the origin – the set of points where a starting trajectory approaches the origin as $t \to \infty$; the one-dimensional *unstable manifold* of the origin existing for $r > 1$, on the other hand, consists of points approaching the origin as $t \to -\infty$. This is indicated in fig. 2.24a. At $r = 1$ the new fixed points (2.6.2) are born, and a trajectory starting on the unstable manifold of the origin for $r > 1$ heads for that fixed point lying in the same half space. As indicated in fig. 2.24b, the trajectory spirals toward the fixed point (a stable spiral point). This is consistent with the oscillatory approach to fixed points found numerically in fig. 2.17, and is simply a consequence of having a complex eigenvalue associated with the linearized flow. As r is increased the spiral loops get larger.

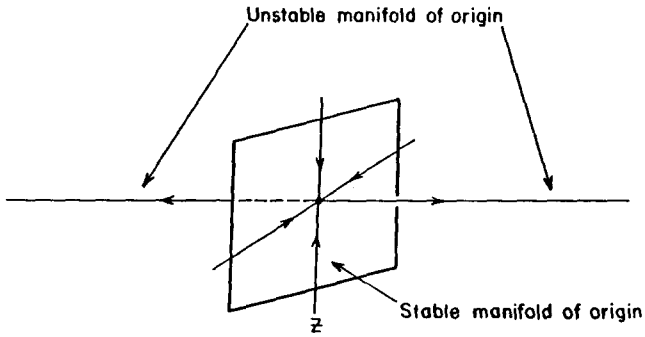

Fig. 2.24a Stable and unstable manifolds of the origin in the Lorenz model.

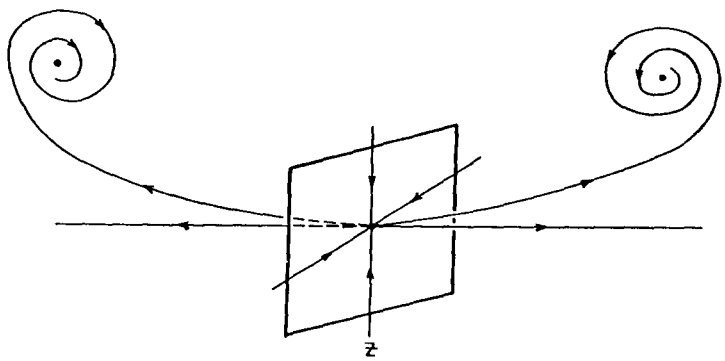

Fig. 2.24b. For $1 < r < r'$ a trajectory starting on the unstable manifold of the origin approaches the stable fixed point in the same half space.

An interesting thing happens when r is raised beyond $13.926... \equiv r'$. In this case the spirals have become large enough that they become attracted to the fixed point in the other half space, as indicated schematically in fig. 2.25. In fig. 2.26a we show a plot of $y(t)$ vs. $x(t)$ obtained by numerically integrating the Lorenz system with $\sigma = 10$, $b = \frac{8}{3}$ and $r = 13.84 < r'$, assuming an initial condition on the unstable manifold of the origin. In fig. 2.26b we show the corresponding result for $r = 13.96 > r'$, indicating how the trajectory crosses over to the fixed point in the other half space. What happens at $r = r'$ is that a trajectory starting out on the unstable manifold of the origin is eventually attracted to the origin, or in other words the unstable manifold of the fixed point at the origin lies within its stable manifold. In this case it is said that we have a *homoclinic orbit* – a trajectory tending to a fixed point x^* for both $t \to \infty$ and $t \to -\infty$. This is illustrated in fig. 2.27.

Beyond $r = r'$ the two branches of the unstable manifold of the origin are attracted to the fixed point in the opposite half space, as in fig. 2.25. By numerically constructing the Poincaré map with surface of section $z = r - 1$, Kaplan and Yorke [33] have shown that there exists an infinite number of both chaotic and periodic orbits. All of these are unstable, however, as most trajectories are attracted to one of the

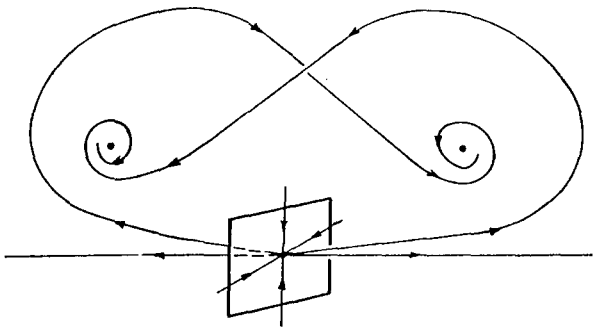

Fig. 2.25. For $r' < r < r_c$ a trajectory starting on the unstable manifold of the origin approaches the stable fixed point in the opposite half space.

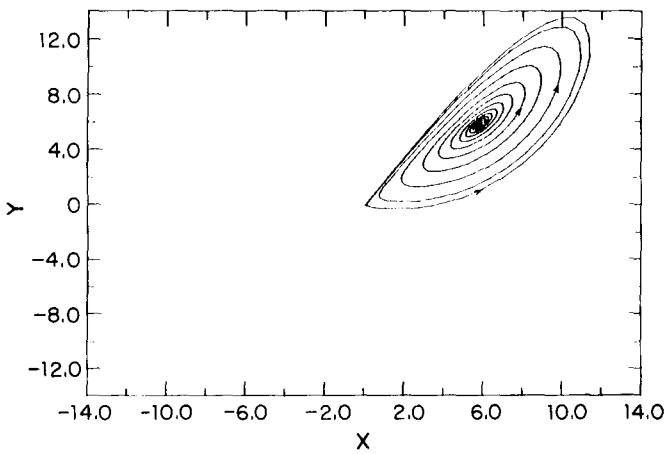

Fig. 2.26a. $y(t)$ vs. $x(t)$ for $r = 13.84$, illustrating the behavior shown in fig. 2.24b.

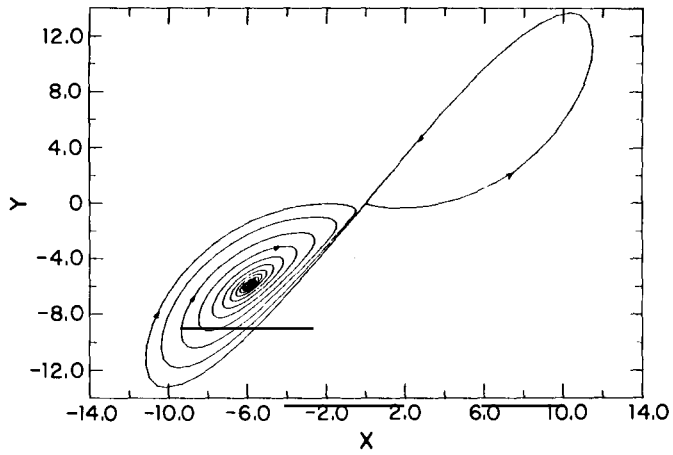

Fig. 2.26b. $y(t)$ vs. $x(t)$ for $r = 13.96$, illustrating the behavior shown in fig. 2.25.

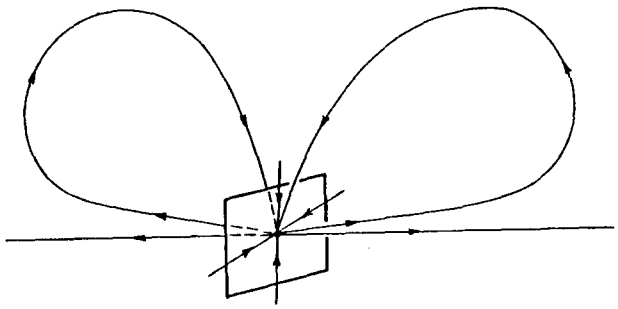

Fig. 2.27. Homoclinic orbits at $r = r'$.

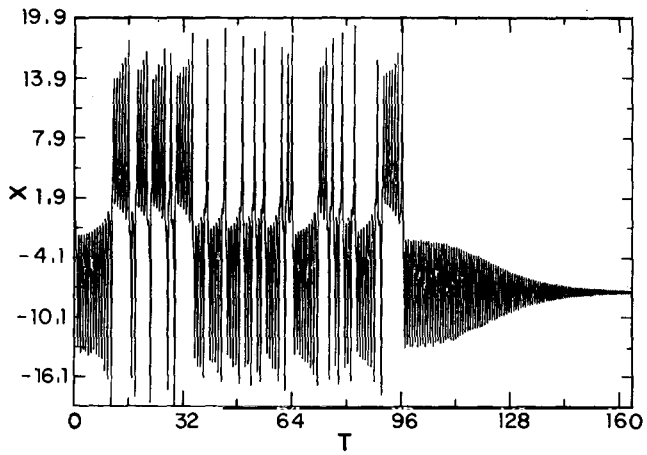

Fig. 2.28. An example of "preturbulent" behavior for $r = 22.2$.

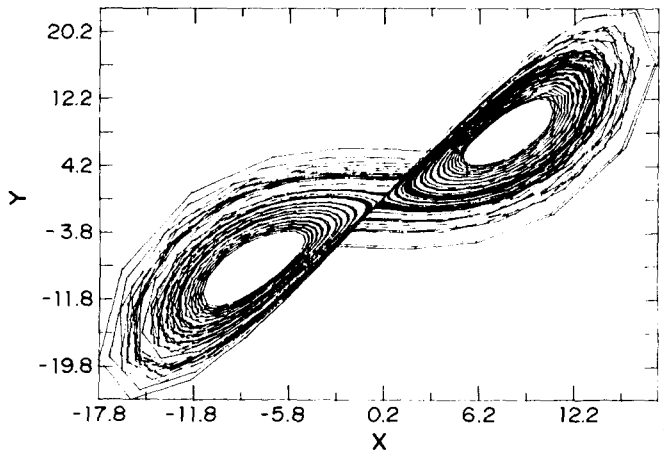

Fig. 2.29. $y(t)$ vs. $x(t)$ for $r = 26$.

two stable fixed points for $r < r_c$. Thus we have the possibility of "preturbulence" [34] or "metastable chaos". An example is shown in fig. 2.28 for $r = 22.2$.

At $r = r'$, the homoclinic orbit gave way to an unstable limit cycle. At $r \cong 24.06 \equiv r''$ the unstable manifold of the origin now spirals onto the unstable limit cycle rather than the stable fixed point. Between $r = r''$ and $r = r_c$ trajectories settle on a chaotic attractor or one of the stable fixed points, depending on initial conditions. At $r = r_c$ the unstable limit cycles collapse onto the fixed points (a so-called subcritical Hopf bifurcation), and beyond $r = r_c$ all three fixed points are unstable. Only the stable chaotic attractor (the "standard" Lorenz attractor) remains. Results like those shown in figs. 2.18–2.22 are typical of this chaotic regime. Figure 2.29 shows $x(t)$ vs. $y(t)$ for $r = 26$. As this picture evolves the trajectory appears to switch from the neighborhood of one of the (unstable) fixed points to the other in an apparently random fashion.

For very large r nearly all trajectories are attracted to a stable limit cycle [35]. Figure 2.30 shows $x(t)$ vs. $y(t)$ for $r = 230$, 220 and 216; we are seeing there the early stages of a period-doubling route to chaos as r is *decreased* from these large values. As in the logistic map, periodic windows occur within the chaotic regime where stable limit cycles are found.

As the reader has by now surmised, the Lorenz model has been studied in great detail. It exemplifies the remarkably rich variety of behavior to be found even in "simple-looking" nonlinear systems. To our knowledge, however, the Lorenz model as yet has no experimental realization. We will later discuss an example in quantum optics where model equations have exactly the same form as the Lorenz system.

In closing our introduction to the Lorenz model, we mention that Shimada and Nagashima [36] have computed the three Lyapunov exponents of the Lorenz system for $\sigma = 16$, $b = 4$, $r = 40$. They obtain a maximal LCE $\cong 1.37$. Conjectured formulas relating the dimension of an attractor to the LCE [37, 38] give a fractal dimension $d \cong 2.06$ for the Lorenz attractor in this case.

2.7. Routes to chaos

As we have mentioned, part of the interest in chaotic dynamics lies in the fact that certain routes to chaos seem to be characteristic of a large number of chaotic systems. We have seen the periodic-

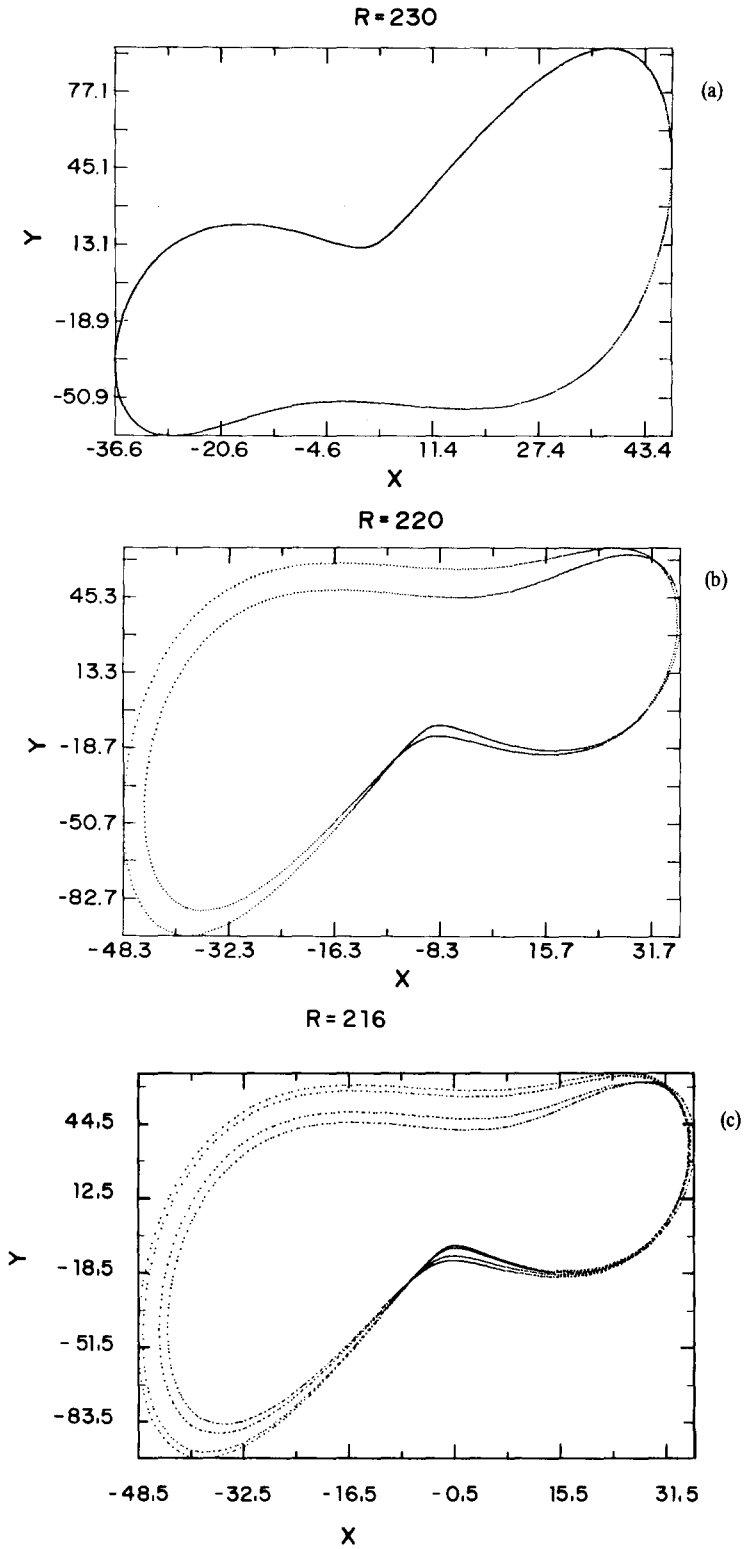

Fig. 2.30. A period-doubling sequence in the Lorenz model. (a) $r = 230$, (b) $r = 220$, (c) $r = 216$.

doubling route to chaos, for instance, in the logistic and Hénon maps, the Duffing oscillator, and in the Lorenz model for large r. There are many routes to chaos, but the period-doubling route, and two others, have been rather well defined both theoretically and in experimental (actual or numerical) studies. Eckmann [39] has reviewed these particular "roads to turbulence" in dissipative systems. Here we will briefly describe the different "scenarios". We will see later that *all* these scenarios have now been experimentally realized in experiments with lasers.

First we mention one of the oldest formulated routes to turbulence, that of Landau [40]. In this scenario a fluid becomes turbulent by an unlimited sequence of instabilities: As the Reynolds number increases, the flow becomes doubly, then triply, then quadruply,... periodic. That is, the number of incommensurate frequencies in the spectrum keeps growing, and the flow pattern becomes very complicated or "turbulent". However, we now recognize that this is not really chaotic motion, because the spectrum is always discrete, becoming effectively broad-band only in the limit of an infinite number of incommensurate frequencies.

Furthermore the Landau scenario appears even to be "unlikely". Ruelle and Takens [41] suggested that nonlinearities make the transition from a doubly periodic state to a triply periodic one unlikely, and that, after the doubly periodic state, a *strange attractor* is more likely. (This was the first paper to refer to a "strange" attractor.) *Implicit in their paper is the assumption that chaos (turbulence) in a real fluid may be associated with the appearance of a low-dimensional strange attractor in the phase space of a fully deterministic system.*

In the Ruelle–Takens route to chaos, a steady state (stable fixed point) gives way to an oscillatory state (limit cycle) by means of a Hopf bifurcation as a "knob" is turned. Then another bifurcation occurs and the motion becomes doubly periodic, corresponding to a toroidal surface in phase space (two incommensurate frequencies in the spectrum). Finally a third bifurcation occurs in which the doubly periodic, toroidal motion gives way to a chaotic attractor.

Curry and Yorke [42] have described a two-dimensional map in which doubly-periodic motion is followed by a chaotic (strange) attractor. In the case of a continuous flow, Curry [43] has studied a system of ordinary differential equations with $N = 14$, and infers from a Poincaré map that chaos is preceded by a two-dimensional torus in the 14-dimensional phase space. It is interesting to note that Curry's system arose from an extension of the Lorenz model to include more terms in a modal expansion.

In addition to the period-doubling and Ruelle–Takens scenarios is the Pomeau–Manneville or "intermittency" route to chaos [44]. This is associated with a "collision" of a stable fixed point with an unstable fixed point, as Eckmann [39] has illustrated with an example of a one-dimensional map. Unlike the period-doubling or Ruelle–Takens scenarios, this scenario does not tell us "when" the transition occurs. It describes a situation in which the motion alternates between periodic behavior and (intermittent) "bursts" of chaos. Very loosely, we can imagine a limit cycle that becomes unstable when a parameter is swept through some critical value, giving rise to "chaotic" motion. In its chaotic meandering a trajectory enters the basin of attraction of the limit cycle, and therefore gets "trapped" again – temporarily – into periodicity.

We will see experimental evidence of these three scenarios in the following sections. For a much less "hand-waving" discussion the reader is referred to Eckmann's review [39], where references to experimental studies of routes to chaos in fluid flows may be found. Experimental reports of chaos by various routes now abound. We mention, for instance, experiments on semiconductor nonlinear oscillators, which accurately confirm predictions of the theory [45–47].

3. Chaos in a many-atom Jaynes–Cummings model

3.1. Introduction

Any doubts about the relevance of chaotic dynamics to quantum optics may be dispelled by considering one of the simplest models in the field: The interaction of a collection of two-level atoms with a single mode of the electromagnetic field. This model has chaotic time evolution, as first discussed by Belobrov et al. [48]. Similar conclusions were later reported independently in ref. [49], the notation of which we will follow here. In particular, it was found that the rotating-wave approximation (RWA) fails completely to account for chaotic behavior, just as in the case of the Duffing oscillator discussed in the preceding section. This failure of the RWA may be one reason why this example of chaos was not discovered much earlier. According to Belobrov et al., "The neglect of the [non-RWA] terms is so weakly based because of the formal difficulties which occur, that the generally accepted use of the [RWA] Hamiltonian of the system has changed into a sort of symbol of faith" [48].

Our treatment will be semiclassical, i.e., the field is treated classically whereas the two-level atoms, of course, are quantum mechanical and are described by the time-dependent Schrödinger equation. All the atoms will be assumed to lie within a region small compared with the wavelength of the (single-mode) field. The model is basically an extension of the Jaynes–Cummings and Tavis–Cummings models [50, 51]. The former considers a single two-level atom (TLA) interacting with a single field mode, whereas the latter extends the treatment to $N>1$ TLAs. Our treatment differs in that (1) the semiclassical approximation is made but (2) the RWA is not made.

3.2. Equations of motion

For a single TLA the state vector at any time t may be written as a superposition of the upper- and lower-energy eigenstates, $|2\rangle$ and $|1\rangle$, respectively:

$$|\psi(t)\rangle = c_1(t)\,|1\rangle + c_2(t)\,|2\rangle\,. \tag{3.2.1}$$

From the Schrödinger equation, with

$$x(t) = c_1^*(t)\,c_2(t) + c_1(t)\,c_2^*(t) \tag{3.2.2a}$$

$$y(t) = \mathrm{i}[c_1^*(t)\,c_2(t) - c_1(t)\,c_2^*(t)] \tag{3.2.2b}$$

$$z(t) = |c_2(t)|^2 - |c_1(t)|^2 \tag{3.2.2c}$$

it follows that [52]

$$\dot{x} = -\omega_0 y \tag{3.2.3a}$$

$$\dot{y} = \omega_0 x + \frac{2d}{\hbar} Ez \tag{3.2.3b}$$

$$\dot{z} = -\frac{2d}{\hbar} Ey \tag{3.2.3c}$$

where $\hbar\omega_0 = E_2 - E_1$ and d is the transition electric dipole moment in the direction of the (linearly polarized) field. Equations (3.2.3) are the well-known optical Bloch equations, assuming an interaction $-\boldsymbol{d}\cdot\boldsymbol{E}$ between the atom and the field. They have the first integral $x^2 + y^2 + z^2 = 1$, which means that any trajectory of (3.2.3) lies on the "Bloch sphere" of phase space.

Equations (3.2.3), with E a prescribed external field, do not admit chaotic behavior because of the restriction to motion on the Bloch sphere. Suppose, however, that $E(t)$ is the field generated by N TLAs per unit volume. For $E(t)$ we then write the Maxwell equation

$$\ddot{E}(t) + \omega^2 E(t) = -4\pi N d\,\ddot{x}(t) \tag{3.2.4}$$

for a single-mode field of angular frequency ω. The system (3.2.3) plus (3.2.4) couples the Schrödinger and Maxwell equations self-consistently. That is, E determines the motion on the Bloch sphere via (3.2.3), while the TLAs in turn act as a source for E via (3.2.4). Let $\tau = \omega_0 t$ and $e(t) = (2d/\hbar\omega_0)\,E(t)$. Then our dynamical system (3.2.3) plus (3.2.4) is

$$\dot{x} = -y \tag{3.2.5a}$$

$$\dot{y} = x + ez \tag{3.2.5b}$$

$$\dot{z} = -ey \tag{3.2.5c}$$

$$\ddot{e} + \mu^2 e = \beta\dot{y} \tag{3.2.5d}$$

which may be written trivially in the form (2.4.1). We have defined the dimensionless parameters $\mu = \omega/\omega_0$ and

$$\beta = 8\pi N d^2/\hbar\omega_0 \tag{3.2.6}$$

and the derivatives in (3.2.5) are with respect to τ.

The divergence of the flow in phase space of the system (3.2.5) is zero, so that our dynamical system is not dissipative. As such it has no attracting sets (attractors). This is because our semiclassical approach does not account for spontaneous emission, and indeed there are no damping terms, phenomenological or otherwise, in (3.2.5). Although the system therefore will not have a strange attractor, it can nevertheless be chaotic, as we will see.

3.3. Chaotic behavior

We will restrict ourselves to the case of exact resonance ($\mu = 1$) between the TLAs and the field, and also to the case of initially excited atoms ($z(0) = 1$). Figure 3.1 shows the result for $z(\tau)$ of a numerical integration of (3.2.5), assuming $e(0) = 10^{-6}$, $\dot{e}(0) = 0$ and $\beta = 1$ ($z(0) = 1$ implies that $x(0) = y(0) = 0$). In fig. 3.2 we show the power spectrum of $z(\tau)$, obtained by applying a cosine bell window to the time series and then taking a 4096-point FFT. The power spectrum is broad-band with no evident periodicities. To confirm more rigorously that we have chaotic time evolution, we have computed the maximal LCE; our result, $\chi \cong 0.087$, confirms that the system is indeed chaotic in the sense of "very sensitive dependence on initial conditions".

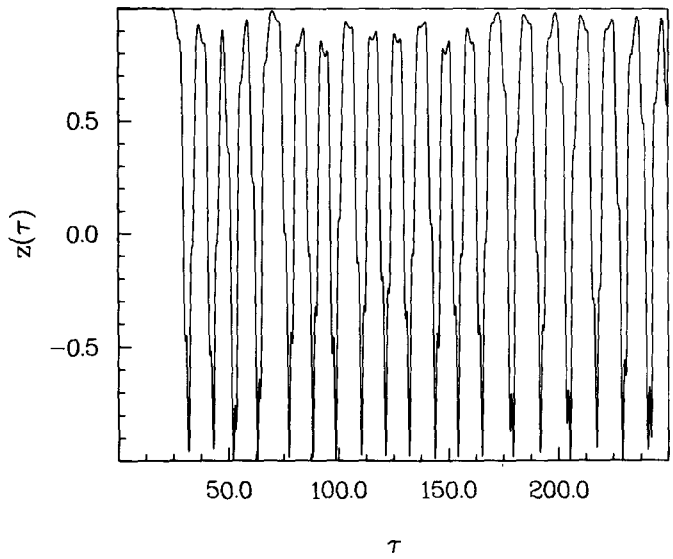

Fig. 3.1. Population difference $z(\tau)$ for $\beta = 1.0$.

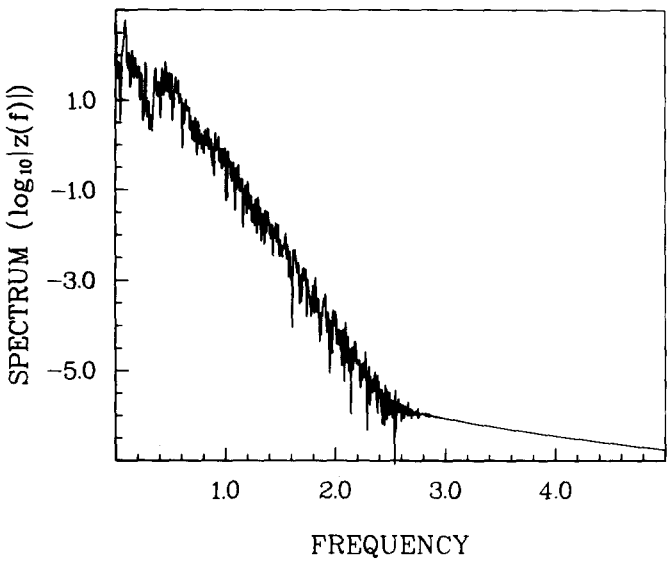

Fig. 3.2. Power spectrum of the time series of fig. 3.1.

In fig. 3.3 we show $x(\tau)$ vs. $y(\tau)$ for the case $\beta = 1$. This plot shows clearly the irregularity of the time evolution of the system. Compare fig. 3.3 with fig. 3.4, which is for the manifestly nonchaotic case $\beta = 0$, where the atoms and field are uncoupled and we are looking at just the solution of the Bloch equations.

In our numerical computations we found that the chaos becomes more pronounced as β increases. For small values of β the computation of the maximal LCE showed that χ was close to zero, but it was

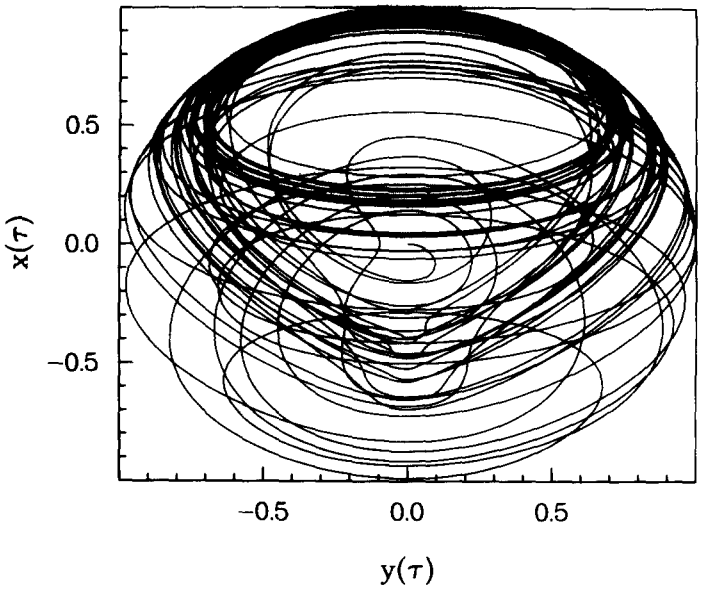

Fig. 3.3. $x(\tau)$ vs. $y(\tau)$ for $\beta = 1.0$.

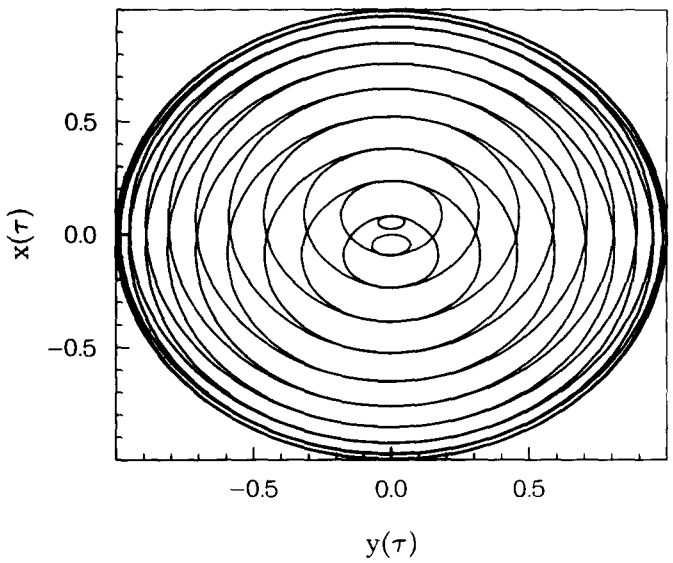

Fig. 3.4. $x(\tau)$ vs. $y(\tau)$ for the orderly case $\beta = 0$.

generally difficult to obtain convergence (in which case χ should be defined as a lim sup). The power spectra for small values of β showed marked periodicities with some "noise". Figures 3.5 and 3.6 show power spectra of $z(\tau)$ for $\beta = 0.01$ and $\beta = 0.1$, respectively. Note that the level of broad-band noise rises with increasing β. We have not found a sharp boundary between order and chaos as the β knob is varied.

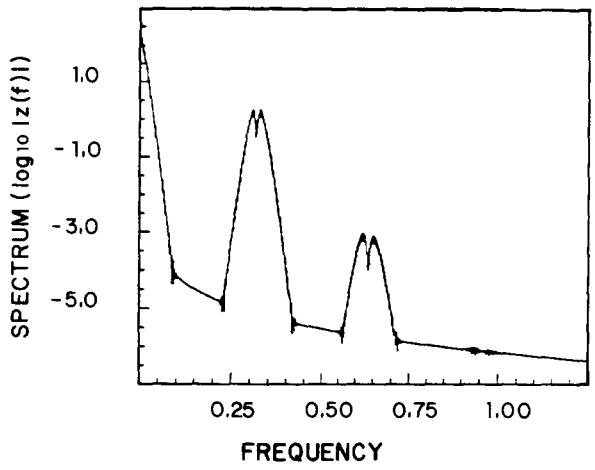

Fig. 3.5. Power spectrum of z for $\beta = 0.01$.

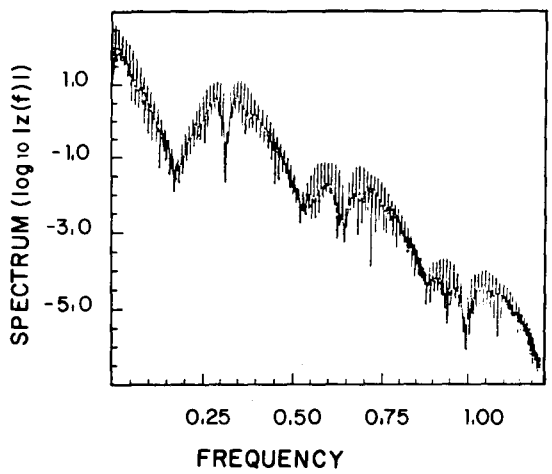

Fig. 3.6. Power spectrum of z for $\beta = 0.1$.

3.4. *Chaos and the rotating-wave approximation*

In (3.2.3) and (3.2.4) let

$$x(t) = u(t)\cos[\omega t + \phi(t)] - v(t)\sin[\omega t + \phi(t)] \tag{3.4.1a}$$

$$y(t) = u(t)\sin[\omega t + \phi(t)] + v(t)\cos[\omega t + \phi(t)] \tag{3.4.1b}$$

$$E(t) = \mathscr{E}(t)\cos[\omega t + \phi(t)] \tag{3.4.1c}$$

and assume that u, v, z, $\mathscr{E}$ and ϕ are slowly varying compared with $\sin\omega t$ and $\cos\omega t$. In this *rotating-wave approximation* (RWA) to (3.2.3) and (3.2.4) we obtain

$$\dot{u} = -(\Delta - \dot{\phi})v \tag{3.4.2a}$$

$$\dot{v} = (\Delta - \dot{\phi})u + \frac{d}{\hbar}\mathscr{E}w \tag{3.4.2b}$$

$$\dot{w} = -\frac{d}{\hbar}\mathscr{E}v \tag{3.4.2c}$$

$$\dot{\mathscr{E}} = (2\pi N d\omega)v \tag{3.4.2d}$$

$$\dot{\phi} = -(2\pi N d\omega)u/\mathscr{E} \tag{3.4.3}$$

where $\Delta = \omega_0 - \omega$ and $w(t) = z(t)$. Now (3.4.3) may be regarded as merely a definition of $\dot{\phi}$ in (3.4.2a) and (3.4.2b), since ϕ itself no longer appears in the equations. The four-dimensional autonomous system (3.4.2) has two integrals:

$$u^2 + v^2 + w^2 = 1 \tag{3.4.4}$$

and the energy integral

$$(N\hbar\omega)w + \frac{1}{4\pi}\mathscr{E}^2 = \text{const.} \tag{3.4.5}$$

This means that trajectories in the four-dimensional phase space (u, v, w, $\mathscr{E}$) are confined to a two-dimensional surface: (3.4.2) is equivalent to an autonomous system of dimension two. *The Poincaré–Bendixson theorem therefore precludes chaotic behavior of the RWA system.*

We thus have a situation analogous to that with the Duffing oscillator: When the RWA is made there is no chaos, whereas the original dynamical system without any approximations can be chaotic. The consequences of the RWA are therefore quite drastic, for it does not reveal the practical impossibility of detailed long-term prediction, i.e., very sensitive dependence on initial conditions.

3.5. Physical implications

Suppose $d = 10^{-18}$ esu and $\lambda = 10\,\mu$m. Then $\beta = 1.3 \times 10^{-22} N$, where N is the number of atoms per cm^3. This shows that relatively large number densities are typically required to reach the strongly chaotic regime $\beta \gtrsim 1$: For $\beta = 1$ we require $N \sim 8 \times 10^{21}\,\text{cm}^{-3}$. For $\lambda \sim 250\,\mu$m and $d = 3 \times 10^{-18}$ esu, corresponding to a rotational transition of the HF molecule [48], $\beta = 1$ requires $N \sim 4 \times 10^{19}\,\text{cm}^{-3}$, or a pressure of about 1.6 atm at $T = 300$ K. Thus the required number density for the strongly chaotic regime is considerably greater than that of a typical experiment in quantum optics, where the Maxwell–Bloch equations alone might provide a good model. However, much smaller densities are required for Rydberg atoms (d large). In any case our interest in this problem is at the fundamental level, for the possibility of chaos in so simple a system suggests that chaotic dynamics may be quite important in laser physics and quantum optics.

Results like that shown in fig. 3.3 indicate an effectively statistical character in the atomic dipole oscillations. The broad-band spectrum of $x(\tau)$, for instance, implies that the atomic transition is in effect broadened; the dipole correlation function will decay, indicating a loss of coherence. Belobrov, Zaslavskii and Tartakovskii [48] remarked at the end of their paper that the appearance of chaos in this system "shows that the analysis of the interaction of radiation with matter under conditions where there is a strong coupling must as a matter of principle take into account the unremovable statistical nature of the motion which in quantum optics so far has not been considered".

One thing that might be noted in connection with the RWA is that the parameter β is on the order of the Rabi frequency for the field due to all the atoms, divided by the natural transition frequency ω_0. Unless β is quite small, therefore, the RWA is not a good approximation. So it is not terribly surprising that the RWA fails to describe the (chaotic) dynamics when $\beta \sim 1$.

3.6. Remarks on the equations of motion

The analysis of Belobrov et al. [48] is based on the equations

$$\ddot{E} + \omega^2 E = 4\pi\omega^2 \mu\rho m \tag{3.6.1}$$

$$\ddot{m} + \omega^2 m = -(2\mu\omega/\hbar)\, En \tag{3.6.2a}$$

$$\dot{n} = (2\mu/\hbar\omega)\, E\dot{m} \,. \tag{3.6.2b}$$

Equations (3.6.2) are equivalent to the Bloch equations (3.2.3) with $m = x$, $\omega = \omega_0$, $\mu = d$, $n = z$. With $\rho = N$ in our notation, however, (3.6.1) is equivalent to

$$\ddot{E} + \omega^2 E = 4\pi N d\omega^2 x = 4\pi\omega^2 P \tag{3.6.3}$$

where $P = Ndx$ is the polarization density. Note that the right-hand side of (3.6.3) differs from that of (3.2.4). If we write (3.2.4) in terms of the electric displacement $D = E + 4\pi P$, however, it becomes

$$\ddot{D} + \omega^2 D = 4\pi N d\omega^2 x \tag{3.6.4}$$

which is the same as (3.6.3) if we identify E in the latter as D.

Equation (3.2.4) is a single-mode variant of the Maxwell wave equation

$$\nabla^2 E - \frac{1}{c^2}\ddot{E} = \frac{4\pi}{c^2}\ddot{P} = \frac{4\pi}{c^2} N d\ddot{x} \tag{3.6.5}$$

for the (transverse) electric field. Equations (3.2.3) and (3.6.5) are widely used as the "Maxwell–Bloch equations", although in general they are replaced by RWA equations for slowly varying amplitudes. The electric displacement D, on the other hand, satisfies

$$\nabla^2 D - \frac{1}{c^2}\ddot{D} = 4\pi\nabla^2 P \tag{3.6.6}$$

of which (3.6.4) is a special case.

Which is the correct set of equations for our problem, (3.2.3) and (3.2.4) or (3.6.1) and (3.6.2)? In spite of the wide-spread use of the Maxwell–Bloch equations in the form of (3.2.3) and (3.6.5), the system (3.6.1) plus (3.6.2) provides a somewhat more satisfactory description of the many-atom Jaynes–Cummings problem. The reasons for this have been discussed recently [53], and are based on an examination of the unitary transformation taking us from the minimal coupling Hamiltonian to the $-\boldsymbol{d}\cdot\boldsymbol{E}$ form [54]. However, since for practical purposes the different sets of equations used in refs. [48] and [49] lead to physically equivalent predictions, we will not dwell on this question here.

3.7. Quantum chaos?

A basic feature of our treatment is that the field is treated classically. This raises the very interesting question of what changes might be expected when the field is quantized. At the present time we do not have a fully quantum-mechanical treatment of the problem, although some preliminary work in this direction has been reported by Graham and Höhnerbach [55].

More generally, one can ask what is the effect of quantum mechanics on a system which, treated classically, exhibits chaotic behavior. This is the question of "quantum chaos", and it is not a trivial matter. For instance, a closed system will have a discrete energy spectrum, and expectation values of observables will therefore not have the broad-band spectra associated with classical chaos. There is also the question of how separation of initially close "trajectories" extends to a quantum system.

Various examples suggest that classical chaos does have quantum manifestations, but not always in unambiguous ways [56–58]. Among the different ideas that have been put forth to characterize quantum chaos, we mention Percival's suggestion [59, 60] that the distribution of energy eigenvalues has sensitive dependence on a control parameter, and Peres' definition of quantum chaos, according to which dynamical variables are represented by pseudo-random matrices when the Hamiltonian is diagonal [61]. The interested reader is also referred to the discussion and references given recently by Berry [62].

The model considered in this section is much more amenable to a fully quantum-mechanical treatment when the RWA is made. Even the single-atom case displays a rich "collapse and revival" behavior [63, 64], which can be interpreted in terms of the generation of incommensurate eigenfrequencies [65]. The case $N > 1$ has been considered by Barnett and Knight [66], who find that the semiclassical approximation predicts a periodic evolution of the atomic inversion, whereas the fully quantized treatment does not.

4. Chaotic lasers

4.1. Introduction

It is not unusual for lasers to have noisy and even unstable output. Ruby lasers with continuous-wave excitation, for instance, exhibit "undamped spiking" behavior, and GaAs lasers tend after a certain aging period to have a pulsating output. Such behavior is usually attributed to certain "random" factors that are not included in standard laser theory. These include such things as impurities and defects, pump variations, self-focusing, etc. Part of the art of designing a laser system is to minimize such instabilities as much as possible.

Recently, however, it has been possible to produce truly chaotic (in the sense of this article) laser output. Only a few years ago this type of laser operation would have been classified as "noisy" and not of intrinsic interest, and in any case it would have been avoided. The recent upsurge of interest in chaotic dynamics has altered this situation considerably: Experimentalists are reporting laser operation with well-defined routes to chaos. In particular, the period-doubling, Ruelle–Takens, and intermittency routes to chaos have all been observed with lasers. In this section we will review some of this recent work on chaotic lasing. Further experimental progress will no doubt occur, but it has already been established that chaotic lasing is achievable, and that the "chaos" is classifiable and in accord, at least in some cases, with theoretical expectations.

4.2. The Lorenz model and the single-mode laser

An early indication that lasers could be chaotic was provided by Haken in 1975 [67]. Consider the RWA equations (3.4.2) and (3.4.3) with $\Delta = 0$, i.e., the case of exact resonance between the atoms and the field. Adding phenomenological damping terms in the usual way [52], we obtain the system

$$\dot{u} = -\beta u - (2\pi N d\omega)uv/\mathscr{E} \tag{4.2.1a}$$

$$\dot{v} = -\beta v + (2\pi N d\omega)u^2/\mathscr{E} + (d/\hbar)\mathscr{E}w \tag{4.2.1b}$$

$$\dot{w} = -\gamma(w - w_0) - (d/\hbar)\mathscr{E}v \tag{4.2.1c}$$

$$\dot{\mathscr{E}} = (2\pi N d\omega)v - \gamma_c \mathscr{E}\,. \tag{4.2.1d}$$

Here $\beta/2\pi$ is the homogeneous linewidth (HWHM) of the transition, γ is the rate at which the population inversion relaxes to its equilibrium value w_0 in the absence of an applied field, and γ_c is the field loss rate. Assuming $w(0) = \pm 1$ implies that $u(0) = v(0) = 0$, which from (4.2.1a) means that u is identically zero. Thus (4.2.1) reduces to

$$\dot{v} = -\beta v + (d/\hbar)\mathscr{E} w \tag{4.2.2a}$$

$$\dot{w} = -\gamma(w - w_c) - (d/\hbar)\mathscr{E} v \tag{4.2.2b}$$

$$\dot{\mathscr{E}} = (2\pi N d\omega)v - \gamma_c \mathscr{E}\,. \tag{4.2.2c}$$

Equations (4.2.2) may be used to model a single-mode, homogeneously broadened laser (SMHBL), assuming line-center ($\Delta = 0$) operation. In this case γ_c is the cavity loss rate for the field, and is inversely proportional to the cavity Q:

$$\gamma_c = \frac{\omega}{2Q} = \frac{\pi\nu}{Q} = \frac{c}{2}\left[a - \frac{1}{2L}\log R_1 R_2\right] \tag{4.2.3}$$

where a is the average distributed loss coefficient, R_1 and R_2 are the mirror reflectivities, and L is the mirror separation.

The fixed points of the dynamical system (4.2.2), i.e., the steady-state solutions, satisfy the relations

$$v_s = (d/\hbar\beta)\,\mathscr{E}_s w_s \tag{4.2.4a}$$

$$w_s = w_0 - (d/\hbar\gamma)\,\mathscr{E}_s v_s \tag{4.2.4b}$$

$$\mathscr{E}_s = (2\pi N d\omega/\gamma_c)v_s \tag{4.2.4c}$$

whose solutions are well known [52]. We introduce the new variables $\tilde{v}$, $\tilde{w}$, $\tilde{\mathscr{E}}$ as follows:

$$\tilde{v} = v/v_s\,, \qquad \tilde{w} = w/w_s\,, \qquad \tilde{\mathscr{E}} = \mathscr{E}/\mathscr{E}_s\,. \tag{4.2.5}$$

In terms of these variables (4.2.2) becomes

$$\dot{\tilde{v}} = -\beta\tilde{v} + \beta\tilde{\mathscr{E}}\tilde{w} \tag{4.2.6a}$$

$$\dot{\tilde{w}} = -\gamma\tilde{w} + \gamma(\lambda + 1) - \gamma\lambda\tilde{\mathscr{E}}\tilde{v} \tag{4.2.6b}$$

$$\dot{\tilde{\mathscr{E}}} = \gamma_c(\tilde{v} - \tilde{\mathscr{E}}) \tag{4.2.6c}$$

where

$$\lambda = w_0/w_s - 1\,. \tag{4.2.7}$$

Finally let

$$r = \lambda + 1 = w_0/w_s \tag{4.2.8a}$$

$$\sigma = \gamma_c/\beta \tag{4.2.8b}$$

$$b = \gamma/\beta \tag{4.2.8c}$$

$$\tau = \beta t \tag{4.2.8d}$$

and define the new dependent variables

$$x = (b\lambda)^{1/2}\,\tilde{\mathscr{E}} \tag{4.2.9a}$$

$$y = (b\lambda)^{1/2}\,\tilde{v} \tag{4.2.9b}$$

$$z = r - \tilde{w} = (w_0 - w)/w_s\,. \tag{4.2.9c}$$

In terms of these new variables (4.2.6) may be written

$$\dot{x} = -\sigma(x - y) \tag{4.2.10a}$$

$$\dot{y} = -y - xz + rx \tag{4.2.10b}$$

$$\dot{z} = xy - bz \tag{4.2.10c}$$

where the derivatives are taken with respect to τ.

The system (4.2.10) is identical to (2.6.1). In other words, *the system* (4.2.2) *that is sometimes used to describe a SMHBL is equivalent to the Lorenz model* [67]. Obviously this suggests that a SMHBL might have chaotic output if the parameters are chosen within the chaotic regime of the Lorenz model.

Although this Lorenz-type chaos in a SMHBL seems possible, the required parameter range is highly atypical. In particular, the condition (2.6.4a) translates in a SMHBL to $\gamma_c > \beta + \gamma$, or

$$\gamma_c > 2\pi\delta\nu_0 + \gamma \tag{4.2.11}$$

where $\delta\nu_0$ is the HWHM Lorentzian linewidth of the laser transition. Now from (4.2.3) we have $\gamma_c = \frac{1}{2}cg_t$, where g_t is the threshold gain coefficient for laser oscillation, and so (4.2.11) may be written

$$\tfrac{1}{2}cg_t > 2\pi\delta\nu_0 + \gamma \tag{4.2.12}$$

which is a necessary condition for chaotic laser oscillation. However, it is exactly the opposite inequality that is satisfied in a typical SMHBL. That is, the Lorentzian width of the bare-cavity mode is usually much *smaller* than the laser transition linewidth. (In the rate-equation approximation, β is assumed to be much larger than either γ or γ_c, so that the off-diagonal elements of the TLA density matrix follow the population inversion adiabatically, and one writes coupled equations only for the population inversion and the cavity intensity [52].)

The instability conditions (2.6.4) for a SMHBL were also derived some time ago by Shirley [68], among others, who noted that the rate-equation approximation to (4.2.2) predicts only stable fixed points (steady-state solutions). It is also interesting that Buley and Cummings [69], in a numerical study of the SMHBL equations, remarked that "A case has also been run... in which the output [intensity]... appears as a series of almost random spikes". Evidently they were seeing the chaotic behavior that Lorenz, at about the same time, was studying in a completely different context!

We are not aware of any SMBHL for which *both* conditions (4.2.2) are satisfied. Since the Lorenz system has yet to be studied in an actual experimental realization, such a laser would be of considerable interest.

4.3. The Lorenz model and self-pulsing in a unidirectional ring laser

In the travelling-wave case equations (4.2.6) are

$$\partial\tilde{v}/\partial t = -\beta\tilde{v} + \beta\tilde{\mathscr{E}}\tilde{w} \tag{4.3.1a}$$

$$\partial\tilde{w}/\partial t = -\gamma\tilde{w} + \gamma(\lambda+1) - \gamma\lambda\tilde{\mathscr{E}}\tilde{v} \tag{4.3.1b}$$

$$c\,\partial\tilde{\mathscr{E}}/\partial z + \partial\tilde{\mathscr{E}}/\partial t = \gamma_c(\tilde{v} - \tilde{\mathscr{E}})\,. \tag{4.3.1c}$$

These equations have the steady-state solution $\tilde{v} = \tilde{w} = \tilde{\mathscr{E}} = 1$. The stability of this solution was investigated by Risken and Nummedal [70], who found that there can be an instability in the unidirectional ring laser without necessarily having $\gamma_c > \beta + \gamma$, a condition required for the Lorenz-type SMHBL instability. This instability corresponds to the onset of multimode, phase-locked pulsing, and requires [70]

$$r > 5 + 3b + [8(b+1)(b+2)]^{1/2} \tag{4.3.2}$$

in the notation of (4.2.8). This represents a "second laser threshold". If $b = \gamma/\beta$ is small, (4.3.2) is equivalent to $r = w_0/w_s \gtrsim 9$, i.e., the laser must be pumped about 9 times above threshold.

Risken and Nummedal found pulse-train solutions of (4.3.1) in which $\tilde{v}$, $\tilde{w}$ and $\tilde{\mathscr{E}}$ are functions of $t - z/v_p$, where v_p is a phase velocity determined by cavity boundary conditions. These solutions satisfy the ordinary differential equations

$$\dot{\tilde{v}} = -\beta\tilde{v} + \beta\tilde{\mathscr{E}}\tilde{w} \tag{4.3.3a}$$

$$\dot{\tilde{w}} = -\gamma\tilde{w} + \gamma(\lambda+1) - \gamma\lambda\tilde{\mathscr{E}}\tilde{v} \tag{4.3.3b}$$

$$\varepsilon\dot{\tilde{\mathscr{E}}} = \tilde{v} - \tilde{\mathscr{E}} \tag{4.3.3c}$$

with $\varepsilon = (1 - c/v_p)/\gamma_c$ and the derivatives are with respect to $t - z/v_p$. Equations (4.3.3) are of the same form as (4.2.6), *and therefore are isomorphic to the Lorenz system* with $r = \lambda + 1 = w_0/w_s$, $\tilde{\sigma} = 1/\beta\varepsilon = (\gamma_c/\beta)/(1 - c/v_p)$, and $b = \gamma/\beta$. It is interesting that the numerical studies of Risken and Nummedal in cases where $r < r_c$ revealed apparently stable periodic solutions, for in the corresponding Lorenz model there are no stable limit cycles for r below the critical value r_c. This difference evidently arises from the periodic boundary conditions imposed on solutions of (4.3.3) in the case of a laser cavity [71].

Graham [71] has derived (4.3.2) in a way that connects it to the Lorenz instability condition (2.6.4). Since v_p and therefore $\tilde{\sigma}$ in the present example are not specified in the equations, it is interesting to find the value $\tilde{\sigma}_{min}$ of $\tilde{\sigma}$ that minimizes r_c. From (2.6.4b) with $\sigma = \tilde{\sigma}$ we find

$$\tilde{\sigma}_{min} = (b+1) + [4(b+1)(b+2)]^{1/2} \tag{4.3.4}$$

for which

$$r_c = r_{min} = 5 + 3b + [8(b+1)(b+2)]^{1/2} \tag{4.3.5}$$

which implies the "second laser threshold" (4.3.2).

Of course the instability represented by the transition from single-mode to stable mode-locked operation in the absence of an external modulation ("self-pulsing") is not a transition to chaos. In some experiments, however, it is found that the successive pulses in a mode-locked train are different, and this could be a form of chaotic lasing. In this connection we mention an experiment of Kaufmann and Marowsky [72], on the "order transition" of a passively mode-locked dye laser, where they investigated the mode-locking properties of the laser as the concentration of the mode-locking dye was varied. These authors described a model in which the field–matter interaction involved primarily the *passive* dye, while the active dye medium was characterized in first approximation by a constant linear gain coefficient. In such a model $r = w_0/w_s > 0$ is satisfied because w_0, $w_s < 0$, and the authors argued that self-pulsing in their ring laser might occur if the concentration of the passive dye were large enough. They did observe the onset of mode locking as they increased the concentration of the passive dye, although for large concentrations the mode locking was no longer observed; the latter effect could not be explained with their crude model. For an intermediate range of passive dye concentrations they observed "irreproducible, incoherently superimposed transient pulse trains of small modulation depth [72]", which possibly was chaotic lasing.

Chaotic solutions of systems like (4.3.1) are known to exist, but do not seem to correspond very well to actual laser devices [73]. However, various instabilities in a homogeneously broadened ring dye laser are reported by Hillman et al. [74]. Such "intrinsic" instabilities of the Haken–Lorenz or Risken–Nummedal type are more readily observed in *inhomogeneously* broadened systems, as we shall see.

4.4. Chaos in a Q-switched CO_2 laser

The first observation and characterization of chaos in a quantum-optical molecular system was reported by Arecchi et al. in 1982 [75]. The CO_2 laser they employed was such that the rate-equation approximation for a SMHBL is applicable. Here we describe their model and experimental results.

If $\beta \gg \gamma$ it may be assumed in (4.2.2) that $v(t)$ follows $w(t)$ adiabatically:

$$v(t) \cong (d/\hbar\beta)\, \mathscr{E}(t)\, w(t)\,. \tag{4.4.1}$$

Therefore (4.2.2b) and (4.2.2c) become

$$\dot{w}(t) = -\gamma[w(t) - w_0] - (8\pi d^2 w/\hbar\beta V)^{1/2}\, n(t)\, w(t) \tag{4.4.2a}$$

$$\dot{n}(t) = (4\pi d^2\omega/\hbar\beta)\, N\, n(t)\, w(t) - 2\gamma_c\, n(t) \tag{4.4.2b}$$

where $n(t)$ is the cavity photon number, i.e.,

$$I(t) = \frac{c}{8\pi}\mathscr{E}(t)^2 \equiv \frac{c\hbar\omega}{V} n(t) \tag{4.4.3}$$

and V is the "mode volume" of the intracavity field. Following Arecchi et al., we define the quantities

$$\Delta = NVw(t), \qquad G = 4\pi d^2\omega/\hbar\beta V$$
$$R = NV\gamma w_0, \qquad K = 2\gamma_c \tag{4.4.4}$$

in terms of which (4.4.2) has the form

$$\dot{\Delta} = R - 2Gn\Delta - \gamma\Delta \tag{4.4.5a}$$

$$\dot{n} = Gn\Delta - Kn. \tag{4.4.5b}$$

As noted earlier, these approximate rate equations have no unstable fixed points. In any case they cannot, according to the Poincaré–Bendixson theorem, have chaotic time evolution, because they form an autonomous system of order 2. The situation is changed completely, however, if the cavity loss is time-dependent, for then the order of the equivalent autonomous system is >2. Arecchi et al. modulated the cavity loss of a CO_2 laser in such a way that

$$K \to K_1(1 + m\cos\Omega t). \tag{4.4.6}$$

In their device $\beta/\gamma \approx 10^5$, and so eqs. (4.4.5) are applicable, with K given by (4.4.6). Numerical simulation of this system predicts a period-doubling sequence and a chaotic regime for a certain range of modulation frequencies Ω, *and such behavior was in fact observed experimentally.*

Obviously the cavity loss modulation in this example is crucial to the observation of chaos. As noted earlier, intrinsic instabilities and chaos are more readily observed in inhomogeneously broadened systems. For instance, chaotic emission has been observed in He–Xe and He–Ne lasers. We now turn our attention to some experimental and theoretical work on instabilities and chaos in inhomogeneously broadened lasers.

4.5. Self-pulsing in the case of inhomogeneous broadening

Low-pressure electric-discharge Xe and He–Xe lasers have large small-signal gains and are highly inhomogeneously (Doppler) broadened. The strong 3.508 μm line may have a gain $\sim 1\,\mathrm{cm}^{-1}$ with a Doppler width $\delta\nu_D \sim 100$ MHz [76]. This combination of high gain and narrow linewidth leads to particularly strong resonant dispersion effects such as frequency pulling [76].

The coupled Maxwell–Bloch equations for a Doppler-broadened, single-mode, two-level laser medium, generalized to allow upper- and lower-level decay, have been solved numerically by Casperson [77]. He finds a self-pulsing instability for a range of reasonable parameter values. Figure 4.1 shows numerical results for the field and intensity, assuming parameter values appropriate to a 3.51 μm Xe laser at a pressure of 5×10^{-3} Torr [77]; in particular, the collisional de-phasing time $T_2 \sim 0.9$ μs. The

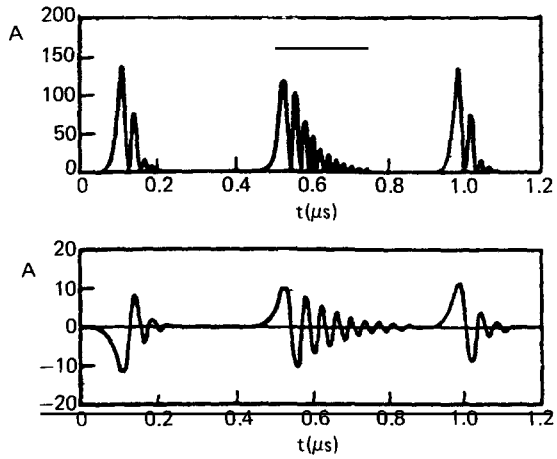

Fig. 4.1. Theoretical plots of the self-pulsing in a 3.51 μm xenon laser. (Courtesy of L.W. Casperson, copyright IEEE 1978.)

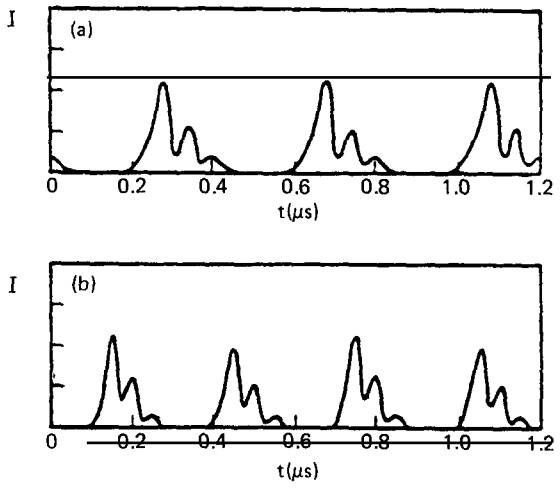

Fig. 4.2. Experimental plots of the self-pulsing for discharge currents of (a) 40 mA and (b) 50 mA. (Courtesy of L.W. Casperson, copyright IEEE 1978.)

pulse variations shown in fig. 4.1 are fast compared with this dipole coherence time, and Casperson emphasized that this instability cannot be derived from rate-equation analyses. Furthermore the pulsing is slow compared with a cavity transit time $2L/c$, and the analysis is single-mode, so there is no connection with mode-locked pulsing. This self-pulsing instability was found to apply only to the case of inhomogeneous broadening, and did not appear far above threshold [77].

What is especially interesting is that Casperson observed the kind of behavior shown in fig. 4.1 *experimentally*. Figure 4.2 shows experimental plots of intensity for two different discharge currents. We note that as the current was increased from 40 to 50 mA a period-doubling seems to have occurred. At a current of 70 mA a chaotic output, with a broad spectrum, was observed [78].

For the numerical results shown in fig. 4.1 $\gamma_c \sim 1\times 10^9\,s^{-1}$, $\beta \sim 2.5\times 10^7\,s^{-1}$ and $\gamma \sim 2\times 10^7\,s^{-1}$ (γ is actually the *lower*-level decay rate in this case). Thus the "bad-cavity" condition $\gamma_c > \beta + \gamma$, eq. (4.2.11), is satisfied. Since $\gamma_c = cg$ and $\beta = 2\pi\delta\nu_0$, $\delta\nu_0$ being the homogeneous linewidth, we can write this condition in the useful form [78]

$$cg/2\pi\delta\nu_0 > 1 \tag{4.5.1}$$

if $\gamma \ll \beta$. This puts a necessary condition on the (threshold) gain coefficient g of the medium for the self-pulsing instability to be realized.

Casperson [79] has presented a stability analysis of the semiclassical laser equations that were solved numerically earlier [77], and has derived (4.5.1) under some reasonable approximations. He interprets the self-pulsing instability in a bad-cavity inhomogeneously broadened laser in terms of *mode splitting*. Mode splitting arises from the strong resonant (or "anomalous") dispersion in a high-gain laser medium, and leads to the possibility that more than one frequency may be associated with the same longitudinal mode (wavelength) [76]. It may be understood as follows. If L and l are the lengths of the cavity and gain tube, respectively, and $n(\omega)$ is the refractive index, the mode condition is

$$m\lambda/2 = (L-l) + l\,n(\omega), \qquad m = \text{positive integer} \tag{4.5.2}$$

or

$$\frac{l}{L}[n(\omega)-1]\omega = \omega_m - \omega \tag{4.5.3}$$

where $\omega_m = mc/L$ is a bare-cavity mode frequency and ω is the laser oscillation frequency. Equation (4.5.2) predicts that there may be several frequencies ω associated with the same mode index m, depending on $n(\omega)$, and these frequencies can lase simultaneously if they have gain > loss. For a Doppler-broadened line the resonant refractive index is given by

$$n(\omega)-1 = \frac{cg(\omega_0)}{\pi^{1/2}\omega} F(x) \tag{4.5.4a}$$

with

$$x = \sqrt{\frac{\log 2}{\pi^2}} \frac{\omega - \omega_0}{\delta\nu_D} \tag{4.5.4b}$$

where $g(\omega_0)$ is the line-center gain coefficient, $\delta\nu_D$ is the Doppler linewidth (FWHM), and $F(x)$ is Dawson's integral [80]. The solution of eq. (4.5.3) for the oscillation frequency ω is obtained from the intersection of the line $y = \omega_m - \omega$ with the dispersion curve $y = (l/L)[n(\omega)-1]$, as indicated in fig. 4.3 [76]. It can be seen that this "spontaneous mode splitting" effect [81], wherein several frequencies can lase on a single longitudinal mode, occurs only when the frequencies are appreciably displaced from line center.

Thus far we have ignored the possibility that spectral holes can be burned into the resonant

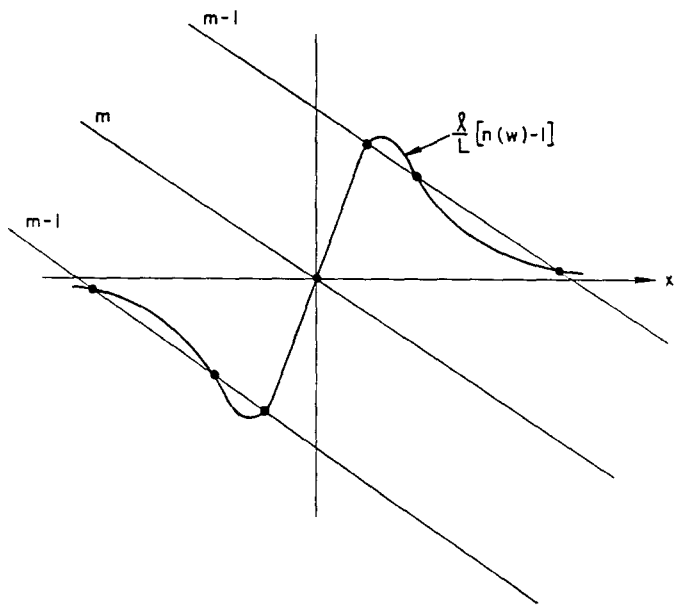

Fig. 4.3. Solutions of eq. (4.5.3). (See text.)

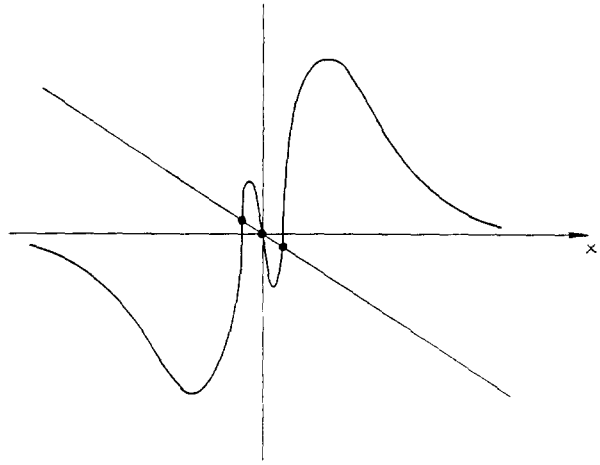

Fig. 4.4. Effect of hole burning on solutions shown in fig. 4.3.

dispersion curve. Figure 4.4 shows what can happen when this hole burning due to a line-center mode is taken into account [79]. Now a mode splitting close to line center can occur, and the allowed frequencies can be expected to lase. (Note that they are away from the dip burned into the center of the gain curve, and so have small-signal gains greater than the gain of the saturating line-center mode.) This "induced mode splitting" [81] is strongest at line center. It is plausible that pulse formation results from the phase locking of the allowed oscillating frequencies.

The Casperson and Risken–Nummedal self-pulsing instabilities are similar in the sense that they are both "intrinsic" instabilities understandable from the same Maxwell–Bloch equations. However, the Casperson instability associated with mode splitting arises out of the dispersive part of the atomic susceptibility, and so in another sense is of a different physical origin. The most important difference is that the Casperson instability does not require the laser to be typically nine times above threshold, as for the Risken–Nummedal instability. Thus the Casperson instability is more easily observed, although it does require the atypical parameter relation (4.5.1) ("bad cavity"), which is not necessarily required for the Risken–Nummedal instability in a homogeneously broadened ring laser [71]. The fact that inhomogeneous broadening leads to a more readily observable instability has been discussed by Minden and Casperson [82] and Mandel [83]. Casperson [84] has also investigated the case of non-Doppler inhomogeneous broadening.

Abraham et al. [81, 85] have observed self-pulsing in a single-mode He–Xe laser, and gave strong evidence that this was due to either spontaneous or induced mode splitting, depending on the detuning of their cavity from line center. They also found a (single) period-doubling in the output pulsations. Period-doubled and two-frequency self-pulsing were also observed in a bad-cavity 3.39 μm He–Ne laser, and for a small range of cavity detunings the pulsations appeared to be chaotic [86].

4.6. Chaos in inhomogeneously broadened lasers

A simplified analysis of the single-mode self-pulsing instability suggests that, for either homogeneous or inhomogeneous broadening, it is associated with a Hopf bifurcation [83]. The experimental observations mentioned above clearly indicated that this transition from a cw steady state to a periodic

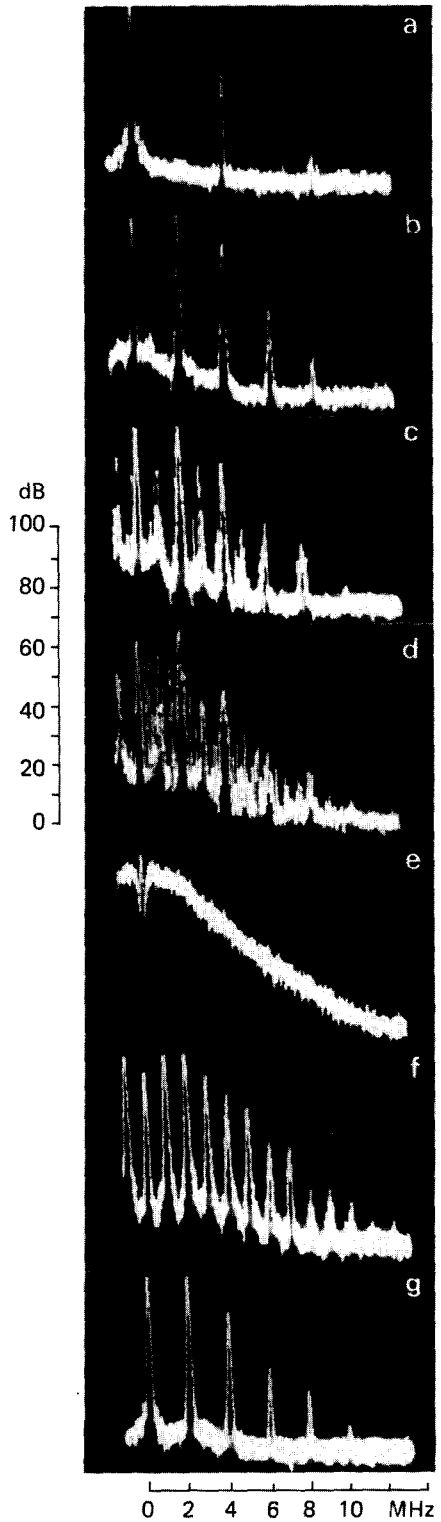

Fig. 4.5. Three period-doublings (a–d) and chaos (e), followed by orderly oscillation (f and g), as one of the mirrors of a 3.39 μm He–Ne laser is tilted. The spectra shown correspond to sidebands of intermode beats. (Courtesy of C.O. Weiss.)

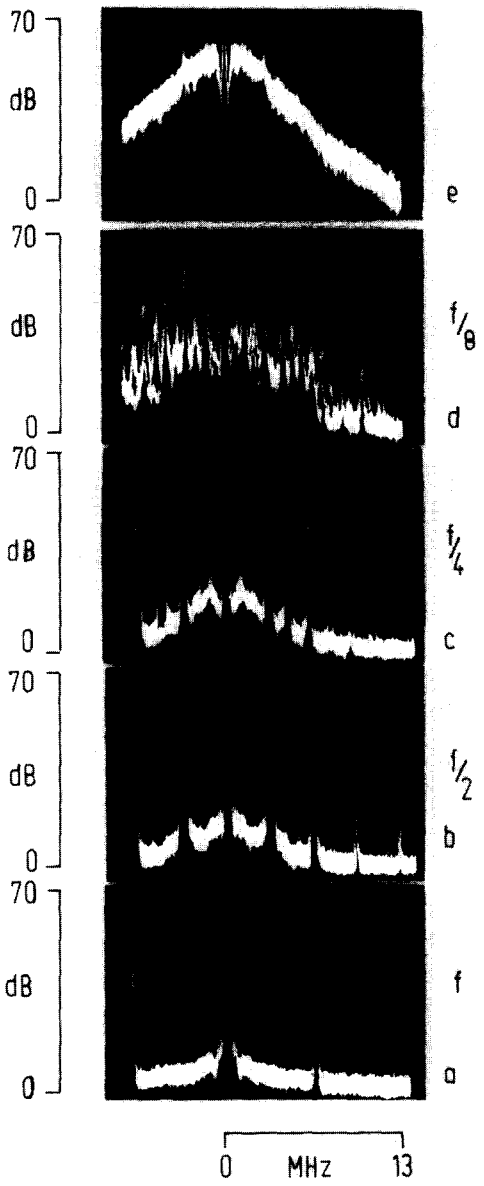

Fig. 4.6. Period-doubling route to chaos in a 3.39 μm He–Ne laser as one mirror is tilted. (Courtesy of C.O. Weiss.)

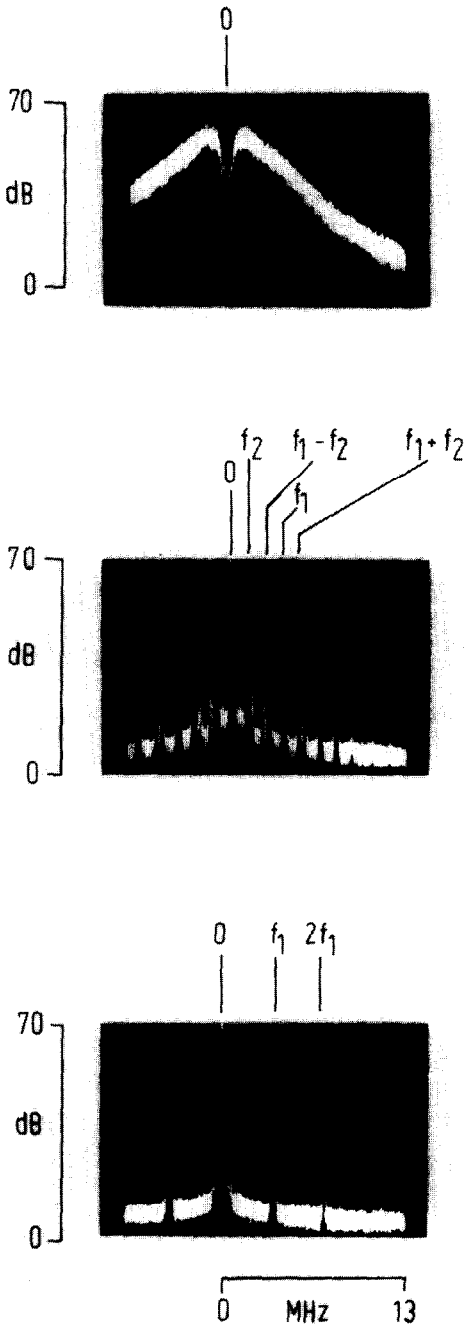

Fig. 4.7. Two-frequency (Ruelle–Takens) route to chaos in a 3.39 μm He–Ne laser as one mirror is tilted. (Courtesy of C.O. Weiss.)

output might be followed by more complicated and even chaotic behavior. Although more experimental progress will certainly be made, it has already been established that lasers under certain conditions may be intrinsically chaotic. Furthermore the period-doubling, Ruelle–Takens (or two-frequency), and intermittency "scenarios" have been realized with lasers. We have already mentioned the period-doubling route to chaos observed in a loss-modulated CO_2 laser by Arecchi et al. [75], and now focus our attention on the "intrinsically" chaotic behavior that has been found in inhomogeneously broadened lasers. The observation of different routes to chaos in an inhomogeneously broadened laser was recently reported by Weiss et al. [87, 88] and by Gioggia and Abraham [89].

Weiss and King [87] used a high-gain 3.39 μm He–Ne laser having a resonator free spectral range ($c/2L$) of 60 MHz. By tilting one of the resonator mirrors they observed three period doublings and then chaos, as shown in fig. 4.5, and then an orderly oscillation again. The total tilt angle in going from fig. 4.5a to fig. 4.5g was only about 2×10^{-4} radian. The spectra shown in fig. 4.5 correspond to *sidebands* of the intermode beats ("beat-beat frequencies").

Weiss, Godone and Olafsson [88] modified the experiment by introducing a second, Lamb-dip stabilized laser. By heterodyning this second laser with the test laser, they could control the frequency (resonator length) of the latter. They found three routes to chaos – period-doubling, two-frequency, and intermittency – as the mirror was tilted. The particular route taken to chaos depended upon the degree of detuning from the center of the gain curve of the single-mode laser with no mirror tilt. Their experimental results for period-doubling and two-frequency (Ruelle–Takens) routes to chaos are shown in figs. 4.6 and 4.7, respectively. Figure 4.8 shows their experimental evidence for the intermittency route to chaos.

Although a theoretical analysis of this chaotic behavior is not at present available, it seems clear that the chaos is closely associated with the presence of *three* longitudinal modes. With no mirror tilt the laser operated on a single longitudinal mode, whereas when the mirror was tilted two additional modes, separated from the original one by $c/2L$, began to lase and increase in intensity with the tilt angle. Phase locking of the modes is also a closely related consideration [88].

Gioggia and Abraham [89] also reported period-doubling, two-frequency, and intermittency routes to chaos in an inhomogeneously broadened laser, this time a bad-cavity 3.51 μm Xe laser. The free spectral range of their resonator, however, was quite large (~900 MHz), so this was certainly *single*-mode chaotic emission. The different routes to chaos were observed in different ranges of detuning from line center, and each route could be followed as the detuning was varied. Some of their data showing period-doubling and two-frequency routes to chaos are shown in fig. 4.9. Here again no theoretical analysis is yet available, although it seems likely that mode splitting plays an important role. In any case the instability here is certainly distinct from that in the experiments of Weiss et al. [87, 88] as it involves only one longitudinal mode.

Chaos in a three-mode 3.39 μm He–Ne laser was also observed by Halas et al. [90]. As in the experiments of Weiss et al. [87, 88] the chaotic behavior appears in the low-frequency secondary beats when the laser is not mode-locked. In this case, however, the chaos is observed as the discharge current is varied, not by misaligning a resonator mirror. The origin of the instabilities may nevertheless be similar. Chaotic emission has also been observed in a Xe ring laser [91]. For details of all these observations the reader is referred to the cited literature.

4.7. Numerical experiments with Maxwell–Bloch equations

When damping terms and Doppler broadening are taken into account, and each level has its own

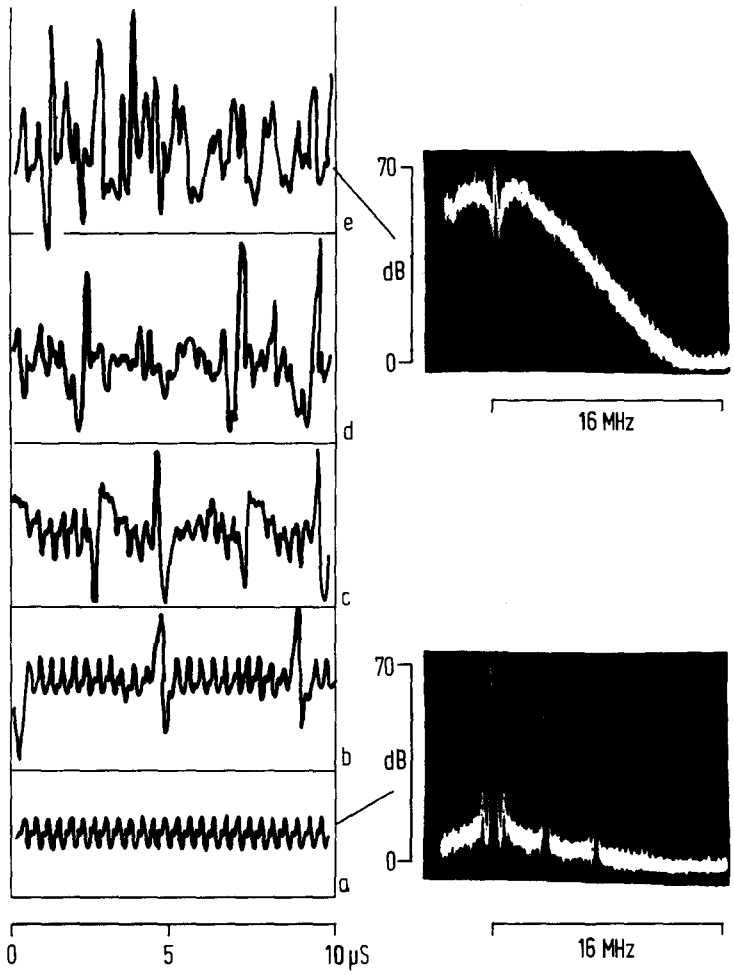

Fig. 4.8. Intermittency route to chaos in a 3.39 μm He-Ne laser as one mirror is tilted. (Courtesy of C.O. Weiss.)

pumping and relaxation rates, the system (3.4.2) plus (3.4.3) is replaced by

$$\dot{u} = -(\Delta - \dot{\phi} - ks)v - \beta u \tag{4.7.1a}$$

$$\dot{v} = (\Delta - \dot{\phi} - ks)u - \beta v + \Omega(z_2 - z_1) \tag{4.7.1b}$$

$$\dot{z}_2 = R_2 - \gamma_2 z_2 - \tfrac{1}{2}\Omega v \tag{4.7.1c}$$

$$\dot{z}_1 = R_1 - \gamma_1 z_1 + \tfrac{1}{2}\Omega v \tag{4.7.1d}$$

$$\dot{\Omega} = -\gamma_c \Omega + A \int_{-\infty}^{\infty} \mathrm{d}s\, W(s)\, v(s, t) \tag{4.7.1e}$$

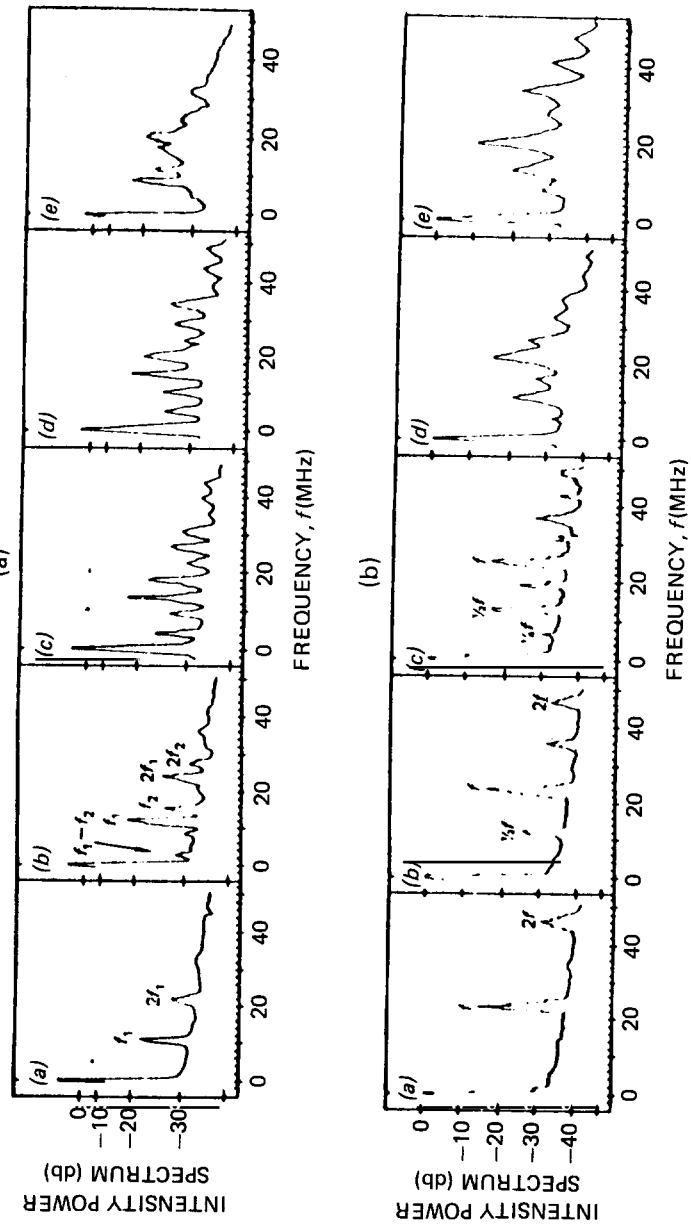

Fig. 4.9. Two-frequency (a) and period-doubling (b) routes to chaos in a 3.51 μm Xe laser. (Courtesy of N.B. Abraham.)

$$\dot{\phi}\Omega = -A \int_{-\infty}^{\infty} ds\, W(s)\, u(s, t)\,. \tag{4.7.1f}$$

These equations have been written in terms of the Rabi frequency $\Omega = d\varepsilon/\hbar$. z_2 and z_1 are the upper- and lower-level occupation probabilities, respectively, with pumping rates R_2, R_1 and damping rates γ_2, γ_1. $W(s)$ is the (one-dimensional) Maxwell–Boltzmann velocity distribution function: $W(s) = (s\pi^{1/2})^{-1} \exp(-s^2/x^2)$, where $x = (2RT/M)^{1/2}$ is the most probable speed at temperature T and molecular weight M. ks is the (angular-frequency) Doppler shift for an atom with velocity s along the optical axis, and we have defined $A = 2\pi N d^2 \omega/\hbar$. Finally γ_c is the field damping rate, as in (4.2.3).

Equations (4.7.1) describe a unidirectional, Doppler-broadened ring laser. A numerical study of this system has been made by Shih et al. [92], who find period-doubling, two-frequency, and intermittency routes to chaos as a parameter (e.g., γ_c or R_2) is varied, provided the bad-cavity condition ($\gamma_c > \beta$) is satisfied. These numerical results, based on realistic values of the various pumping and relaxation rates, demonstrate once again the importance and relevance of chaotic dynamics to quantum optics and electronics.

Figure 4.10a shows the intensity computed from (4.7.1) for the following parameters: $\beta = 61 \times 10^6\ s^{-1}$, $R_1 = 0$, $R_2 = 8.5 \times 10^{-9}\beta$, $\gamma_c = 5.4\beta$, $\gamma_1 = 0.8\beta$, $\gamma_2 = 0.012\beta$, $A = 6.4 \times 10^{23}\ s^{-2}$, $\Delta = 0$, and a Doppler

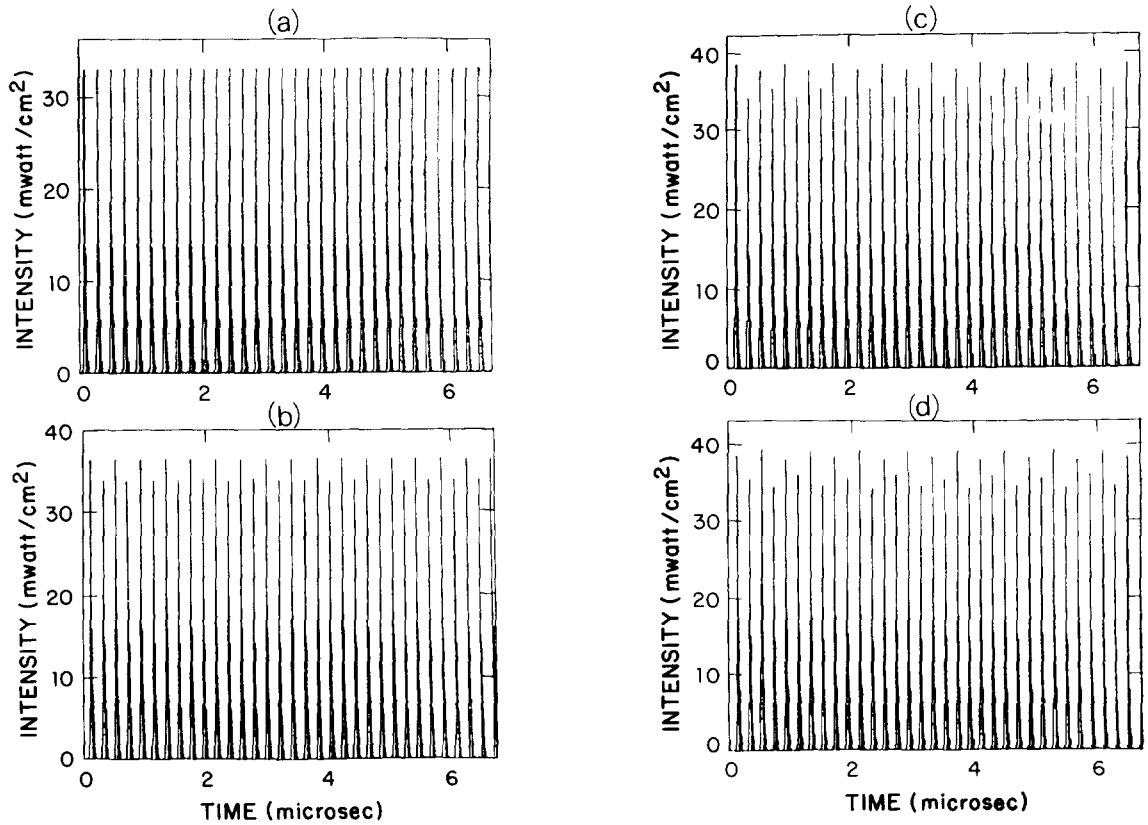

Fig. 4.10. Period-doubling route to chaos as the pump rate R_2 is increased. (See text.)

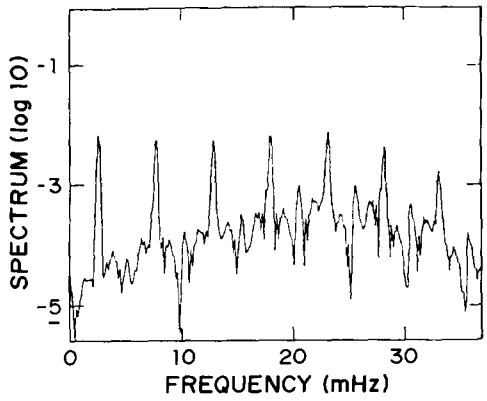

Fig. 4.11. Power spectrum of the electric field after the period-doubling sequence has proceeded *ad infinitum*, showing the broad-band component typical of chaotic dynamics.

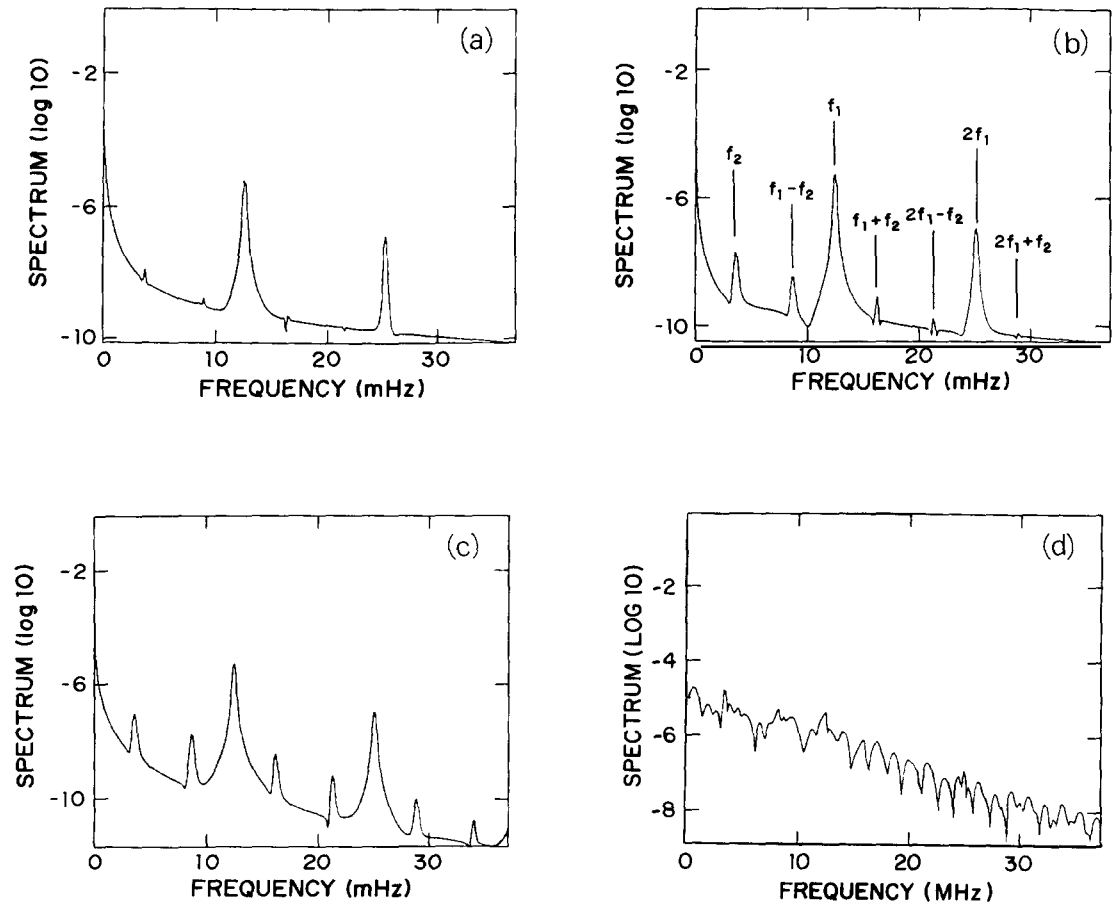

Fig. 4.12. Development of chaos after the appearance of two incommensurate frequencies f_1 and f_2 in the spectrum. (See text.)

width (FWHM) $\delta\nu_0 = kx\sqrt{\log 2}/\pi = 110$ MHz. These choices are discussed in ref. [92]. In fig. 4.10a and throughout this section we plot results only after initial transients die out. In each case we assume $u = v = z_1 = z_2 = 0$ initially, with Ω having some small initial value in order to start the laser. In a fully quantized approach the initial "noise" arises from spontaneous emission.

Figure 4.10b shows the computed intensity when R_2 is raised to $9.0 \times 10^{-9}\beta$. In going from fig. 4.10a to fig. 4.10b we see that a period-doubling bifurcation has occurred. Figures 4.10c and 4.10d show the intensity for $R_2 = 9.3 \times 10^{-9}\beta$ and $9.4 \times 10^{-9}\beta$, respectively, revealing further period doublings. Slight further increases in R_2 result in more period doublings and chaos as the period doubles *ad infinitum* according to the Feigenbaum sequence. Figure 4.11, for instance, shows the power spectrum of $\Omega(t)$ for $R_2 = 9.6 \times 10^{-9}\beta$.

In figs. 4.12a–4.12d we show the power spectrum of the electric field for the same parameters as above, but with R_2 fixed at $5.6 \times 10^{-9}\beta$ and the detuning Δ increasing from 3.725β to 3.75β. What we are seeing now is a two-frequency route to chaos, in which the dynamics becomes chaotic following the appearance of two incommensurate frequencies (i.e., motion on a two-torus in phase space).

In some numerical experiments we have also found chaos developing via intermittency. Figure 4.13

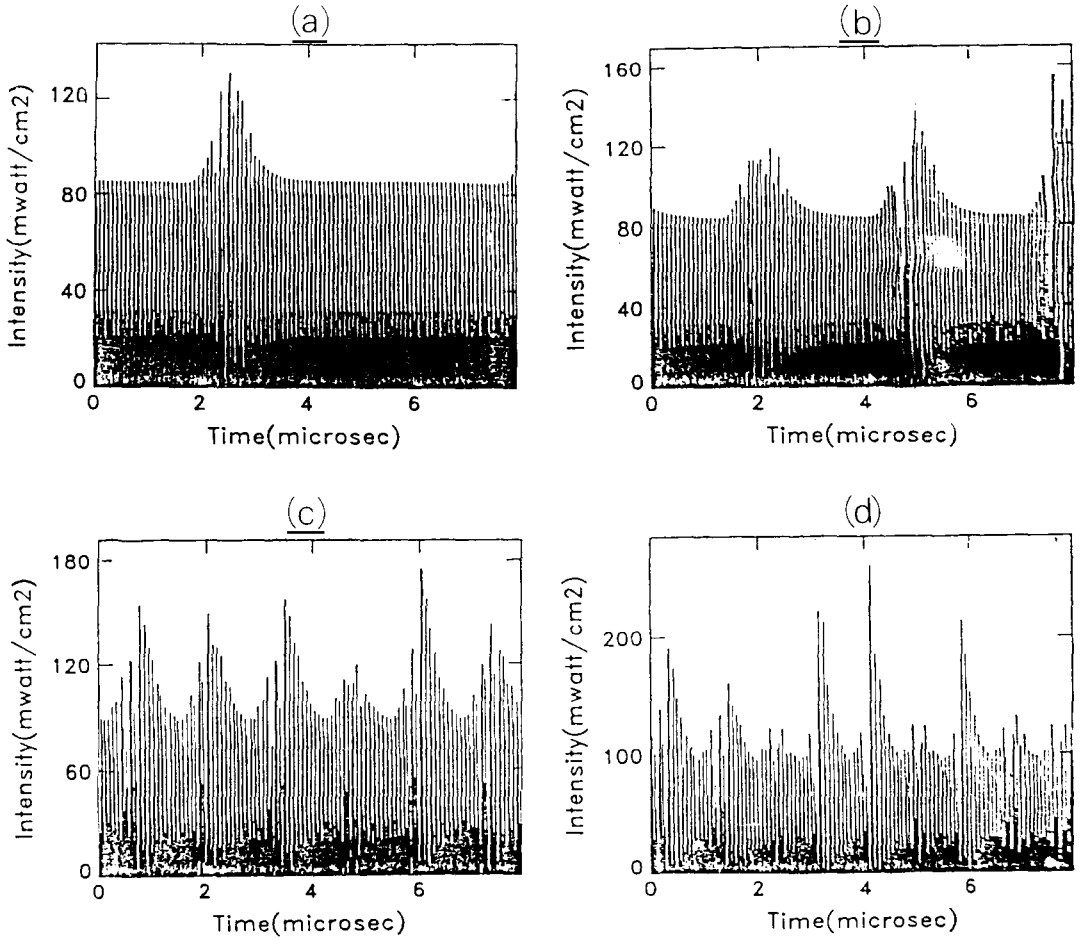

Fig. 4.13. Development of chaos via increasingly frequent irregular bursts. (See text.)

shows an example of such a route to chaos as R_2 is increased, for a somewhat different range of parameters than in figs. 4.10–4.12 [93].

The system (4.7.1) assumes a unidirectional ring, not a standing-wave or bidirectional ring device. Although the traveling-wave assumption may be a good approximation [78], the most direct comparison of our computations with experiment would be for a truly unidirectional device. Chaos in a bad-cavity unidirectional ring laser has now been observed by Urbach et al. [94], but we do not at present have any corresponding numerical results, as our computations assumed parameters more appropriate to the Gioggia–Abraham experiments [89]. In any case we believe from numerical experiments done thus far that a one-to-one comparison of theory and experiment will be very difficult without highly accurate values for the various rates and cross sections; small changes in these parameters can dramatically alter the solutions of (4.7.1).

From numerical results like those shown in figs. 4.10–4.13 we can nevertheless draw an important conclusion: Standard semiclassical laser theory, with its traditional simplifying assumptions like plane-wave fields and constant pump rates, predicts the same "universal" routes to single-mode chaos that have been observed experimentally. It is also quite interesting that the fundamental system (4.7.1), which has been known and studied for a long time in quantum electronics, displays all this rich chaotic behavior of so much current interest.

4.8. Remarks

The ubiquity of a few "universal" routes to chaos is one reason why the subject is attracting so much interest. Deterministic chaos seems to explain the transition from laminar to turbulent fluid flow [95], and lasers have now been added to the wide variety of nonlinear systems in which chaos has been observed and characterized. This possibility of understanding at least some aspects of "turbulence", with relatively simple models, certainly must count as a fundamental breakthrough.

Now that some pioneering experiments have been reported, it is expected that laser physicists will take an increased interest in chaotic lasing, and that observations will be made on many more systems. It would be especially interesting now to investigate the possibility of chaotic behavior in somewhat more typical lasers. Furthermore there is clearly room for more theoretical analyses of the chaotic lasers already studied experimentally. One might also ask whether there are interesting photon-statistical aspects of chaotic laser radiation [92]. In closing this section we will briefly mention some other work that has come to our attention. The list is by no means exhaustive, and it is expected that more developments will occur by the time this introductory review is published.

Yamada and Graham [96] and Scholtz et al. [97] have considered a SMHBL with modulated external field and population inversion, respectively, both leading to chaos. In the latter case the chaos develops via intermittency. Mayr et al. [73] find chaotic behavior in the self-pulsing described by equations for a ring SMHBL. Arecchi et al. have observed chaos in a laser with an injected signal [98]. Graham and Cho [99] have described two simplified models of self-pulsing and chaos in a single-mode inhomogeneously broadened laser, and compare the chaotic behavior with that for the Lorenz model.

The multimode case, of course, has well-known theoretical complexities. The strong-signal theory in the case of Doppler broadening has been aptly described as "horrendous, to say the least" [100]. With regard to chaos, some interesting progress along the lines of the original Lamb third-order theory has been made by Brunner and Paul [101] for the Doppler limit. They find that the assumption of free-running operation [102], which allows one to write equations for intensities only, becomes invalid when the homogeneous linewidth $\gtrsim$ twice the mode spacing. In this case the numerical analysis suggests

that the multimode oscillation is chaotic. Brunner and Paul note that this prediction seems consistent with the irregular spiking behavior of argon-ion lasers at high excitation [103].

It is also possible that spatial inhomogeneities in the pumping of a laser can lead to chaotic emission as a result of coupling of different transverse modes [104]. A related conclusion has been reached by Hauck et al. [105], and they provide some experimental evidence using a solid-state device. In the model described in ref. [104] there is a period-doubling route to chaos [92, 93].

5. Chaos in nonlinear optics

5.1. Introduction

It should by now come as no surprise to the reader that chaotic behavior can occur in various sorts of nonlinear optical processes. Thus far most of the attention in this area of "optical turbulence" has focused on optical bistability. However, it seems likely that other examples of chaos will be found in nonlinear optics as interest in chaos and nonlinear dynamics continues to grow. In the following section we describe how chaos can arise in optically bistable devices, and point to some of the experimental work on this aspect of optical bistability. We also consider examples involving coupled wave equations for Raman and Brillouin scattering, which suggest other examples where chaos may appear in nonlinear optics.

5.2. Chaos in optical bistability

A system may be said to be bistable if it has two possible output states for the same input state. An optical bistable device is generally defined to have two possible output states for the same input intensity. A comprehensive review of optical bistability has been given by Abraham and Smith [106]. The concept goes back to early papers by Szöke et al. [107] and McCall [108]. Here we consider the possibility, first discussed by Ikeda [109], of chaotic behavior, or "optical turbulence", in an optically bistable device.

The system of interest is illustrated in fig. 5.1. Mirrors 1 and 2 have reflectivity $R = 1 - T < 1$, whereas mirrors 3 and 4 are assumed to be perfect reflectors. The cell inside this cavity contains N two-level atoms per unit volume. E_I denotes the field strength of the monochromatic input field, and the transmitted and intracavity fields are denoted by E_T and E, respectively. The cell length is L, the total ring circuit length is $\mathscr{L}$, and we denote the difference by $l = \mathscr{L} - L$.

The system of fig. 5.1 is described by the Maxwell–Bloch equations, together with the cavity boundary conditions. The major differences between this device and a laser is that the medium is an absorber rather than an amplifier ($w_0 = -1$), and there is an injected field E_I. Generalizing equations (3.4.2) and (3.4.3) to allow a z-dependent field amplitude and phase, we write

$$\partial u/\partial \tau = -\Delta v - \beta u \tag{5.2.1a}$$

$$\partial v/\partial \tau = \Delta u - \beta v + (d/\hbar)\mathscr{E} w \tag{5.2.1b}$$

$$\partial w/\partial \tau = -\gamma(w+1) - (d/\hbar)\mathscr{E} v \tag{5.2.1c}$$

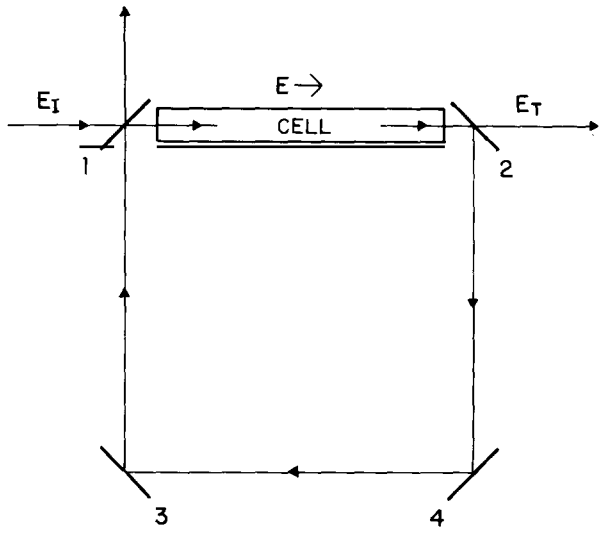

Fig. 5.1. Ring cavity configuration for an optically bistable device.

$$\partial \mathscr{E}/\partial z = (2\pi N dk)v \tag{5.2.1d}$$

$$\mathscr{E}\,\partial\phi/\partial z = -(2\pi N dk)u \tag{5.2.1e}$$

where $\tau = t - z/c$ and $k = \omega/c$. Loss is assumed to occur only at the mirrors, so that $\gamma_c = 0$, and the absorber is assumed to be homogeneously broadened.

Let us assume that β is large enough that

$$u \cong -\frac{\Delta}{\beta} v \tag{5.2.2a}$$

$$v \cong \frac{\Delta}{\beta} u + \frac{1}{\beta}\left(\frac{d}{\hbar}\mathscr{E} w\right) \tag{5.2.2b}$$

in (5.2.1). In this rate-equation approximation to the TLA Bloch equations we replace (5.2.1) by

$$\frac{\partial w}{\partial \tau} = -\gamma(w+1) - \left(\frac{\beta d^2/\hbar}{\Delta^2+\beta^2}\right)|E|^2 w \tag{5.2.3a}$$

$$\frac{\partial E}{\partial z} = \left(\frac{2\pi N d^2 k/\hbar}{\Delta^2+\beta^2}\right)(\beta + i\Delta)\,Ew \tag{5.2.3b}$$

where $E \equiv \mathscr{E}\, e^{i\phi}$. From (5.2.3) it follows by simple manipulations that

$$E\left(\tau+\frac{z}{c}, z\right)=E(\tau, 0)\exp\left[\frac{2\pi Nd^2k/\hbar}{\Delta^2+\beta^2}(\beta+\mathrm{i}\Delta)\,W(\tau, z)\right] \tag{5.2.4a}$$

$$\frac{\partial}{\partial\tau}W(\tau, z)=-\gamma[W(\tau, z)+z]-\frac{1}{4\pi N\hbar k}|E(\tau, 0)|^2\left\{\exp\left[\frac{4\pi Nd^2k\beta/\hbar}{\Delta^2+\beta^2}W(\tau, z)\right]-1\right\} \tag{5.2.4b}$$

where

$$W(\tau, z)\equiv\int_0^z \mathrm{d}z'\, w\left(\tau+\frac{z'}{c}, z'\right). \tag{5.2.4c}$$

We must also specify the cavity boundary conditions, which may be conveniently written in terms of the fields at the ends of the absorption cell [109]:

$$E(t, 0)=\sqrt{T}\,E_{\mathrm{I}}(t)+R\exp(\mathrm{i}k\mathscr{L})\,E\left(t-\frac{l}{c}, L\right) \tag{5.2.5a}$$

$$E_{\mathrm{T}}(t)=\sqrt{T}\,E(t, L)\exp(\mathrm{i}kL). \tag{5.2.5b}$$

Equations (5.2.4) and (5.2.5) are the bases of Ikeda's analysis. He defines the population difference in such a way that $w=\frac{1}{2}(-\frac{1}{2})$ for an atom in the upper (lower) energy state. The connection with Ikeda's work is therefore made easier by replacing W in (5.2.4) by $2W$, so that W below will actually be the same as Ikeda's. Defining $\theta=2\pi Nd^2k/\hbar$, $\Delta\omega=\Delta$, $\gamma_{\mathrm{T}}=\beta$, $\gamma_{\parallel}=\gamma$, and $\mu=d/\hbar$, we can write eqs. (5.2.4a) and (5.2.4b) as eqs. (4) and (5) of Ikeda's paper [109]:

$$E\left(\tau+\frac{z}{c}, z\right)=E(\tau, 0)\exp\left[2\theta W(\tau, z)\frac{\mathrm{i}\Delta\omega+\gamma_\perp}{\Delta\omega^2+\gamma_\perp^2}\right] \tag{5.2.6a}$$

$$\frac{\partial}{\partial\tau}W(\tau, z)=-\gamma_{\parallel}\left(W+\frac{z}{2}\right)-\frac{\mu^2}{2\theta}|E(\tau, 0)|^2\left\{\exp\left[\frac{4\theta\gamma_\perp W}{\Delta\omega^2+\gamma_\perp^2}\right]-1\right\}. \tag{5.2.6b}$$

We now define the dimensionless variables [109]

$$\begin{aligned}
&x=\gamma_{\parallel}t, \qquad \kappa=\gamma_{\parallel}\mathscr{L}/c, \qquad \Delta=\Delta\omega/\gamma_\perp\\
&\phi(t)=\frac{1}{L}W\left(t-\frac{\mathscr{L}}{c}, L\right)\\
&\varepsilon(t, z)=\frac{u}{2}E(t, z)\,[\gamma_\perp\gamma_{\parallel}(1+\Delta^2)]^{-1/2}\\
&\varepsilon_{\mathrm{T}}(t)=\frac{u}{2}E_{\mathrm{T}}\left(t-\frac{l}{c}\right)[\gamma_\perp\gamma_{\parallel}(1+\Delta^2)]^{-1/2}\\
&\varepsilon_{\mathrm{I}}(t)=\frac{u}{2}E_{\mathrm{I}}(t)\,[\gamma_\perp\gamma_{\parallel}(1+\Delta^2)]^{-1/2}
\end{aligned} \tag{5.2.7}$$

in terms of which (5.2.5) and (5.2.6) may be combined in the form of time-delay equations [109]:

$$\varepsilon(x,0) = \sqrt{T}\,\varepsilon_{\mathrm{I}}(x) + R\,\varepsilon(x-k,0)\exp\{\alpha L\,\phi(x)\}\exp\{\mathrm{i}[\alpha L\Delta(\phi(x)+\tfrac{1}{2}) - \delta_0]\} \tag{5.2.8a}$$

$$\frac{\mathrm{d}\phi}{\mathrm{d}x} = -(\phi(x)+\tfrac{1}{2}) - 2\,|\varepsilon(x-\kappa,0)|^2 \frac{1}{\alpha L}[\exp\{2\alpha L\,\phi(x)\} - 1] \tag{5.2.8b}$$

$$\varepsilon_{\mathrm{T}}(x) = \sqrt{T}\,\varepsilon(x-\kappa,0)\exp\{\alpha L\,\phi(x)\}\exp\{\mathrm{i}[\alpha L\Delta(\phi(x)+\tfrac{1}{2}) - (\delta_0 + kl)]\} \tag{5.2.8c}$$

where

$$\alpha = 2\theta\gamma_\perp/(\Delta\omega^2 + \gamma_\perp^2) \tag{5.2.9a}$$

$$\delta_0 = -k\left[\left(1 - \frac{2\pi N\mu^2\Delta\omega}{\Delta\omega^2+\gamma_\perp^2}\right)L + l\right] + 2\pi M \tag{5.2.9b}$$

and $2\pi M$ is introduced as the integral multiple of 2π closest to the first term on the right-hand side of (5.2.9b).

The steady-state limit of (5.2.8) is obtained by setting $\mathrm{d}\phi/\mathrm{d}x = 0$ and $\varepsilon(x,0) =$ constant. If $\delta_0 = \Delta = 0$, we obtain after simple algebra the steady-state relation

$$\log\left[1 + T\left(\frac{\varepsilon_{\mathrm{I}}}{\bar{\varepsilon}_{\mathrm{T}}} - 1\right)\right] + \frac{1}{2T}\bar{\varepsilon}_{\mathrm{T}}^2\left\{\left[1 + T\left(\frac{\varepsilon_{\mathrm{I}}}{\bar{\varepsilon}_{\mathrm{T}}} - 1\right)\right]^2 - 1\right\} = \tfrac{1}{2}aL \tag{5.2.10}$$

where $\bar{\varepsilon}_{\mathrm{T}}$ denotes the steady-state value of ε_{T}. This is the relation for "absorptive" optical bistability obtained by Bonifacio and Lugiato [110]. They show that, for R greater than some critical value depending on L, there are two allowed values of $\bar{\varepsilon}_{\mathrm{T}}$ for the same value of ε_{I}, i.e., there is optical bistability. (This is called "absorptive" bistability because $\Delta = 0$ implies there is no resonant dispersion.) If αL, $\alpha\Delta L$, $|\delta_0|$ and $|\bar{\varepsilon}_{\mathrm{T}}|^2/T$ are all small compared with unity, we have the case of "dispersive" bistability observed in experiments of Gibbs et al. [111].

For a detailed review of optical bistability, and an extensive bibliography, the reader is again referred to Abraham and Smith [106]. Henceforth we will focus our attention primarily on *chaos* in optical bistability.

If the population difference has a relaxation time much shorter than the ring transit time $\mathscr{L}/c$, so that $\kappa \gg 1$, we may set $\mathrm{d}\phi/\mathrm{d}x \cong 0$ in (5.2.8b), and the time-delay equations in this limit reduce to a discrete mapping:

$$\varepsilon_{0,n} = \sqrt{T}\,\varepsilon_{\mathrm{I}} + R\,\varepsilon_{0,n-1}\exp(\alpha L\phi_n)\exp\{\mathrm{i}[\alpha L\Delta(\phi_n + \tfrac{1}{2}) - \delta_0]\} \tag{5.2.11a}$$

$$\varepsilon_{\mathrm{T},n} = \sqrt{T}\,\varepsilon_{0,n-1}\exp(\alpha L\phi_n)\exp\{\mathrm{i}[\alpha L\Delta(\phi_n + \tfrac{1}{2}) - (\delta_0 + kl)]\} \tag{5.2.11b}$$

$$\phi_n + \tfrac{1}{2} = \frac{2}{\alpha L}|\varepsilon_{0,n-1}|^2(1 - \exp(\alpha L\phi_n)) \tag{5.2.11c}$$

where

$$\varepsilon_{0,n} \equiv \varepsilon(x_0 + n\kappa, 0) \tag{5.2.12a}$$

$$\varepsilon_{T,n} \equiv \varepsilon_T(x + n\kappa)\,. \tag{5.2.12b}$$

Ikeda [109] iterated the mapping (5.2.11) for the example $\alpha\Delta L = 6$, $\alpha L = 4$, $\delta_0 = 0$ and $R = 0.95$. Within a range of values of $|\varepsilon_I|$, the sequence $\{\varepsilon_{T,n}\}$ of transmitted field strengths is chaotic, and follows a period-doubling route to chaos. This possibility of chaos in optical bistability sparked a lively interest in "optical turbulence".

Consider now a medium of TLAs far removed from resonance with the input field. If the absorption coefficient of the medium is nonsaturable and the TLAs, being far from resonance, make no significant contribution to it, then in (5.2.8) we may replace $\alpha L\phi$ by $\alpha L(-\frac{1}{2})$. Defining e and θ by

$$\varepsilon(x, 0) = [2\Delta(1 - e^{-\alpha L})]^{-1/2}\, e(x) \tag{5.2.13a}$$

$$\phi(x) + \tfrac{1}{2} = (1/\alpha\Delta L)\,\theta(x) \tag{5.2.13b}$$

we then obtain from (5.2.8) the time-delay system

$$e(t) = A + B\, e(t - t_R) \exp\{i[\theta(t) - \delta_0]\} \tag{5.2.14a}$$

$$\frac{1}{\gamma_\parallel}\dot{\theta}(t) = -\theta(t) + |e(t - t_R)|^2 \tag{5.2.14b}$$

where

$$A \equiv [2T\Delta(1 - e^{-\alpha L})]^{1/2}\varepsilon_I \tag{5.2.15a}$$

$$B \equiv R\, e^{-\alpha L/2} \tag{5.2.15b}$$

$$t_R \equiv \mathscr{L}/c\,. \tag{5.2.15c}$$

Equations (5.2.14) for the case of "dispersive" optical bistability are identical to those of Ikeda et al. [112] for the case in which the cell contains a medium with a nonlinear refractive index. In their case the longitudinal relaxation rate $\gamma_\parallel$ of the optical Bloch equations is replaced by the relaxation rate used in the Debye theory of dielectric relaxation, and A is defined differently. They show that the equations (5.2.14) admit chaotic behavior, and Nakatsuka et al. [113] have observed this optical turbulence experimentally, as discussed below.

When the cavity circuit time is much larger than the material relaxation time (i.e., $\gamma_\parallel t_R \gg 1$), we may use an adiabatic approximation to $\theta(t)$, setting the left-hand side of (5.2.14b) to zero so that $\theta(t) \cong |e(t - t_R)|^2$. Then from (5.2.14a) we obtain

$$e(t) = A + B\, e(t - t_R) \exp\{i[|e(t - t_R)|^2 - \delta_0]\}\,. \tag{5.2.16}$$

In this approximation, therefore, the differential-difference system (5.2.14) is replaced by the discrete mapping

$$e_n = A + Be_{n-1}\exp\{i[|e_{n-1}|^2 - \delta_0]\} \tag{5.2.17}$$

studied by Ikeda et al. [112]. This takes the form of a real two-dimensional mapping that has a period-doubling route to chaos. The results of a detailed study of this map have been reported by Carmichael et al. [114].

The fixed points $\bar{e}$ of the map (5.2.17) may be found numerically. In particular, the amplitudes $|\bar{e}|$ are determined by the equation

$$A = |\bar{e}|\,[1 + B^2 - 2B\cos(|\bar{e}|^2 - \delta_0)]^{1/2} \tag{5.2.18}$$

assuming for simplicity that A is real. Figure 5.2 shows $|\bar{e}|$ as a function of A for $\delta_0 = 0$ and $B = 0.5$, and also indicates which branches of the solution are stable. Proceeding along the lower stable branch from $A = 0$, stability is lost at $A \cong 1.24775$, and a period-doubling bifurcation occurs. At $A = 1.5$, for instance, the iteration of (5.2.17) starting from $e_0 = 0$ yields $|e_n| = 1.807953$, 0.6226517, 1.807953, 0.6226517,... after initial transients die out. At $A \cong 1.511525$ a 4-cycle is found, and very small increases in A lead to more period doublings and chaos. Carmichael et al. [114] have verified that the rate of period doubling to chaos is governed by the Feigenbaum number δ.

Figure 5.3 shows the chaotic attractor in the complex e plane as computed by Ikeda et al. [112] for the case $B = 0.4$, $A = 4.39$. The enlargement shown in fig. 5.3b shows a structure within structure, as in the case of the chaotic Hénon attractor (fig. 2.3). In fig. 5.4 we show the Ikeda attractor for the case $B = 0.5$, $A = 1.565$. The attractor in this case also shows the characteristic ribbonlike aspect of a strange attractor under enlargement.

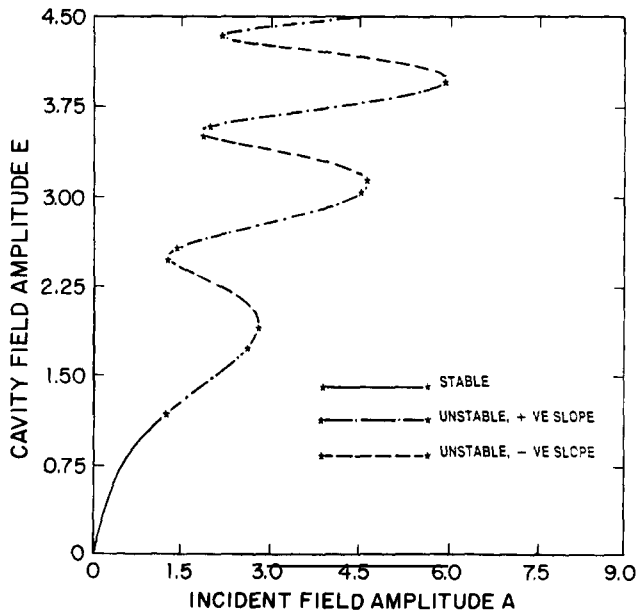

Fig. 5.2. $|\bar{e}|$ as a function of A for $\delta_0 = 0$ and $B = 0.5$, indicating which branches of the solution are stable. (Courtesy of H.J. Carmichael.)

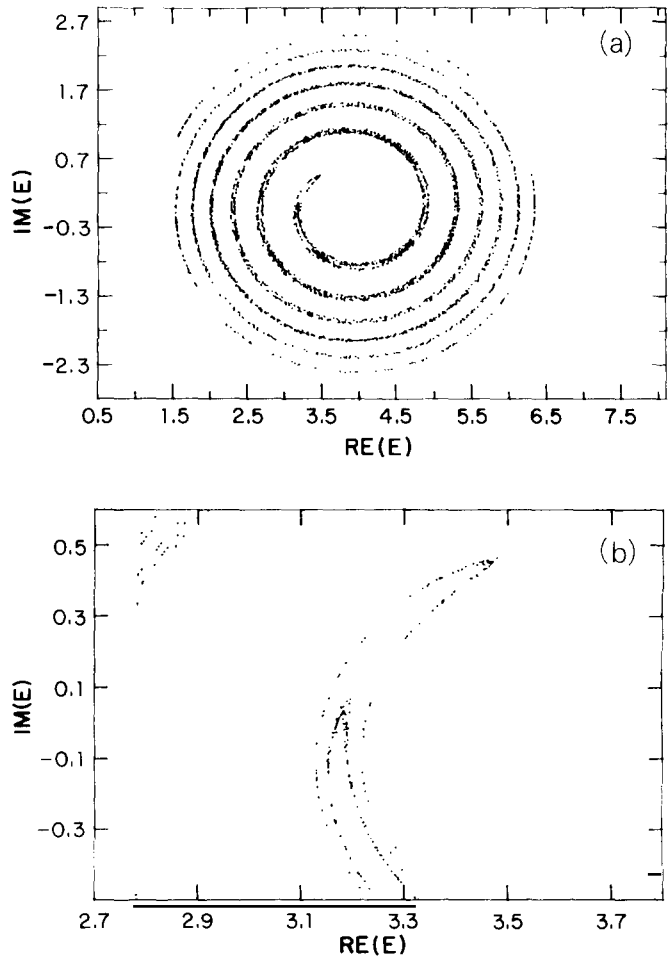

Fig. 5.3. Chaotic Ikeda attractor in the complex e plane for $B = 0.4$ and $A = 4.39$ (a), and an enlargement (b) showing structure within structure.

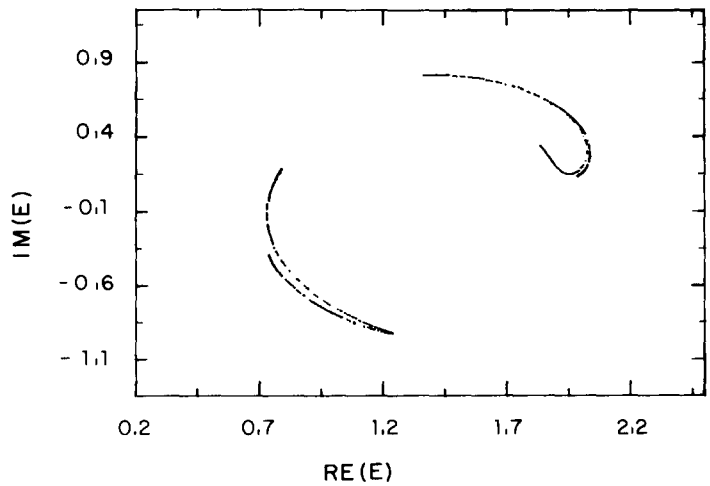

Fig. 5.4. Ikeda attractor for $B = 0.5$, $A = 1.565$. (Courtesy of A. Zardecki.)

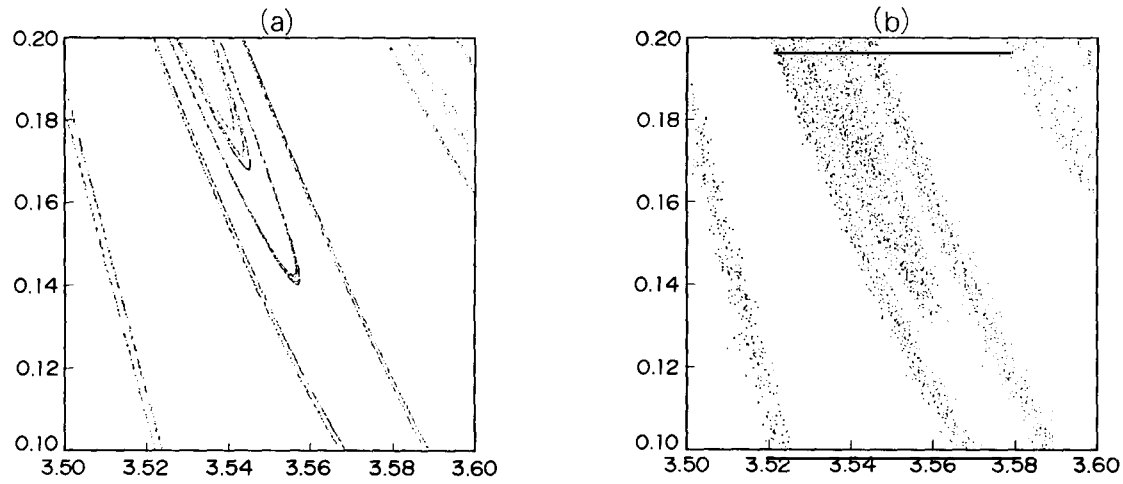

Fig. 5.5. A section of the Ikeda attractor for $B = 0.8$, $A = 3.0$, without noise (a), and with Gaussian noise (b) having $q = 0.001$. (Courtesy of A. Zardecki.)

It is interesting to consider the influence of noise on a chaotic dynamical system. Zardecki [115] has considered the effect on the Ikeda attractor of Gaussian noise superimposed on the incident driving field. The added noise term is $q[\xi_n + i\eta_n]$, where q is a small real number and ξ_n, η_n are independent Gaussian random variables of zero mean and unit variance. Figure 5.5a shows a section of the Ikeda attractor for $B = 0.8$, $A = 3.0$ without noise ($q = 0$), and fig. 5.5b shows the same section for $q = 0.001$. It is evident that one effect of noise is to change the fractal dimension d (eq. (2.3.13)) of the attractor. Figure 5.6 shows $d(\varepsilon) = \log N(\varepsilon)/\log(\varepsilon^{-1})$ computed by Zardecki for both the Ikeda and Hénon maps, with and without noise. On a very fine scale of resolution (ε small), below the magnitude of the noise, $d(\varepsilon)$ is close to 2.0, which is in fact the fractal dimension of two-dimensional Gaussian noise. That is, at high resolution $d(\varepsilon)$ is a measure of the noise and not the dynamical system. For coarse resolution $d(\varepsilon)$ approximates the fractal dimension of the attractor in the absence of noise, i.e., 1.26 and 1.41, respectively, for the Hénon and Ikeda maps.

Ikeda et al. [112] argue that, with increasing t, eq. (5.2.17) eventually becomes inapplicable, even if the condition $\gamma_{\parallel} t_R \gg 1$ is satisfied. This is a consequence of very sensitive dependence on initial conditions. For if $e(t)$ has any variations, small differences between $e(t_1)$ and $e(t_2)$ $(0 \leq t_1 \neq t_2 < t_R)$ become magnified, and their images under the mapping (5.2.17) eventually have a very short "correlation time". When this time becomes as small as the material relaxation time, we can no longer make an adiabatic elimination of $\theta(t)$.

If $B \ll 1$ but $A^2 B \sim 1$, we can write the following approximate version of (5.2.14):

$$\frac{1}{\gamma_{\parallel}} \dot{\theta}(t) = -\theta(t) + A^2\{1 + 2B \cos[\theta(t - t_R) - \delta_0]\}. \tag{5.2.19}$$

(Note that this time-delay differential equation is effectively equivalent to an autonomous system of infinite order. The Poincaré–Bendixson theorem does not apply.) By numerically integrating (5.2.19), and Fourier transforming the time series so obtained, Ikeda et al. [112] find a transition to chaos as A is varied: The power spectrum of $\theta(t)$ changes from a series of sharp spikes to a broad-band spectrum.

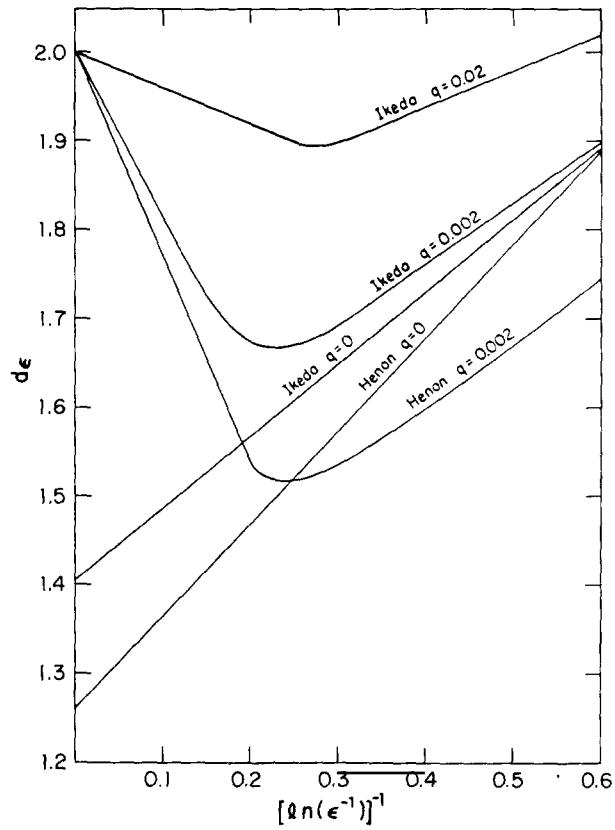

Fig. 5.6. Approximate fractal dimension $d(\varepsilon)$ vs. $[\log(\varepsilon^{-1})]^{-1}$ computed by Zardecki for the Ikeda and Hénon maps, with and without noise. (Courtesy of A. Zardecki.)

The experiments of Nakatsuka et al. [113] on chaos in an "all-optical" bistable system support this prediction. Their experimental arrangement is indicated in fig. 5.7. A single-mode optical fiber, having a quadratic nonlinear index, is used as the nonlinear "cell" in the ring cavity. The high power level necessary for the observation of chaos with this system was obtained from the second harmonic of a

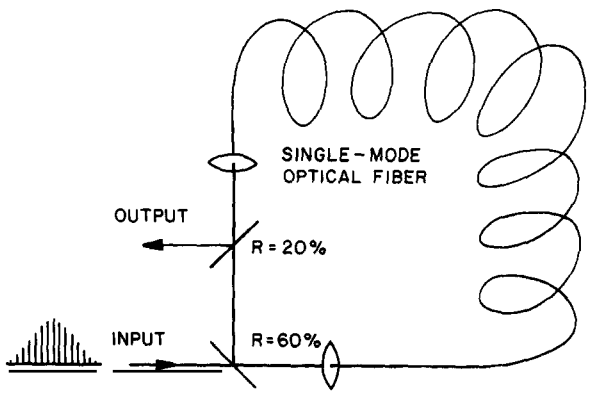

Fig. 5.7. Schematic of experimental arrangement of Nakatsuka et al. [113]. (Courtesy of H. Nakatsuka.)

mode-locked YAG laser (pulse separation ~7.6 ns). As the bifurcations to chaos stem from the interference of the input and cavity fields, it was necessary to match the ring transit time to the period of the mode-locked pulses. The cavity was such that $B \cong 0.4$–0.5, and the parameter A could be increased sufficiently, by raising the input power level, to realize a chaotic regime of the system. When the peak power of the input pulse train was raised from 50 to 160 W, a period doubling of the output train was observed. At a power level of 300 W the output was chaotic. The results were consistent with the theoretical model.

Chaos in a "hybrid" optically bistable device, in which a delay time is introduced electronically using a delayed feedback line, was observed in 1980 by Gibbs et al. [116]. Their hybrid device is well described by eq. (5.2.19) of Ikeda et al. [112], although of course the origin of the delay time τ_R is different.

Chaos in an all-optical ring-resonator system employing an ammonia cell and injected CO_2 laser pulses has been reported by Harrison et al. [117]. As in the experiments of Gibbs et al. there is evidence of a period-doubling route to chaos. Their approach offers considerable flexibility for the variation of parameters, and furthermore enjoys the theoretical neatness associated with a homogeneously broadened two-level system.

The development of chaos in a ring resonator pumped by a sequence of sech pulses has been studied numerically by Blow and Doran [118]. Their analysis is based on a nonlinear, Schrödinger-like wave equation, in which the dispersive nonlinearity is due to the Kerr effect. Chaos via period doubling was observed with increasing pump intensity, followed by an inverse Feigenbaum sequence. In contrast to the dispersionless case [113], all points of the pulse circulating in the cavity seem to have the same dynamics for their choice of parameters.

5.3. Chaos in optical mixing

It is also possible for chaos to appear in the propagation of intense laser radiation in a nonlinear optical medium. We will consider an example involving coupled wave equations for the pump, Stokes and anti-Stokes modes in Raman scattering [119].

Let A_1, A_2 and A_3 be the electric field amplitudes for the anti-Stokes, pump and Stokes modes, respectively, and assume perfect phase matching. We write [120, 121]

$$\dot{A}_1 = -\gamma_1 A_1 - \beta_1[|A_2|^2 A_1 + A_2^2 A_3^*] \tag{5.3.1a}$$

$$\dot{A}_2 = -\gamma_2 A_2 + \beta_2[|A_1|^2 - |A_3|^2] A_2 \tag{5.3.1b}$$

$$\dot{A}_3 = -\gamma_3 A_3 + \beta_3[|A_2|^2 A_3 + A_1^* A_2^2]\,. \tag{5.3.1c}$$

The γ_i are loss or gain coefficients, and the β_i are mode-coupling coefficients involving Raman cross sections [120]. Introduce real variables a_i and θ_i by writing

$$A_i = a_i(z) \exp\{\mathrm{i}\, \theta_i(z)\} \tag{5.3.2}$$

and assume for simplicity that $2\theta_2 - \theta_3 - \theta_1 = 0$ at the input plane $z = 0$. Then (5.3.1) takes the form of a third-order autonomous system:

$$\dot{a}_1 = -\gamma_1 a_1 - \beta_1(a_1 + a_3)a_2^2 \tag{5.3.3a}$$

$$\dot{a}_2 = -\gamma_2 a_2 + \beta_2(a_1^2 - a_3^2)a_2 \tag{5.3.3b}$$

$$\dot{a}_3 = -\gamma_3 a_3 + \beta_3(a_1 + a_3)a_2^2 . \tag{5.3.3c}$$

We will focus our attention on the parameter values $\gamma_1 = -1$, $\gamma_2 = \gamma_3 = -\gamma$, $\beta_1 = 9, \beta_2 = 5, \beta_3 = 1$.

Consider first the case $\gamma = -1$. There are five fixed points of (5.3.3), and in this case they are all unstable. Figure 5.8 shows $a_2(z)$ for the initial condition $a_1(0) = a_2(0) = a_3(0) = 1$. The evolution of a_2 *looks* chaotic, and this is confirmed by taking the Fourier transform of a_2, for instance, as shown in fig. 5.9. In fig. 5.10 we plot $a_2(z)$ vs. $a_1(z)$. The orbit winds around one fixed point and then another, and

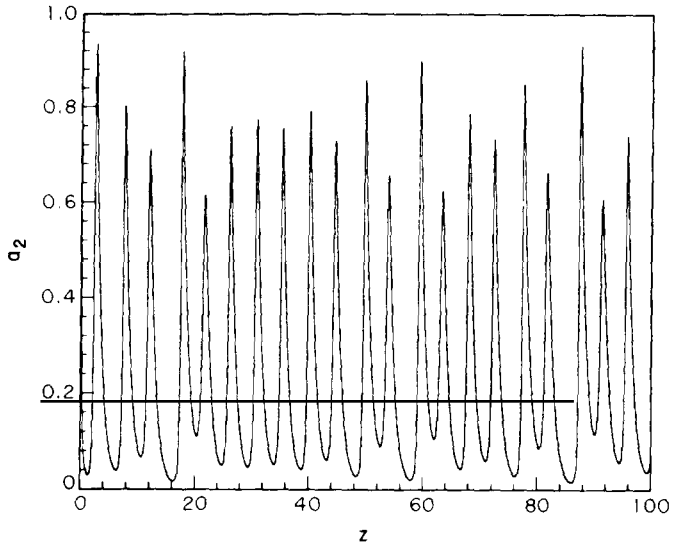

Fig. 5.8. Variation of pump amplitude a_2 with z for $\gamma_1 = -1$, $\gamma_2 = \gamma_3 = 1$, $\beta_1 = 9$, $\beta_2 = 5$, $\beta_3 = 1$.

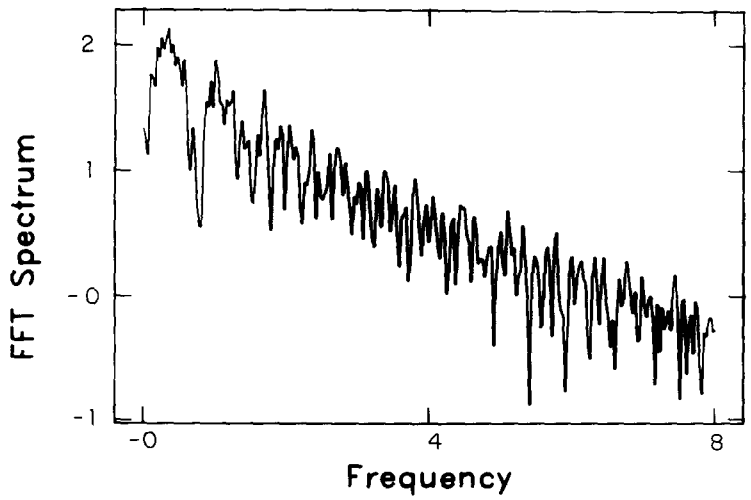

Fig. 5.9. Power spectrum of a_2 of fig. 5.8.

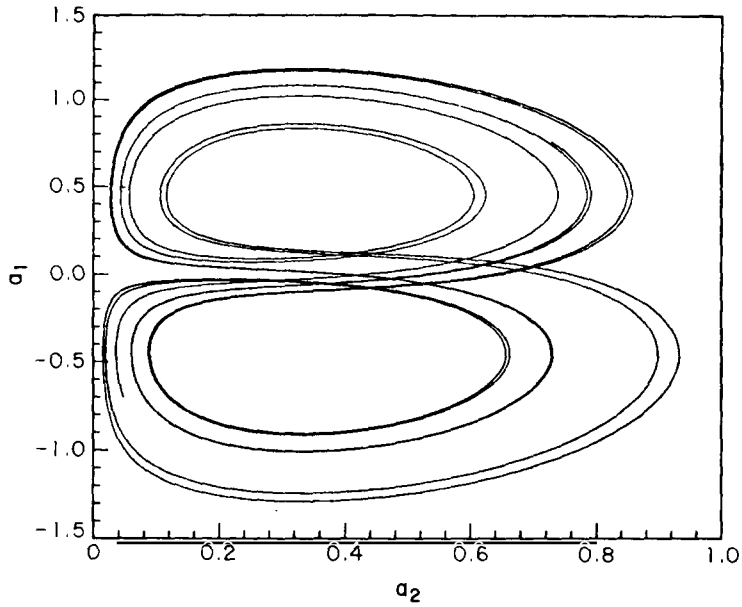

Fig. 5.10. a_1 vs. a_2 for the parameters of fig. 5.8, $40 \leq z \leq 100$.

when one looks at its development in time (or actually z) it appears to switch erratically between the two. A similar result is found when $a_3(z)$ is plotted vs. $a_2(z)$ (fig. 5.11). These results are reminiscent of the Lorenz model, and in fact (5.3.3) has an important property in common with the Lorenz model: It is invariant under the transformation $(a_1, a_2, a_3) \rightarrow (-a_1, a_2, -a_3)$, the a_2 axis is invariant, and any point on the a_2 axis approaches the origin.

Let us now consider a Poincaré map using the surface of section $a_1 = 0$ (see fig. 2.5). The points on the Poincaré map shown in fig. 5.12 for $\gamma = 1$ appear in the $a_2 a_3$ plane in an apparently random fashion. We also show in fig. 5.13 a magnified section of fig. 5.12. When this section is further enlarged we can begin to see structure within structure, or self-similarity, suggesting that the Poincaré map has a Cantor-like structure associated with strange attractors.

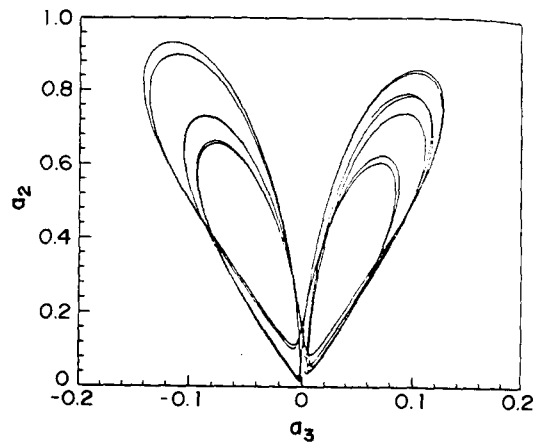

Fig. 5.11. a_2 vs. a_3 for the parameter values of fig. 5.8, $40 \leq z \leq 100$.

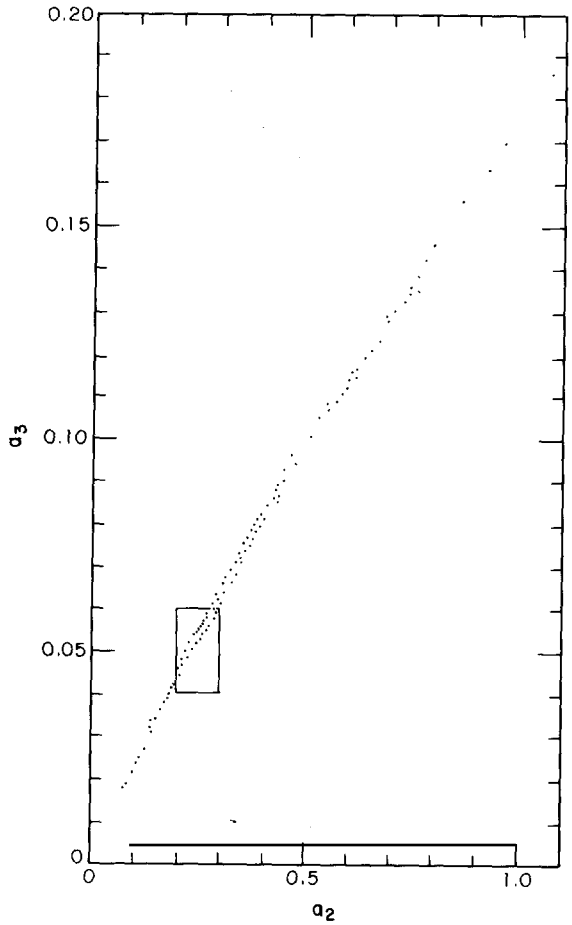

Fig. 5.12. Poincaré map obtained by plotting $a_3(z)$ vs. $a_2(z)$ for points z at which $a_1 = 0$ and $\dot{a}_1 < 0$.

Sensitivity to initial conditions for this chaotic Raman attractor may be verified by computing the Lyapunov characteristic exponents of the system. We have "very sensitive dependence on initial conditions" (chaos) if any of the Lyapunov exponents is positive, and so it suffices, in order simply to verify that the system is chaotic, to compute the largest exponent. This may be done as described in section 2.4. The result of the computation for the chaotic Raman attractor with $\gamma = 1$ is shown in fig. 5.14. χ converges to about 0.1, verifying that the attractor is chaotic.

If we reduce γ to 0.05, we obtain for $a_2(z)$ the result shown in fig. 5.15. The system reaches a stable limit cycle, as confirmed both by spectral analysis and Poincaré maps. In fig. 5.16 we show $a_1(z)$ vs. $a_2(z)$ for this case of orderly behavior. The orbit in the a_1a_2 plane simply keeps retracing its path over the figure eight.

This example of order and chaos in a nonlinear optical problem will be difficult to study experimentally, as it assumes gain at the anti-Stokes frequency but loss at the Stokes and pump frequencies. Nevertheless it suggests that chaos may be found in other nonlinear optical phenomena of this type. For instance, Ray [122] has suggested that chaotic behavior described by the Lorenz model may be found in three-wave optical mixing. It should also be mentioned that Randall and Albritton [123] have studied

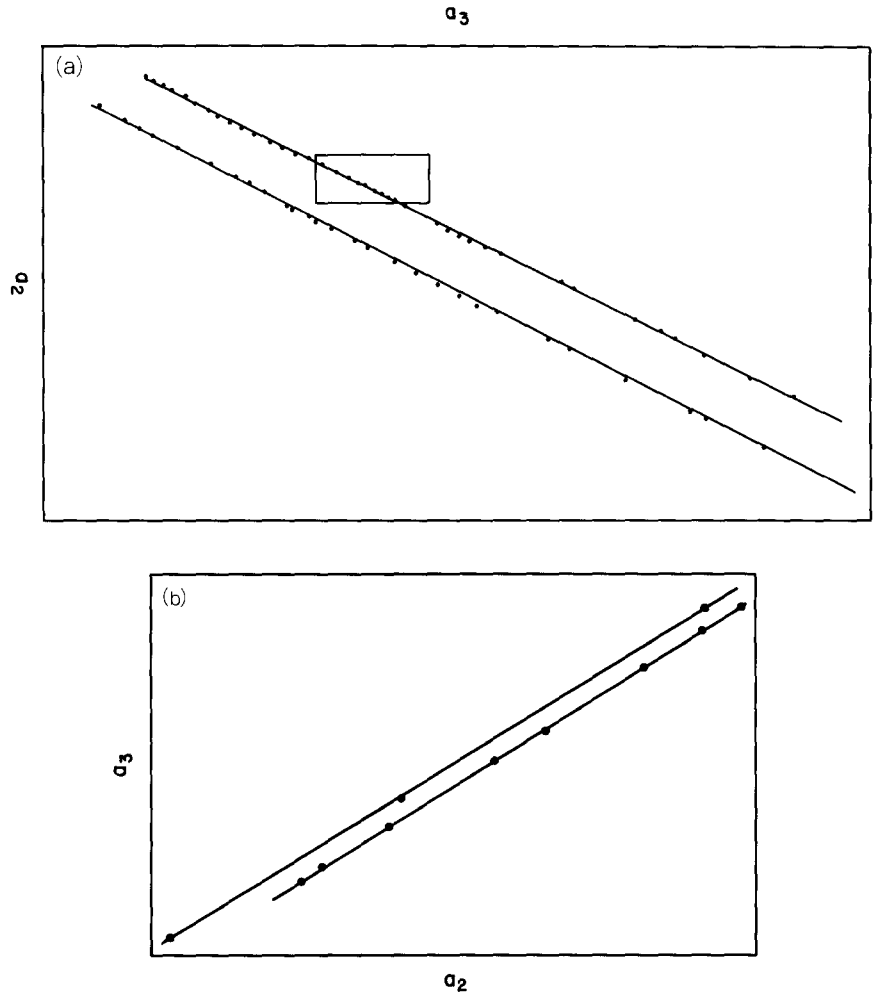

Fig. 5.13. (a) Magnification of the rectangle indicated in fig. 5.12 and (b) magnification of the rectangle in (a).

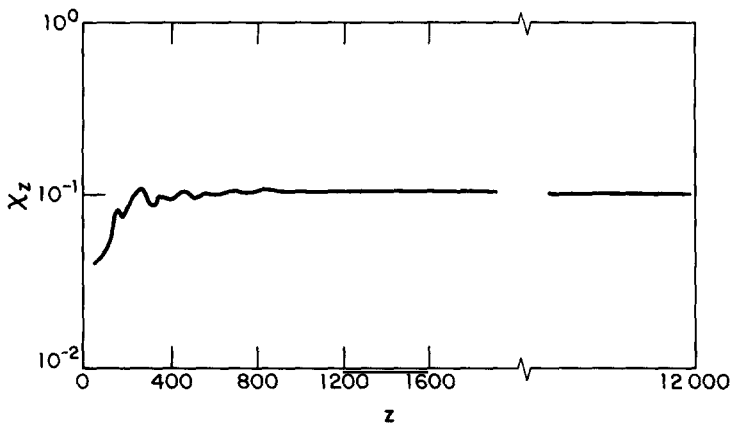

Fig. 5.14. Maximal Lyapunov exponent computed for the parameters of fig. 5.8.

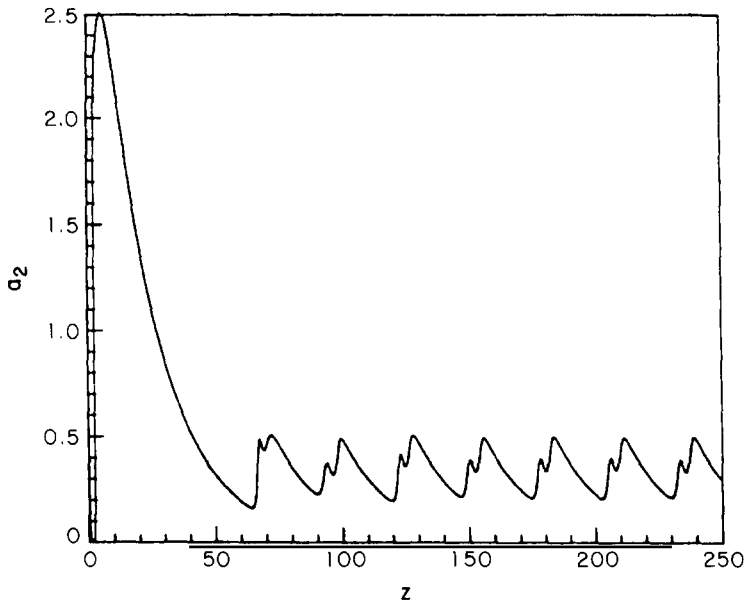

Fig. 5.15. Variation of pump amplitude a_1 with z for $\gamma_1 = -1$, $\gamma_2 = \gamma_3 = 0.05$, $\beta_1 = 9$, $\beta_2 = 5$, $\beta_3 = 1$.

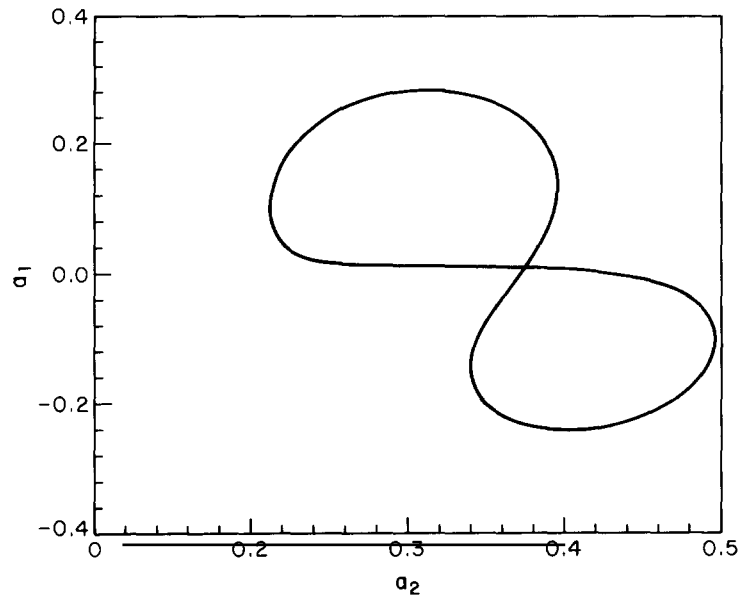

Fig. 5.16. a_1 vs. a_2 for the parameters of fig. 5.8.

partial differential equations modeling nonlinear stimulated Brillouin scattering in a medium with a reflecting boundary. The boundary leads to results qualitatively different from the predictions of the usual steady-state coupled wave equations, including the generation of subharmonics of the acoustic wave frequency. The scattered light intensity may also have chaotic time evolution.

6. Chaos in infrared laser–molecule interactions

6.1. Introduction

A vibrational mode of a molecule pumped by a laser is basically an example of a sinusoidally driven anharmonic oscillator. The possibility therefore arises that the dynamics of this nonlinear oscillator could be chaotic for a certain range of parameter values. In fact the Duffing oscillator considered in section 2.5 serves as a crude model of a driven molecular oscillator. In this section we will consider more realistic models, taking into account "background" vibrational modes coupled to the infrared-active pumped mode. We will see that for realistic parameter values the pumped-mode dynamics is indeed predicted to be chaotic [124]. Furthermore this chaos may explain very nicely a general trend observed experimentally in the multiple photon excitation of a large number of molecules, namely that the absorption tends to be fluence dependent rather than intensity dependent. We will also describe a model that includes molecular rotations but not the intermode coupling, and again predict that the molecule undergoes chaotic motion under the influence of the laser [125].

6.2. The model Hamiltonian

The energy-level spacings for electronic, vibrational and rotational transitions differ by orders of magnitude, and it is reasonable therefore to assume the separability of these motions. The Born–Oppenheimer approximation [126] is just the assumption that electronic structure may be separated from the vibrational-rotational structure of a molecule. Since we are interested here in infrared laser–molecule interactions, we will ignore the electronic structure of the molecules.

Consider first a diatomic molecule, as illustrated in fig. 6.1. The Hamiltonian describing the interaction of such a molecule with an applied (infrared) field is simply

$$H = \Delta a_z^\dagger a_z + B_0(J_x^2 + J_y^2) + \Omega \hat{e}_Z \mathbb{C}_{Zz}(a_z^\dagger + a_z) \tag{6.2.1}$$

where the first and second terms represent the vibrational and rotational energies, respectively, and the last term describes the coupling of the vibration to the applied field. The operators a_z and $a_z^\dagger$ are the annihilation and creation operators for the vibrational motion along the z axis of the molecule; Δ is the frequency detuning between the laser and the molecular vibration. J_x and J_y are the angular momentum operators for the two rotational degrees of freedom, the constant B_0 being inversely proportional to the moment of inertia. Ω is the Rabi frequency, and $\mathbb{C}_{Zz}$ is the direction cosine diadic taking the field along the Z axis in the laboratory frame into the molecular dipole moment along the z axis in the molecular frame; $\hat{e}_Z$ is the unit vector giving the orientation of the applied electric field.

The anharmonicity of the molecular vibration may be accounted for by adding a term $-\chi(a_z^\dagger a_z)^2$ to the Hamiltonian (6.2.1), where χ is the "anharmonicity" constant. This correction perturbs the energy of vibrational level n by $-\chi n^2$. It may be regarded as the rotating-wave approximation to the standard $q^4 = (a + a^\dagger)^4$ anharmonic correction. With this addition the Hamiltonian (6.2.1) applies not only to a diatomic molecule, but also to a nondegenerate pumped mode of a *polyatomic* molecule. That is, it contains the essential physics of the laser–molecule interaction.

Consider now the specific example of the SF_6 molecule. The two infrared active normal modes of vibration in this case, denoted ν_3 and ν_4, are separated by roughly 300 cm^{-1}. This means that a laser can interact selectivity with one specified mode, and since the ν_3 mode vibrates in the 10 μm region it has

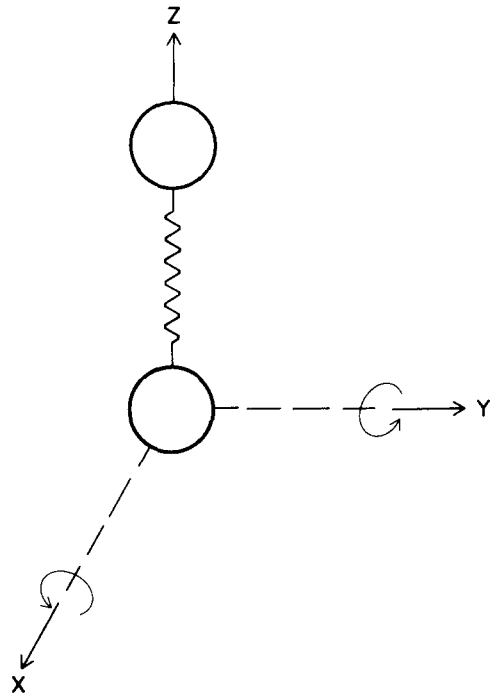

Fig. 6.1. A diatomic molecule having rotational degrees of freedom along the x and y axes.

been studied extensively using the CO_2 laser [127]. The ν_3 mode is somewhat complicated by the fact that it is triply degenerate, and this brings some additional features into the Hamiltonian. Furthermore, we should include non-laser-coupled "background" modes in the Hamiltonian, because they are coupled to the laser-pumped ν_3 mode and can exchange energy with it. For our generic Hamiltonian describing infrared absorption in a polyatomic molecule we therefore write

$$H = H_{\mathrm{PM}} + H_{\mathrm{BM}} + H_{\mathrm{IC}} + H_{\mathrm{R}} + H_{\mathrm{PMF}} \tag{6.2.2}$$

where

$$H_{\mathrm{PM}} = \Delta \boldsymbol{a}^\dagger \cdot \boldsymbol{a} - \chi(\boldsymbol{a}^\dagger \cdot \boldsymbol{a})^2 + G(\boldsymbol{a}^\dagger \times \boldsymbol{a})^2 + T \sum_i (a_i^\dagger a_i)^2 \tag{6.2.3a}$$

$$H_{\mathrm{BM}} = \sum_m (\Delta + \varepsilon_m)\, \boldsymbol{b}_m^\dagger \cdot \boldsymbol{b}_m + \sum_m \chi_{mm} (\boldsymbol{b}_m^\dagger \cdot \boldsymbol{b}_m)^2 \tag{6.2.3b}$$

$$H_{\mathrm{IC}} = \sum_m \beta_m (\boldsymbol{a}^\dagger \cdot \boldsymbol{b}_m + \boldsymbol{b}_m^\dagger \cdot \boldsymbol{a}) + \sum_n \sum_{m \neq n} \chi_{mn} (\boldsymbol{b}_n \cdot \boldsymbol{b}_m^\dagger)(\boldsymbol{b}_m \cdot \boldsymbol{b}_n^\dagger) \tag{6.2.3c}$$

$$H_{\mathrm{R}} = B_0 \boldsymbol{J}^2 \tag{6.2.3d}$$

$$H_{\mathrm{PMF}} = \Omega \hat{\boldsymbol{\varepsilon}} \cdot \overleftrightarrow{\mathbb{C}} \cdot (\boldsymbol{a}^\dagger + \boldsymbol{a}) \tag{6.2.3e}$$

where we have indicated explicitly the vector character of the various operators. H_{PM} is the Hamiltonian operator for the pump mode; it contains terms representing its anharmonic character (χ), its vibrational angular momentum (G), and its vibrational tensor splitting (T). The latter two terms are attributable to the degeneracy of the pump mode, and for this reason were not present in (6.2.1). The anharmonicity term, another consideration in a realistic model, reflects the presence of a continuum at high excitation energy (i.e., a real molecule can be dissociated!). The Hamiltonian H_{BM} for the background modes is similar to H_{PM}, but we neglect the G and T terms for simplicity. H_{IC} represents the intramolecular mode coupling among all the modes; the first term is the coupling between the pump mode and the background modes, the second is a mixing among the background modes. H_R is the (rigid-rotator) Hamiltonian for molecular rotation, and finally H_{PMF} is the laser-pump-mode interaction. The laser field is treated as an externally prescribed, classical field.

In the following sections we will consider model problems based on simplifications of (6.2.2). The most significant aspect of these models, which we believe are fairly realistic, is that *chaotic behavior is predicted.* In other words, we believe that chaos is fundamental to the process of infrared multiple-photon absorption. Furthermore the appearance of chaos has interesting experimental consequences, as we will see.

6.3. A basic model of multiple photon excitation

We will now describe a simplified model based on the Hamiltonian (6.2.2). First of all let us neglect entirely the rotation of the molecule. We will take $G = T = 0$ and assume that the background modes are perfectly harmonic, so that $\chi_{mm} = 0$ in (6.2.3b). We furthermore ignore any coupling among background modes, setting $\chi_{mn} = 0$ in (6.2.3c). Thus we replace (6.2.2) by

$$H = H_{PM} + H_{BM} + H_{IC} + H_{PMF} \tag{6.3.1}$$

where

$$H_{PM} = \Delta a^\dagger a - \chi (a^\dagger a)^2 \tag{6.3.2a}$$

$$H_{BM} = \sum_m (\Delta + \varepsilon_m) b_m^\dagger b_m \tag{6.3.2b}$$

$$H_{IC} = \sum_m \beta_m (a^\dagger b_m + b_m^\dagger a) \tag{6.3.2c}$$

$$H_{PMF} = \frac{\Omega}{\sqrt{n}} (c^\dagger a + a^\dagger c) \tag{6.3.2d}$$

where c, $c^\dagger$ are the annihilation and creation operators for the quantized laser field mode. As indicated earlier, we will treat the applied field classically in the end. It is nevertheless useful to introduce c and $c^\dagger$ at this stage because we can easily identify the constant of the motion

$$a^\dagger a + \sum_m b_m^\dagger b_m + c^\dagger c = \text{total excitation number} \tag{6.3.3}$$

from the Heisenberg equations. This constant of the motion is a consequence of the rotating-wave approximation.

Without much loss of generality we will assume the coupling parameters β_m are all the same: $\beta_m = \beta$. As in radiationless transition theory it is also convenient to assume that the background oscillator frequencies are uniformly distributed [128]:

$$\varepsilon_m = \bar{\Delta}_0 + m\rho^{-1} \tag{6.3.4}$$

where $\bar{\Delta}_0$ is the separation between the band origins of the nearest background oscillator and the pump mode, and ρ is the density of background states. Such a "quasi-continuum" (QC) model in fact has roots in the Weisskopf–Wigner theory of radiative decay [129]. Related QC models have recently been considered in the context of laser–molecule interactions by Eberly et al. [130, 131] and Galbraith et al. [132]. The present model permits considerable analytical simplification via the Poisson summation formula [133].

In SF_6 the nearest background mode to the pump mode ν_3 is $\nu_2 + \nu_6$, and the anharmonicity of this mode is less than that of ν_3. This provides some justification for the simplification of treating the background as harmonic. The simplification of an infinite number of background oscillators is also more reasonable than might at first be supposed. The work of Bixon and Jortner [128], for instance, shows that the strength of the coupling of the pump mode with the background, when diagonalization is performed, is a Lorentzian function; for small coupling constant β, which we anticipate for a real molecule, the number of background oscillators can then be safely extended to infinity, because beyond a certain number there is essentially no contribution. This point is also discussed from a different point of view in ref. [133].

A final approximation, which makes the model more tractable, is to treat not only the field but the *entire* dynamics classically. Thus, for instance, a, $a^\dagger \to a$, a^*, ordinary c-numbers. Multiple photon excitation typically involves the absorption, in many molecules, of ~30 photons. We feel that quantum effects correlate to just a few photons absorbed, whereas we are interested in gross features of the absorption process. Other workers have also argued in favor of classical dynamics in the theory of infrared multiple photon absorption [134–136].

6.4. A discrete mapping

The equations of motion obtained from the Hamiltonian (6.3.1) are

$$\dot{a} = -i\Delta a + 2i\chi a|a|^2 - i\Omega - i\beta \sum_m b_m \tag{6.4.1a}$$

$$\dot{b}_m = -i(\Delta + \bar{\Delta}_0 + m\rho^{-1})b_m - i\beta a \tag{6.4.1b}$$

$$\dot{c} = \frac{-i\Omega}{\sqrt{n}} a . \tag{6.4.1c}$$

We assume that at $t = 0$ there are n photons in the laser field. The formal solution of (6.4.1c) is

$$c(t) = \sqrt{n} - \frac{i\Omega}{\sqrt{n}} \int_0^t dt'\, a(t') \tag{6.4.2}$$

and therefore

$$|c(t)|^2 \cong n + 2\Omega \int_0^t dt'\, \mathrm{Im}[a(t')] \tag{6.4.3}$$

for $n \gg 1$. In other words,

$$n - |c(t)|^2 = -2\Omega \int_0^t dt'\, \mathrm{Im}[a(t')] \tag{6.4.4}$$

represents the number of "photons" absorbed from the applied field.

From (6.4.1b) we have the formal solution

$$b_m(t) = -i\beta \int_0^t dt'\, a(t') \exp\{-i(\Delta + \bar{\Delta}_0 + m\rho^{-1})(t - t')\} \tag{6.4.5}$$

where all the background modes are assumed to be in their ground states at the initial time $t = 0$. Now in (6.4.1a) we need the sum

$$\sum_m b_m(t) = -i\beta \int_0^t dt'\, a(t') \exp\{-i(\Delta + \bar{\Delta}_0)(t - t')\} \sum_m \exp\{-im\rho^{-1}(t - t')\}\,. \tag{6.4.6}$$

The assumption that the background modes are uniformly spaced above and below the pump mode frequency allows us to invoke the Poisson sum rule:

$$\sum_{m=-\infty}^{\infty} \exp\{-im\rho^{-1}(t - t')\} = 2\pi\rho \sum_{m=-\infty}^{\infty} \delta(t - t' - 2\pi m\rho)\,. \tag{6.4.7}$$

Thus

$$\sum_m b_m(t) = -2\pi i\beta\rho \left[\tfrac{1}{2} a(t) + \sum_{m=1}^{\infty} \bar{\beta}^m a(t - m\tau_R)\, \theta(t - m\tau_R)\right] \tag{6.4.8}$$

where θ is the unit step function and

$$\tau_R = 2\pi\rho \tag{6.4.9a}$$

$$\bar{\beta} = \exp\{-i(\Delta + \bar{\Delta}_0)\tau_R\}\,. \tag{6.4.9b}$$

Using this result in (6.4.1a), we obtain a time-delay differential equation for a:

$$\dot{a}(t) = -i\Delta\, a(t) - \frac{\gamma}{2} a(t) + 2i\chi\, a(t)\,|a(t)|^2 - i\Omega - \gamma \sum_{m=1}^{\infty} \bar{\beta}^m\, a(t - m\tau_R)\,\theta(t - m\tau_R) \tag{6.4.10}$$

where

$$\gamma = 2\pi\beta^2\rho \tag{6.4.11}$$

is simply the decay rate, out of the pump mode, that would be predicted by Fermi's Golden Rule. This exponential decay rate applies in the limit $\tau_R \to \infty$, i.e., when the background level spacing goes to zero and we have the limiting case of a true continuum. We see that τ_R plays the role of a "recurrence time", or the rephasing time of the background modes.

If we set the anharmonicity χ to zero in (6.4.10), the time-delay equation becomes linear and has an exact analytical solution [93]. In this case the system is not chaotic. Similarly if $\tau_R \to \infty$ then (6.4.10) reduces to

$$\dot{a}(t) = -i\Delta\, a(t) - \frac{\gamma}{2} a(t) + 2i\chi\, a(t)\,|a(t)|^2 - i\Omega \tag{6.4.12}$$

which is essentially of the form of the RWA Duffing system (cf. (2.5.4)) and likewise does not exhibit any chaotic behavior. In other words, chaos can only occur in our model if (1) there is an anharmonicity $\chi \neq 0$, and (2) the background mode frequencies do not form a continuum. We shall see that when (1) and (2) are satisfied the system (6.4.10) describing the pumped mode dynamics is indeed chaotic.

For $t < \tau_R$ eq. (6.4.10) reduces to (6.4.12). The only effect of the background for such times is to cause exponential decay from the pump mode at the Golden Rule rate. At $t = \tau_R$, however, the background "signals" back to the pump mode. This feedback is evident in the equation

$$\dot{a}(t) = -i\Delta\, a(t) - \frac{\gamma}{2} a(t) + 2i\chi\,|a(t)|^2\, a(t) - i\Omega - \gamma\bar{\beta}\, a(t - \tau_R) \qquad (\tau_R < t < 2\tau_R)\,. \tag{6.4.13}$$

In general the behavior of $a(t)$ on the interval $m\tau_R < t < (m+1)\tau_R$ is affected by its behavior on *all* earlier intervals. The phase $\bar{\beta}$ determines how the relative location of the band origins affects the absorption and emission of photons by the molecule.

Equation (6.4.10) has some useful scaling relations. Let us define

$$\tilde{a} = \frac{\gamma}{\Omega} a \tag{6.4.14a}$$

$$\alpha = \frac{\Omega^2}{\gamma^3}\chi \tag{6.4.14b}$$

$$T = \gamma t \tag{6.4.14c}$$

$$T_R = \gamma \tau_R \,. \tag{6.4.14d}$$

Then we may write (6.4.10) in the form

$$\dot{\bar{a}}(T) = -i\frac{\Delta}{\gamma}\bar{a}(T) - \tfrac{1}{2}\bar{a}(T) + 2i\alpha\,|\bar{a}(T)|^2\,\bar{a}(T) - i - \sum_{m=1}^{\infty}\bar{\beta}^m\,\bar{a}(T - mT_R)\,\theta(T - mT_R)\,. \tag{6.4.15}$$

On resonance ($\Delta = 0$), this equation depends on only two variables, α and $\bar{\beta}$. For simplicity we will henceforth restrict our discussion to this case of exact resonance.

The rescaling (6.4.14) not only simplifies the parameter space, but also elucidates some of the physics. If the relaxation constant γ is very large, for instance, and the laser cannot pump the molecule very far up the vibrational ladder, then the scaled system will have a small anharmonicity α. But if the laser power is large, then the molecule can be pumped fairly far up the ladder, and the scaled model will have an effectively large anharmonicity. Both of these physically intuitive effects demonstrate the equivalence of many different molecules with respect to relaxation, laser power, and anharmonicity.

If the relaxation is very fast ($\gamma\tau_R \gg 1$), then on each interval $(mT_R < T < (m+1)T_R)$ $\bar{a}$ quickly approaches a "steady state" for that interval [133]. Then we can set $\dot{\bar{a}} = 0$, and (6.4.15) reduces to an equation for the steady state on interval N as a function of the steady states of all earlier intervals:

$$\begin{aligned}\{\tfrac{1}{2} - 2i\alpha\,|\bar{a}_N|^2\}\,\bar{a}_N &= -i - \sum_{m=1}^{N}\bar{\beta}^m\bar{a}_{N-m} \\ &= -i - \sum_{m=0}^{N-1}\bar{\beta}^{N-m}\bar{a}_m\end{aligned} \tag{6.4.16}$$

where $\bar{a}_N$ denotes the steady-state amplitude on the interval $NT_R < T < (N+1)T_R$. Equation (6.4.16) implies that

$$\{\tfrac{1}{2} - 2i\alpha\,|\bar{a}_N|^2\}\,\bar{a}_N = -i(1-\bar{\beta}) - \bar{\beta}\{\tfrac{1}{2} + 2i\alpha\,|\bar{a}_{N-1}|^2\}\bar{a}_{N-1} \tag{6.4.17}$$

where $\bar{a}_0$ satisfies

$$\{\tfrac{1}{2} - 2i\alpha\,|\bar{a}_0|^2\}\,\bar{a}_0 = -i\,. \tag{6.4.18}$$

If we define

$$c_N = \{\tfrac{1}{2} - 2i\alpha\,|\bar{a}_N|^2\}\,\bar{a}_N \tag{6.4.19a}$$

$$d_N = \{\tfrac{1}{2} + 2ia\,|\bar{a}_N|^2\}\,\bar{a}_N \tag{6.4.19b}$$

then

$$|\bar{a}_N|^2 = f(|c_N|^2) = f(|d_N|^2) \equiv f_N \tag{6.4.20}$$

since $|c_N| = |d_N|$. Here f is the cubic function for $|\bar{a}_N|^2$ implied by (6.4.19), and has only one real root:

$$4\alpha^2|\bar{a}_N|^6 + \tfrac{1}{4}|\bar{a}_N|^2 - |c_N|^2 = 0\,. \tag{6.4.21}$$

Using the definition of f, we can rewrite (6.4.17) as

$$c_N = -\mathrm{i}(1-\bar{\beta}) - \bar{\beta}\left[\frac{\frac{1}{2}+2\mathrm{i}\alpha f_{N-1}}{\frac{1}{2}-2\mathrm{i}\alpha f_{N-1}}\right] c_{N-1}\,. \tag{6.4.22}$$

The factor in square brackets is simply a phase factor:

$$\exp(\mathrm{i}\Phi_N) \equiv (\tfrac{1}{2}+2\mathrm{i}\alpha f_N)/(\tfrac{1}{2}-2\mathrm{i}\alpha f_N) \tag{6.4.23}$$

and so

$$c_N = -\mathrm{i}(1-\bar{\beta}) - \bar{\beta}\exp(\mathrm{i}\Phi_{N-1})\, c_{N-1} \tag{6.4.24}$$

where $c_0 = -\mathrm{i}$.

Under the assumption of fast relaxation to a steady state on each interval, therefore, we have reduced (6.4.15) to the discrete mapping (6.4.24). In this mapping the solution for c_{N-1} is needed to get $\exp(\mathrm{i}\Phi_{N-1})$. If the system is harmonic ($\alpha = 0$) then from (6.4.23) we have $\exp(\mathrm{i}\Phi_N) = 1$, giving us simply

$$c_N = -\mathrm{i}(1-\bar{\beta}) - \bar{\beta}c_{N-1} \tag{6.4.25}$$

with solution

$$c_N = -\mathrm{i}\left\{\frac{-2(-\bar{\beta})^{N+1} + 1 - \bar{\beta}}{1+\bar{\beta}}\right\}. \tag{6.4.26}$$

Thus there is an N-cycle (i.e., $c_N = c_0$) when $(-\bar{\beta})^N = 1$. If $\bar{\beta} = -1$ we apply l'Hospital's rule to (6.4.26) to obtain

$$c_N = -\mathrm{i}[2(N+1) - 1] \tag{6.4.27}$$

which of course is not cyclical. Although the harmonic case has a fairly rich structure, the mapping in this case does not admit chaos. In the following section we will also consider the discrete mapping in the anharmonic case. In either case the discrete mapping is obtained only under the assumption that a steady state is reached on each interval; this ignores the influence on a given interval of the dynamics from previous intervals. Comparison with the results for the system (6.4.15) *without* this assumption shows, as we shall see, that such "memory" effects are very important.

6.5. Chaotic behavior in multiple photon excitation

Before considering some of the time dynamics let us consider some parameter values characteristic of real molecules. Laser intensities of 1–16 MW/cm^2 are common in multiple photon excitation experiments; this translates into $0.1 \leq \Omega \leq 0.4\ \text{cm}^{-1}$ for the Rabi frequency in wave numbers. We would expect densities of background states in the 1–4/cm^{-1} regime and possibly higher. Coupling parameters in the range 0.1–0.4 cm^{-1}, comparable to the Rabi frequency, are also expected. These parameter values give $\gamma \sim 0.8$–$1\ \text{cm}^{-1}$ ($\gamma^{-1} \sim 5$ psec) and $\tau_R \sim 30$–130 psec. A reasonable value of χ would be $\sim 2\ \text{cm}^{-1}$, which gives $\alpha \leq 0.5$ for the anharmonicity of the scaled model.

In the resonant case $\bar{\beta} = \exp(-i\bar{\Delta}_0\tau_R) = \exp(-i\phi)$, where

$$\phi = \bar{\Delta}_0\tau_R = 2\pi(\bar{\Delta}_0\rho) \tag{6.5.1}$$

and ρ, we recall, is the inverse of the background level spacing. Thus, if $\bar{\Delta}_0$ is halfway between background levels, $\bar{\Delta}_0\rho = \frac{1}{2}$ and $\phi = \pi$. If $\bar{\Delta}_0$ is on a background level, $\bar{\Delta}_0\rho = 0$ and $\phi = 0$. We will focus our attention on the resonant case.

By numerically integrating (6.4.15), we can compute the average number of photons absorbed by the pump mode and also, by (6.4.4), the total number of photons absorbed from the applied field by the pump and background modes. In fig. 6.2 we plot the average number of photons absorbed by the pump mode over a time 5 T_R for the *harmonic* case $\alpha = 0$ with $\phi = \pi/2$, $\beta = 0.2\ \text{cm}^{-1}$, $\rho = 4$ cm, $\Omega = 0.3\ \text{cm}^{-1}$ (9 MW/cm^2 in SF_6). (In this figure and those which follow, it is important to note that the number of "photons" plotted is actually the scaled number $|\bar{a}|^2 = (\gamma/\Omega)^2|a|^2$. For the chosen values of γ and Ω, therefore, the actual predicted photon numbers are an order of magnitude less than the *scaled* number that is plotted.) On the first interval we observe the expected exponential relaxation to the steady-state value indicated by a small box at the end of the interval. From (6.4.26) we expect this choice of ϕ to give a 4-cycle; note, however, that the *approach* to steady state is different on the first and fourth intervals. In fig. 6.3 we plot the total number of photons absorbed, which is observed to give a linear

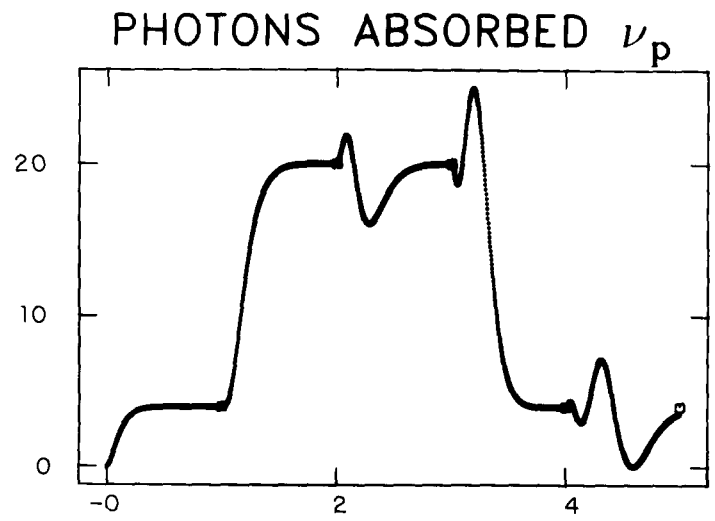

Fig. 6.2. Average number of photons absorbed by a harmonic pump mode, plotted for 5 T_R. A box at the end of each interval gives the steady-state solution predicted by the discrete mapping. Parameters are $\alpha = \Delta = 0$, $\rho = 4$ cm, $\beta = 0.2\ \text{cm}^{-1}$, $\Omega = 0.3\ \text{cm}^{-1}$, $\phi = \pi/2$.

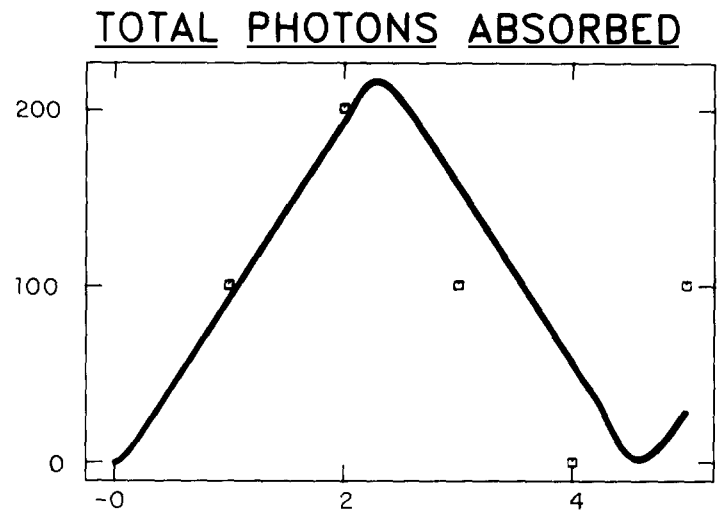

Fig. 6.3. Total number of photons absorbed for the parameters of fig. 6.2.

variation on each interval. Again the predicted steady-state number of photons absorbed is indicated by a box at the end of each interval. We see that the steady-state prediction becomes inapplicable after a few intervals. The reason for this breakdown in the steady-state prediction is simply the carryover in the full dynamical solution from one interval into the next, as mentioned at the end of the preceding section. Physically, the pumped mode may reach a steady state on each interval and stop absorbing photons, but the background modes of the molecule continue to take up energy from the laser, using the pump mode as an intermediary. Whether the molecule absorbs or emits photons depends on the interval and the value of ϕ. The importance of ϕ may be seen by comparing fig. 6.2 with figs. 6.4 and 6.5, which are for $\phi = 0$ and $\phi = \pi$, respectively. For $\phi = \pi$ (fig. 6.5), for instance, we observe the absorption proportional to N^2, for large N, as predicted by (6.4.27).

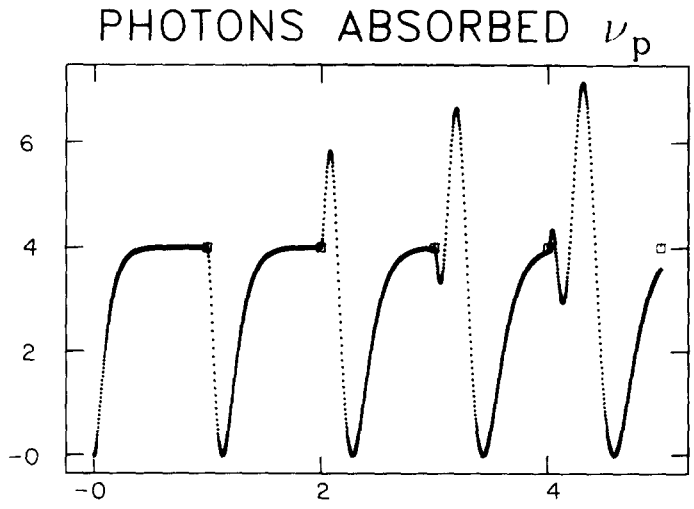

Fig. 6.4. Same as fig. 6.2 except $\phi = 0$.

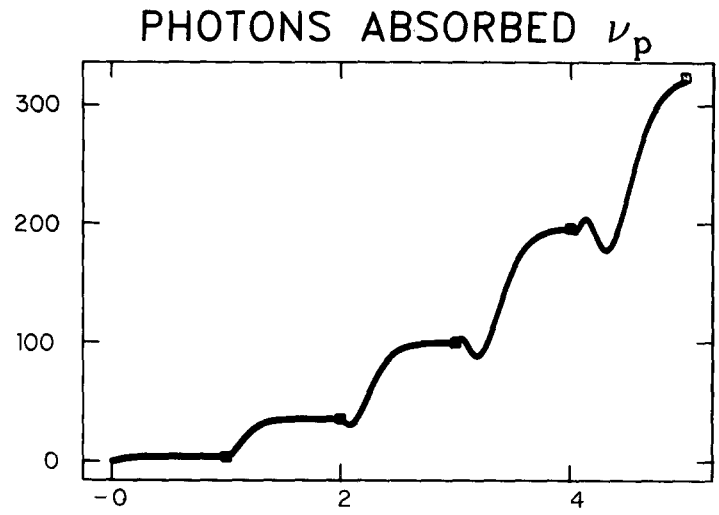

Fig. 6.5. Same as fig. 6.2 except $\phi = \pi$.

Of course the situation of real interest corresponds to an anharmonicity $\alpha \neq 0$. For fig. 6.6 all the parameters are identical to those in fig. 6.2, except that we have now introduced an anharmonicity $\alpha = 0.5$. We note that, although the anharmonicity apparently adds more ringing to the dynamics, the predicted steady-state values indicated by the boxes are still accurate. In fig. 6.7 we plot the total (scaled) number of photons absorbed for the same case, but with the time extended to 150 T_R. *The steady-state predictions based on the discrete mapping of the preceding section are observed to be completely invalid for the long-term dynamics.* The time dynamics appears to go chaotic, and shows a *linear absorption rate* with some "noise" superimposed.

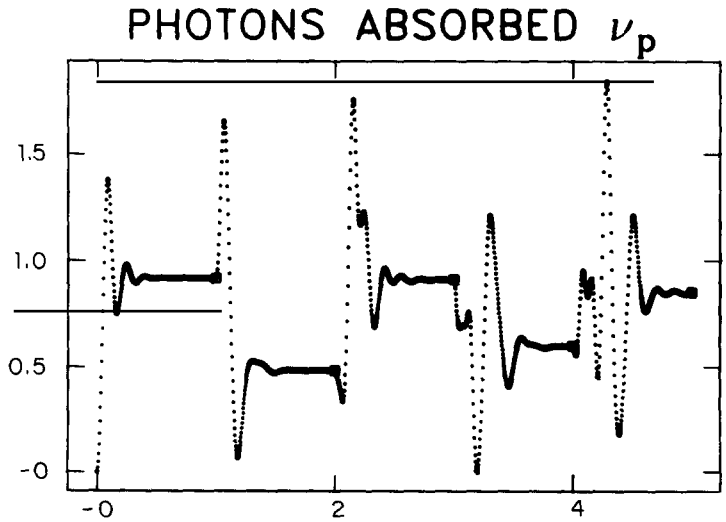

Fig. 6.6. Same as fig. 6.2 except $\alpha = 0.5$.

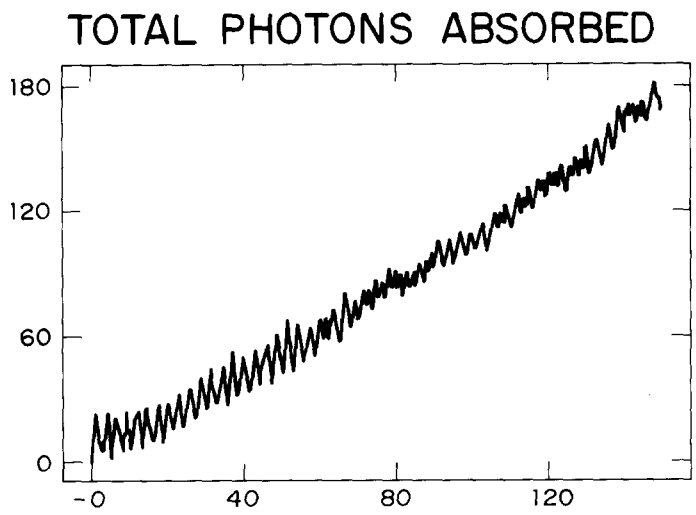

Fig. 6.7. Total number of photons absorbed for the same parameter values as in fig. 6.2, extending the integration to 150 T_R.

To see explicitly that the dynamics is chaotic, we have computed the power spectrum (fig. 6.8) and the maximal Lyapunov exponent. For different values of ϕ the system is still found to be chaotic, but the slope of the approximately linear absorption curve is dependent on the value of ϕ. We have not found a threshold for the onset of chaos, which we now believe is a characteristic mode of behavior in multiple-photon absorption experiments. *The linear absorption implies a fluence-dependent absorption.* Furthermore this feature is a *unimolecular* effect.

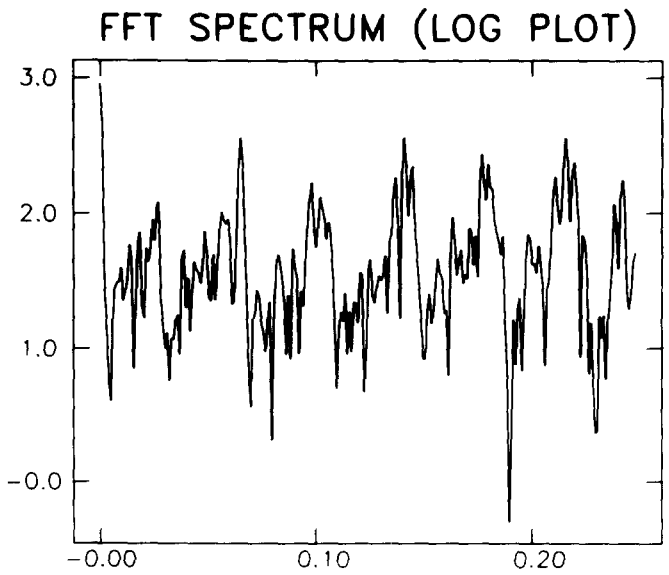

Fig. 6.8. Power spectrum corresponding to fig. 6.7.

6.6. Discussion of the role of chaos

We can summarize our investigations of multiple photon absorption based on the Hamiltonian (6.3.2), with the QC assumption (6.3.4), as follows: For realistic molecular and driving-field parameters, the time evolution of the driven molecular vibrations is chaotic. As a consequence, the absorption of energy from the laser is approximately proportional to the time. This may be understood roughly as follows.

From (6.4.5) we have

$$\sum_{m=-\infty}^{\infty} |b_m(t)|^2 = \gamma \int_0^t \mathrm{d}t' \int_0^t \mathrm{d}t''\, a^*(t')\, a(t'') \sum_{m=-\infty}^{\infty} \bar{\beta}^m\, \delta(t''-t'-m\tau_R) \tag{6.6.1}$$

where we have again used (6.4.7). The total excitation number in the background modes may thus be written in the form

$$\sum_{m=-\infty}^{\infty} |b_m(t)|^2 = \gamma \int_0^t \mathrm{d}t'\, a^*(t')\, a(t') + 2\,\mathrm{Re} \sum_{m=1}^{\infty} \bar{\beta}^m\, \theta(t-m\tau_R) \int_0^{t-m\tau_R} \mathrm{d}t'\, a^*(t')\, a(t'+m\tau_R)\,. \tag{6.6.2}$$

The second term involves the time-averaged correlation function $\langle a^*(t)\, a(t+\tau)\rangle_t$. As is the case with the logistic map or the Lorenz model, we find that correlations decay from their $\tau = 0$ values (but not necessarily to zero). The major contribution is then from the first term, which describes, in a simple rate-equation fashion, the growth of the background-mode excitation at the expense of the pump mode. The growth rate is just $\gamma a^* a$, where γ is the Golden Rule rate and $a^* a$ is the number of quanta in the pump mode. It is this rate that gives rise to an approximately linear increase with time of the total background-mode excitation number (6.6.2). This interpretation has been checked quantitatively. The chaos, which causes the correlations in the pumped-mode amplitude to decay, is in this way responsible for the incoherent energy deposition into the molecule.

Note that the incoherent absorption is found without recourse to coherence-destroying damping terms in the model. In other words, the incoherent, predominantly fluence-dependent absorption is a *collisionless* effect, a characteristic of an individual molecule.

One might expect it to be difficult to dissociate a molecule with radiation of one frequency, for the anharmonicity destroys the equal level spacing of the harmonic oscillator, and the system is effectively off-resonant after the absorption of a few photons. It therefore came as a surprise when SiF_4, for instance, was found to dissociate rather easily [137]. This led to considerable interest in the possibility of bond-selective photochemistry and laser isotope separation. It gradually became clear, however, that for most molecules the intramolecular relaxation of the pump mode into the background modes redistributes the absorbed energy too rapidly to achieve these goals efficiently. In fact it became customary to assume a statistical energy distribution in the background modes. This background (the quasi-continuum) was modeled by rate equations, which naturally gave a strongly fluence-dependent absorption, consistent with experiment.

The dependence of multiple photon absorption on pulse energy rather than intensity has been found for about 50 polyatomic molecules by Lyman et al. [138, 139]. Since an average over homogeneous and

inhomogeneous linewidths could lead to an explanation of this lack of laser-molecule coherence, it has usually been assumed that hotband and rotational averaging are responsible for this effect. In the following section we consider a model including molecular rotation, and show that rotational effects cannot be treated simply as a sort of inhomogeneous broadening.

6.7. Chaos in a vibration-rotation model

The Hamiltonian (6.3.1) does not include molecular rotation. We will now include rotations, but for simplicity (and in order to isolate some of the effects) we will neglect anharmonicity and intramolecular coupling. We consider a triply-degenerate harmonic oscillator coupled to an applied laser field and allowed to rotate. From (6.2.2) we can identify the Hamiltonian for this system as [140]

$$H = \Delta \boldsymbol{a}^\dagger \cdot \boldsymbol{a} + B_0 \boldsymbol{J}^2 + \Omega \hat{\boldsymbol{\varepsilon}} \cdot \overleftrightarrow{\mathbb{C}} \cdot (\boldsymbol{a} + \boldsymbol{a}^\dagger) . \tag{6.7.1}$$

The (classical) equations of motion obtained from this Hamiltonian are

$$\dot{\boldsymbol{a}} = -\mathrm{i}\Delta \boldsymbol{a} - \mathrm{i}\Omega \boldsymbol{P} \tag{6.7.2a}$$

$$\dot{\boldsymbol{P}} = -2B_0(\boldsymbol{J} \times \boldsymbol{P}) \tag{6.7.2b}$$

$$\dot{\boldsymbol{J}} = \Omega \boldsymbol{P} \times (\boldsymbol{a} + \boldsymbol{a}^*) \tag{6.7.2c}$$

where we have defined

$$\boldsymbol{P} = \hat{\boldsymbol{\varepsilon}} \cdot \overleftrightarrow{\mathbb{C}} . \tag{6.7.2d}$$

We recall from section 6.2 that $\hat{\boldsymbol{\varepsilon}}$ is the laser polarization vector, the components of which are referred to the lab frame; $\boldsymbol{a}$ and $\boldsymbol{a}^*$ for the infrared-active mode of the molecule have components referred to body-fixed axes; and $\overleftrightarrow{\mathbb{C}}$ is the 3×3 orthogonal matrix relating the lab and body frames. Physically, eq. (6.7.2b) describes a precession of the *body-fixed* components of the laser polarization vector (i.e., $\hat{\boldsymbol{\varepsilon}} \cdot \overleftrightarrow{\mathbb{C}}$) about the total angular momentum vector $\boldsymbol{J}$. In what follows we assume the initial conditions

$$\boldsymbol{a}(0) = (0, 0, 0) \tag{6.7.3a}$$

$$\boldsymbol{J}(0) = (0, 0, J_0) \tag{6.7.3b}$$

$$\boldsymbol{P}(0) = (1/\sqrt{2}, 0, 1/\sqrt{2}) . \tag{6.7.3c}$$

Let us note first that, were $\boldsymbol{J}$ taken to be a constant of the motion by deleting (6.7.2c) from the set (6.7.2), then from (6.7.2a) and (6.7.2b), setting $\boldsymbol{J} = J_0 \hat{\boldsymbol{z}}$, we calculate

$$\boldsymbol{P}(t) = \frac{1}{\sqrt{2}} (\cos 2B_0 J_0 t, \sin 2B_0 J_0 t, 1) . \tag{6.7.4}$$

Using this result in (6.7.2a), we obtain

$$|a|^2 = \Omega^2 \left\{ \frac{1-\cos(\Delta + 2B_0J_0)t}{2(\Delta + 2B_0J_0)^2} + \frac{1-\cos(\Delta - 2B_0J_0)t}{2(\Delta - 2B_0J_0)^2} + \frac{1-\cos \Delta t}{\Delta^2} \right\}. \tag{6.7.5}$$

In our calculations we have set $B_0 = 0.1\ \mathrm{cm}^{-1}$, a characteristic value for molecules with large moments of inertia (e.g., SF_6), $\Omega = 1\ \mathrm{cm}^{-1}$ and $\Delta = 0.5\ \mathrm{cm}^{-1}$. The vibrational energy given by (6.7.5) is much greater than the rotational energy. The resonances at $\Delta = \pm 2B_0J_0$ and $\Delta = 0$ will be recognized as the P, Q and R branches of the spectrum [141].

In fig. 6.9 we plot $|a|^2$, given by (6.7.5) with $J_0 = 5$, as a function of t. For our choice of parameters, $\Delta \pm 2B_0J_0 = 1.5$, $-0.5\ \mathrm{cm}^{-1}$, respectively, with $\Delta = 0.5\ \mathrm{cm}^{-1}$. Figure 6.10 is a plot of P_x vs. P_y, showing the simple precession of $\boldsymbol{P}$ about $\boldsymbol{J}$ (in the z direction) in this case $\boldsymbol{J}$ = constant.

Let us now consider the full set of equations (6.7.2), with $\boldsymbol{J}$ no longer a constant of the motion but satisfying (6.7.2c). In this case we obviously have a nonlinear set of equations. Figures 6.11 and 6.12 show $|a|^2$ and P_x vs. P_y, assuming $J_0 = 5$ for the magnitude of the initial angular momentum (eq. (6.7.3b)). Figure 6.11 shows an erratic energy deposition in the pump mode, in marked contrast to the case shown in fig. 6.9. Figure 6.12 shows the erratic motion of the polarization vector, which is attempting to precess about a *moving* $\boldsymbol{J}$ vector. It is evident that $\boldsymbol{J}$ here is *not* a constant of the motion. The power spectra computed for $|a|^2$ and P_x, P_y strongly suggest that the dynamics of the pumped vibration-rotation model is chaotic. That the motion is indeed chaotic has been confirmed by the convergence of the maximal Lyapunov exponent to a positive value.

The chaos is associated with nonconservation of the molecular angular momentum. We have $\boldsymbol{J} = \boldsymbol{J}_0 + \boldsymbol{L}$, where [142]

$$\boldsymbol{L} = \mathrm{i}(\boldsymbol{a} \times \boldsymbol{a}^*) \tag{6.7.6}$$

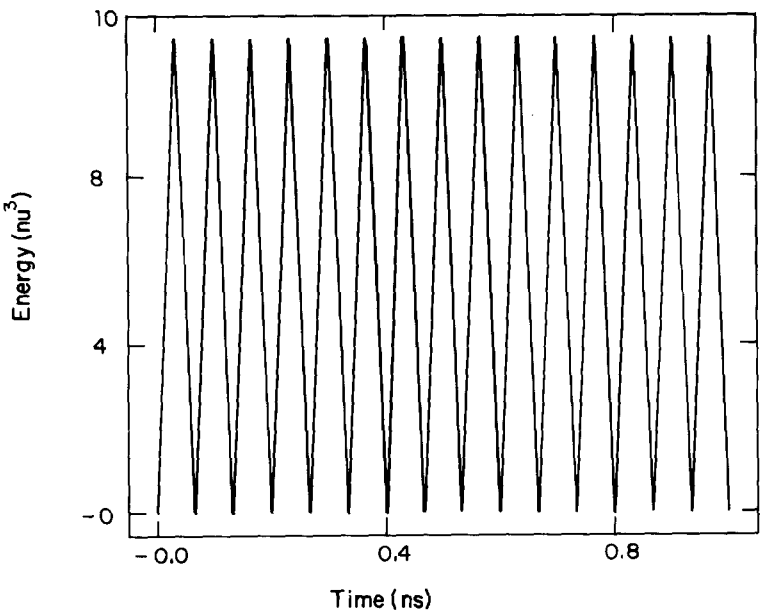

Fig. 6.9. Energy in pumped mode in the vibration-rotation model with $\boldsymbol{J}$ held constant, $\Delta = 0.5\ \mathrm{cm}^{-1}$, $\Omega = 1\ \mathrm{cm}^{-1}$, $B_0 = 0.1\ \mathrm{cm}^{-1}$ and $J_0 = 5$.

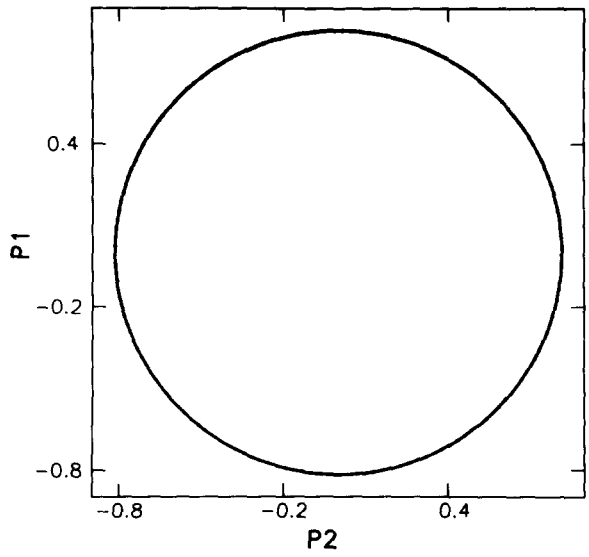

Fig. 6.10. P_x vs. P_y for the parameters of fig. 6.9.

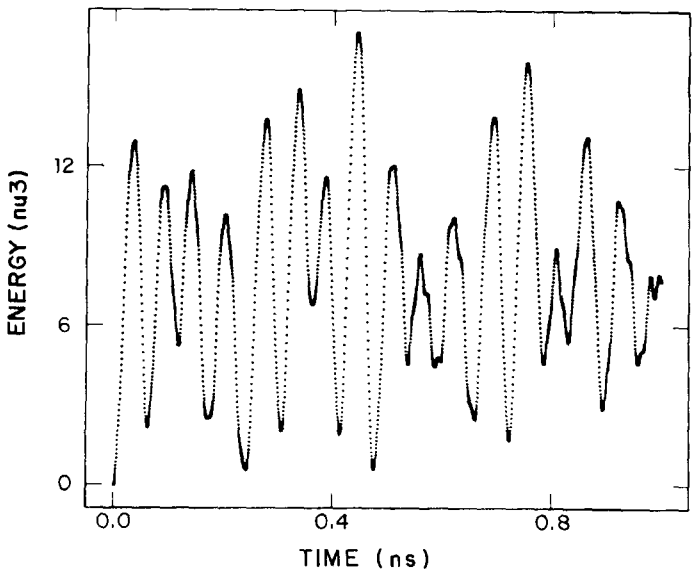

Fig. 6.11. Same as fig. 6.9 except J is not held constant.

is the vibrational angular momentum. Since $|L|^2 \lesssim |\boldsymbol{a}|^2$, a large value of $|\boldsymbol{a}|^2$ results in a value of L large compared with J_0, and a destabilization of the motion of $\boldsymbol{P}$. For $J_0 \gg L$, on the other hand, there is basically a simple precession of $\boldsymbol{P}$ about $\boldsymbol{J}$: the dynamics are gyroscopically stabilized. In this case the motion is not chaotic. In other words, the chaos is dominant when the photon absorption ($|\boldsymbol{a}|^2$) exceeds the $t = 0$ angular momentum J_0, i.e., under strong driving conditions. Similar conclusions are deduced from the consideration of parallel and perpendicular bands of symmetric-top and asymmetric-top molecules of nondegenerate and doubly degenerate infrared-active modes. These studies show that

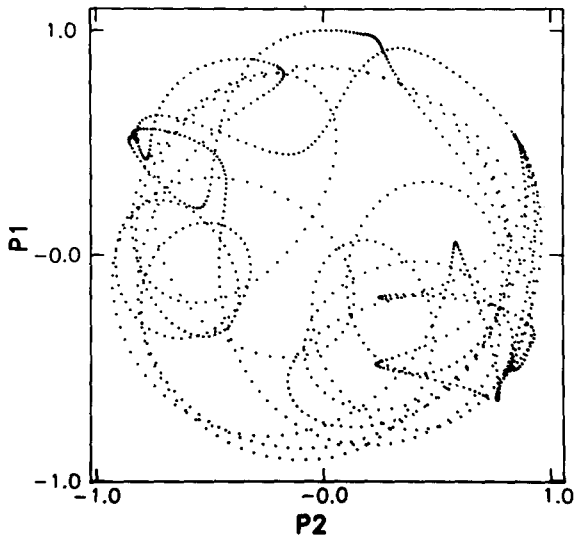

Fig. 6.12. Same as fig. 6.10 except J is not held constant.

molecular rotations cannot be treated cavalierly as simple inhomogeneous broadening, because the molecule–field interaction strongly couples the rotational and vibrational motion [140].

6.8. Discussion

We have found chaos in a quite reasonable model of multiple-photon infrared absorption by polyatomic molecules. Both the vibrational anharmonicity and the coupling of the pumped mode to infrared-inactive modes are essential for chaos; the latter effect has been treated using the quasi-continuum model employed earlier in radiationless transition theory.

The appearance of chaos explains several features of multiple-photon infrared absorption. First, we have found that the energy in the molecule increases, approximately linearly, with time. This flow of energy from the laser to the molecule does not require any collisions. Indeed we have not put any damping or de-phasing processes into the model. The chaos leads to a practically irreversible flow of energy from the pumped mode to the background modes, which thus act effectively as a sponge for the laser energy. This occurs in spite of the fact that the density of background modes may not be sufficient to justify *a priori* the assumption of irreversible decay.

The energy deposited into the molecule is found to be (approximately) fluence-dependent, in agreement with general trends found experimentally. We can thus understand some important aspects of multiple-photon excitation of large polyatomic molecules that are found experimentally but have hitherto not been satisfactorily explained: (1) The molecules readily absorb tens of photons without any bottlenecking arising from their anharmonicity; (2) the process is strongly fluence dependent, and (3) it does not require molecular collisions. According to the present theory, these features should hold also in low-temperature experiments, where rotational degrees of freedom are "frozen out". The molecular rotation, however, can itself give rise to chaotic behavior, as we saw in the preceding section.

We have recently learned that chaotic dynamics has also been discussed by some Russian authors in connection with multiple-photon excitation and dissociation. In particular, Belobrov et al. [143] have found in a rather different model exhibiting chaos that "stochastic excitation" of high vibrational states

can be realized. Some time ago Zaslavskii and Chirikov [144] noted that the energy of a driven, undamped pendulum can increase on average with time when its motion is chaotic. These results suggest that our conclusions about the role of chaos in multiple-photon absorption may be valid independently of the details of a specific model.

Such a "diffusive" excitation process associated with chaotic dynamics has also been proposed to explain the *microwave* excitation and ionization of Rydberg atoms observed by Bayfield and Koch. [145]. Classical models put forth by Delone et al. [146], Leopold and Percival [147] and Meerson et al. [148] seem to be consistent with the experimental results. Leopold and Percival [147], for instance, work with the classical Hamiltonian

$$H = \tfrac{1}{2}P^2 - 1/r + zE\cos\omega t \tag{6.8.1}$$

and choose initial conditions by a Monte Carlo method (classical microcanonical ensemble) to incorporate the degenerate (l, m) states for a given principal quantum number n. Results in excellent agreement with experiment [145] were obtained, but of course alternative explanations cannot be ruled out [146]. It may be worth noting that in this case of atomic diffusive excitation there is no obvious resonance such as occurs in our molecular vibration model, where the applied field is nearly resonant with the approximately harmonic vibrational ladder.

This diffusive excitation (and ionization) process proposed for Rydberg atoms in microwave fields is based, as in our model of multiple-photon excitation (and dissociation) for molecules in infrared fields, on the classical approximation. And therefore the old question of quantum chaos again arises: what happens quantum mechanically when the corresponding classical system is chaotic?

Classical chaos is by now fairly well understood, and can be identified unambiguously (i.e., a positive Lyapunov exponent); this seems especially true in light of the universal routes to chaos known for dissipative systems. Part of the difficulty with *quantum* chaos is semantic, as there seems to be no consensus as to how one should *define* quantum chaos. For instance, if one insists on defining chaos in terms of a nondiscrete spectrum, then the discrete energy spectrum in our model of infrared multiple-photon excitation [149] implies that there can be no chaotic (quantum) behavior! [150].

As mentioned in section 3.7, there are quantum manifestations of classical chaos [56–62]. In the absence of any consensus on a definition of quantum chaos, however, it seems fruitless at this point to argue whether our model of infrared multiple-photon absorption does or does not admit quantum chaos. What we suggest will survive a quantum treatment of our model is the strong fluence dependence of the process and the effectively irreversible influence of the quasi-continuum on the pumped mode. Work is now in progress to investigate quantum corrections to the classical model.

Acknowledgements

We have many people to thank for discussions and encouragement, especially Dr. H.W. Galbraith. We also thank Drs. D. Campbell, H.J. Carmichael, J.H. Eberly, J.D. Farmer, E.J. Heller, G. Mayer-Kress, S. Singh and D.K. Umberger for helpful remarks. Drs. N.B. Abraham, F.T. Arecchi, L.W. Casperson, H.J. Carmichael, H. Nakatsuka, C.O. Weiss and A. Zardecki kindly supplied figures from their work or gave us permission to reproduce published figures. Permission from the publishers is also gratefully acknowledged. Research at Arkansas was supported in part by NSF grant PHY-8308048 and by dual funding from NSF EPSCOR grant ISP 8011444 and the State of Arkansas. P.W. Milonni

gratefully acknowledges the Los Alamos National Laboratory for supporting him as a Visiting Staff Member during the initial stages of this collaboration. Finally, we are particularly grateful to an anonymous referee for carefully reading the manuscript and helping us to improve it.

References

[1] R. Abraham, quoted in: Newsweek, 18 July 1983, p. 53.
[2] R.M. May, Nature 261 (1976) 459.
[3] M.J. Feigenbaum, J. Stat. Phys. 19 (1978) 25; 21 (1979) 669.
[4] M.J. Feigenbaum, Los Alamos Science (Summer, 1980) pp. 4–27.
[5] D.R. Hofstadter, Scientific American (November 1981) pp. 22–43.
[6] B.A. Huberman and J. Rudnick, Phys. Rev. Lett. 45 (1980) 154.
[7] A.N. Šarkovskii, Ukr. Mat. Zh. 16 (1964) 61.
[8] P. Štefan, Commun. Math. Phys. 54 (1977) 237.
[9] T.-Y. Li and J. Yorke, Amer. Math. Monthly 82 (1975) 985.
[10] M. Kac and S.M. Ulam, Mathematics and Logic (New American Library, N.Y., 1969) p. 23.
[11] M. Hénon, Commun. Math. Phys. 50 (1976) 69.
[12] B. Derrida, A. Gervois and Y. Pomeau, J. Phys. A12 (1979) 269.
[13] D.A. Russell, J.D. Hanson and E. Ott, Phys. Rev. Lett. 45 (1980) 1175.
[14] J.R. Ackerhalt, H.W. Galbraith and P.W. Milonni, Chaos in radiative interactions, in: Quantum Electrodynamics and Quantum Optics, ed. A.O. Barut (Plenum, N.Y., 1984).
[15] S.D. Feit, Commun. Math. Phys. 61 (1978) 249.
[16] B. Mandelbrot, Fractals (W.H. Freeman, San Francisco, 1977).
[17] E.N. Lorenz, J. Atmos. Sci. 20 (1963) 130; Tellus 16 (1964) 1.
[18] C. Sparrow, The Lorenz Equations: Bifurcations, Chaos, and Strange Attractors (Springer-Verlag, N.Y., 1982).
[19] A.A. Andronov and C.E. Chaikin, Theory of Oscillations (Princeton University Press, N.J., 1949).
[20] N. Minorsky, Nonlinear Oscillations (Van Nostrand, N.Y., 1962).
[21] J.W. Cooley and J.W. Tukey, Math. Comp. 19 (1965) 297.
[22] See, for instance, G.D. Bergland, IEEE Spectrum 42 (1969).
[23] L. Cesari, Asymptotic Behavior and Stability Problems in Ordinary Differential Equations (Academic Press, N.Y., 1963).
[24] G. Benettin, L. Galgani and J.-M. Strelcyn, Phys. Rev. A14 (1976) 2338.
[25] G. Benettin, L. Galgani, A. Giorgilli and J.-M. Strelcyn, Meccanica 15 (1980) 9 and 15 (1980) 27.
[26] B.A. Huberman and J.P. Crutchfield, Phys. Rev. Lett. 43 (1979) 1743.
[27] L.D. Landau and E.M. Lifschitz, Mechanics (Pergamon, N.Y., 1976) Chapter V.
[28] S. Novak and R.G. Frehlich, Phys. Rev. A26 (1982) 3660.
[29] J.N. Elgin, D. Forster and S. Sarkar, Phys. Lett. 94A (1983) 195.
[30] J.R. Ackerhalt, H.W. Galbraith and P.W. Milonni, in: Coherence and Quantum Optics, eds. L. Mandel and E. Wolf (Plenum, N.Y., 1984).
[31] See, for instance, J.E. Marsden and M. McCracken, The Hopf Bifurcation and Its Applications (Springer-Verlag, Berlin, 1976).
[32] See also Bifurcation Theory and Applications in Scientific Disciplines, eds. O. Gurel and O.E. Rossler, Annals of the New York Academy of Sciences 316 (N.Y. Academy of Sciences, N.Y., 1978).
[33] J.L. Kaplan and J.A. Yorke, Commun. Math. Phys. 67 (1979) 93.
[34] E.D. Yorke and J.A. Yorke, J. Stat. Phys. 21 (1979) 263.
[35] K. Robbins, SIAM J. Appl. Math. 36 (1979) 457.
[36] I. Shimada and T. Nagashima, Prog. Theor. Phys. 61 (1979) 1605.
[37] H. Mori, Prog. Theor. Phys. 61 (1979) 1605.
[38] J.L. Kaplan and J.A. Yorke, in: Functional Differential Equations and Approximation of Fixed Points, eds. H.O. Peitgen and H.O. Walther (Springer, Berlin, 1979).
[39] J.-P. Eckmann, Rev. Mod. Phys. 53 (1981) 643.
[40] See L.D. Landau and E.M. Lifshitz, Fluid Mechanics (Pergamon, London, 1959) Chapter 3.
[41] D. Ruelle and F. Takens, Commun. Math. Phys. 20 (1971) 167.
[42] J.H. Curry and J.A. Yorke, The Structure of Attractors in Dynamical Systems, eds. N.G. Markley, J.C. Martin and W. Perrizo (Springer, Berlin, 1978).
[43] J.H. Curry, Commun. Math. Phys. 60 (1978) 193.
[44] Y. Pomeau and P. Manneville, Commun. Math. Phys. 77 (1980) 189.
[45] P.S. Lindsay, Phys. Rev. Lett. 47 (1981) 1349.

[46] J. Testa, J. Perez and C. Jeffries, Phys. Rev. Lett. 48 (1982) 714.
[47] J.E. Hirsch, B.A. Huberman and D.J. Scalapino, Phys. Rev. A25 (1982) 519.
[48] P.I. Belobrov, G.M. Zaslavskii and G. Kh. Tartakovskii, Sov. Phys. JETP 44 (1976) 945.
[49] P.W. Milonni, J.R. Ackerhalt and H.W. Galbraith, Phys. Rev. Lett. 50 (1983) 966.
[50] E.T. Jaynes and F.W. Cummings, Proc. IEEE 51 (1963) 89.
[51] M. Tavis and F.W. Cummings, Phys. Rev. 170 (1968) 379.
[52] See, for example, L. Allen and J.H. Eberly, Optical Resonance and Two-Level Atoms (Wiley, N.Y., 1975).
[53] J.R. Ackerhalt and P.W. Milonni, J. Opt. Soc. Am. B1 (1984) 116.
[54] E.A. Power and S. Zienau, Phil. Trans. Roy. Soc. A251 (1959) 427.
[55] R. Graham and M. Höhnerbach, Phys. Lett. 101A (1984) 61.
[56] G. Casati, B.V. Chirikov and J. Ford, Lecture Notes in Physics 93, eds. G. Casati and J. Ford (Springer, Berlin, 1979).
[57] E.J. Heller, Chem. Phys. Lett. 60 (1979) 338.
[58] D.W. Noid, M.L. Koszykowski and R.A. Marcus, Ann. Rev. Phys. Chem. 32 (1981) 267.
[59] I.C. Percival, J. Phys. B6 (1974) L229; Adv. Chem. Phys. 36 (1977) 1.
[60] N. Pomphrey, J. Phys. B7 (1974) 1909.
[61] A. Peres, Phys. Rev. A30 (1984) 504;
M. Feingold, N. Moiseyev and A. Peres, Phys. Rev. A30 (1984) 509.
[62] M.V. Berry, The Wave-Particle Dualism, eds. S. Diner, D. Fargue, G. Lochak and F. Selleri (D. Reidel Publishing Co., Dordrecht, Holland, 1984).
[63] J.H. Eberly, N.B. Narozhny and J.J. Sanchez-Mondragon, Phys. Rev. Lett. 44 (1980) 1323.
[64] N.B. Narozhny, J.J. Sanchez-Mondragon and J.H. Eberly, Phys. Rev. A23 (1981) 236.
[65] P.L. Knight and P.M. Radmore, Phys. Rev. A26 (1982) 676.
[66] S.M. Barnett and P.L. Knight, Optica Acta 31 (1984) 435.
[67] H. Haken, Phys. Lett. 53A (1975) 77.
[68] J.H. Shirley, Am. J. Phys. 36 (1968) 949, and references therein.
[69] E.R. Buley and F.W. Cummings, Phys. Rev. 134 (1964) A1454.
[70] H. Risken and K. Nummedal, J. Appl. Phys. 39 (1968) 4662, and references therein.
[71] R. Graham, Phys. Lett. 58A (1976) 440.
[72] K. Kaufmann and G. Marowsky, Appl. Phys. 11 (1976) 47.
[73] M. Mayr, H. Risken and H.D. Vollmer, Opt. Commun. 36 (1981) 480.
[74] L.W. Hillman, J. Kracinski, R.W. Boyd and C.R. Stroud Jr., Phys. Rev. Lett. 52 (1984) 1605.
[75] F.T. Arecchi, R. Meucci, G. Puccioni and J. Tredicce, Phys. Rev. Lett. 49 (1982) 1217.
[76] L.W. Casperson and A. Yariv, Appl. Phys. Lett. 17 (1970) 259.
[77] L.W. Casperson, IEEE J. Quantum Electron. QE-14 (1978) 756.
[78] L.W. Casperson, Laser Physics, eds. J.D. Harvey and D.F. Walls, Lecture Notes in Physics 182 (Springer-Verlag, Berlin, 1983) pp. 88–106.
[79] L.W. Casperson, Phys. Rev. A21 (1980) 911.
[80] M. Abramowitz and I.A. Stegun, Handbook of Mathematical Functions (National Bureau of Standards, Washington, D.C., 1964).
[81] M. Maeda and N.B. Abraham, Phys. Rev. A26 (1982) 3395.
[82] M.L. Minden and L.W. Casperson, IEEE J. Quantum Electron. QE-18 (1982) 1952.
[83] P. Mandel, Opt. Commun. 44 (1983) 400.
[84] L.W. Casperson, Phys. Rev. A23 (1981) 248.
[85] J. Bentley and N.B. Abraham, Opt. Commun. 41 (1982) 52.
[86] R.S. Gioggia and N.B. Abraham, Opt. Commun. 47 (1983) 278.
[87] C.O. Weiss and H. King, Opt. Commun. 44 (1982) 59.
[88] C.O. Weiss, A. Godone and A. Olafsson, Phys. Rev. A28 (1983) 892.
[89] R.S. Gioggia and N.B. Abraham, Phys. Rev. Lett. 51 (1983) 650.
[90] N.J. Halas, S.-N. Liu and N.B. Abraham, Phys. Rev. A28 (1983) 2915.
[91] N.B. Abraham, T. Chyba, M. Coleman, R.S. Gioggia, N.J. Halas, L.M. Hoffer, S.-N. Liu, M. Maeda and J.C. Wesson, in: Laser Physics, ref. [78].
[92] M.-L. Shih, P.W. Milonni and J.R. Ackerhalt, J. Opt. Soc. Am. B2 (1985) 130.
[93] M.-L. Shih, Ph.D. thesis (University of Arkansas, 1984, unpublished).
[94] L.E. Urbach, S.-N. Liu and N.B. Abraham, Coherence and Quantum Optics V, eds. L. Mandel and E. Wolf (Plenum, N.Y., 1984).
[95] See, for instance, Hydrodynamic Instabilities and the Transition to Turbulence, eds. H.L. Swinney and J.P. Gollub, Topics in Applied Physics 45 (Springer-Verlag, New York, 1981).
[96] T. Yamada and R. Graham, Phys. Rev. Lett. 45 (1980) 1322.
[97] H.J. Scholtz, T. Yamada, H. Brand and R. Graham, Phys. Lett. 82A (1981) 321.
[98] F.T. Arecchi, G. Lippi, G. Puccioni and J. Tredicce, in: Coherence and Quantum Optics V, eds. L. Mandel and E. Wolf (Plenum, N.Y., 1984).
[99] R. Graham and Y. Cho, Opt. Commun. 47 (1983) 52.
[100] M. Sargent III, High-Energy Lasers and Their Applications, eds. S.F. Jacobs, M.O. Scully and M. Sargent III (Addison-Wesley, Reading, Mass., 1974) p. 39.

[101] W. Brunner and H. Paul, Opt. and Quantum Electron. 15 (1983) 87.
[102] M. Sargent III, M.O. Scully and W.E. Lamb Jr., Laser Physics (Addison-Wesley, Reading, Mass, 1974).
[103] T.J. Bridges and W.W. Rigrod, IEEE J. Quantum Electron. QE-1 (1965) 303.
[104] M.-L. Shih and P.W. Milonni, Opt. Commun. 49 (1984) 155.
[105] R. Hauck, F. Hollinger and H. Weber, Opt. Commun. 47 (1983) 141.
[106] E. Abraham and S.D. Smith, Rep. Prog. Phys. 45 (1982) 815.
[107] A. Szoke, V. Daneu, J. Goldhar and N.A. Kurnit, Appl. Phys. Lett. 15 (1969) 376.
[108] S.L. McCall, Phys. Rev. A9 (1974) 1515.
[109] K. Ikeda, Opt. Commun. 30 (1979) 257.
[110] R. Bonifacio and L.A. Lugiato, Lett. Nuovo Cimento 21 (1978) 505.
[111] H.M. Gibbs, S.L. McCall and T.N.C. Venkatesan, Phys. Rev. Lett. 36 (1976) 1135.
[112] K. Ikeda, H. Daido and O. Akimoto, Phys. Rev. Lett. 45 (1980) 709.
[113] H. Nakatsuka, S. Asaka, H. Itoh, K. Ikeda and M. Matsuoka, Phys. Rev. Lett. 50 (1983) 109.
[114] H.J. Carmichael, R.R. Snapp and W.C. Schieve, Phys. Rev. A26 (1982) 3408.
[115] A. Zardecki, Phys. Lett. 90A (1982) 274.
[116] H.M. Gibbs, F.A. Hopf, D.L. Kaplan and R.L. Shoemaker, Phys. Rev. Lett. 46 (1981) 474.
[117] R.G. Harrison, W.J. Firth, C.A. Emshary and I.A. Al-Saidi, Phys. Rev. Lett. 51 (1983) 562.
[118] K.J. Blow and N.J. Doran, Phys. Rev. Lett. 52 (1984) 526.
[119] P.W. Milonni, J.R. Ackerhalt and H.W. Galbraith, Phys. Rev. A28 (1983) 887.
[120] J.A. Armstrong, N. Bloembergen, J. Ducuing and P.S. Pershan, Phys. Rev. 127 (1962) 1918.
[121] J.R. Ackerhalt, Phys. Rev. Lett. 46 (1981) 922.
[122] D.S. Ray, Phys. Rev. A29 (1984) 3440.
[123] C.J. Randall and J.R. Albritton, Phys. Rev. Lett. 52 (1984) 1887.
[124] J.R. Ackerhalt, H.W. Galbraith and P.W. Milonni, Phys. Rev. Lett. 51 (1983) 1259.
[125] H.W. Galbraith, J.R. Ackerhalt and P.W. Milonni, J. Chem. Phys. 79 (1983) 5345.
[126] M. Born and R. Oppenheimer, Ann. Physik 84 (1927) 457.
[127] See, for instance, Laser-Induced Chemical Processes, ed. J.I. Steinfeld (Plenum, New York, 1981). Chapter 1, by H.W. Galbraith and J.R. Ackerhalt, has an extensive list of references on multiple photon excitation of SF_6.
[128] M. Bixon and J. Jortner, J. Chem. Phys. 48 (1968) 715.
[129] V.F. Weisskopf and E.P. Wigner, Z. Phys. 63 (1930) 54. An English translation may be found in W.R. Hindmarsh, Atomic Spectra (Pergamon, Oxford, 1967).
[130] J.H. Eberly, J.J. Yeh and C.M. Bowden, Chem. Phys. Lett. 86 (1982) 76.
[131] J.J. Yeh, C.M. Bowden and J.H. Eberly, J. Chem. Phys. 76 (1982) 5936.
[132] H.W. Galbraith, J.R. Ackerhalt and P.W. Milonni, J. Chem. Phys. 78 (1983) 790.
[133] P.W. Milonni, J.R. Ackerhalt, H.W. Galbraith and M.-L. Shih, Phys. Rev. A28 (1983) 32.
[134] W.E. Lamb Jr., in: Laser Spectroscopy III, eds. J. Hall and J. Carlsten (Springer-Verlag, N.Y., 1977); Laser Spectroscopy IV, eds. H. Walther and K. Rothe (Springer-Verlag, N.Y., 1979).
[135] R.B. Walker and R.K. Preston, J. Chem. Phys. 67 (1977) 2017.
[136] L.M. Narducci, S.S. Mitra, R.A. Shatas and C.A. Coulter, Phys. Rev. A16 (1977) 247.
[137] N.R. Isenor and M.C. Richardson, Appl. Phys. Lett. 18 (1971) 224; Opt. Commun. 3 (1971) 360.
[138] J.L. Lyman, G.P. Quigley and O.P. Judd, in: Multiple-Photon Excitation and Dissociation of Polyatomic Molecules, ed. C.D. Cantrell (Springer-Verlag, N.Y., to be published).
[139] O.P. Judd, J. Chem. Phys. 71 (1979) 4515.
[140] H.W. Galbraith, J.R. Ackerhalt and P.W. Milonni, J. Chem. Phys. 79 (1983) 5345.
[141] L.C. Biedenharn and J.D. Louck, Angular Momentum in Quantum Physics, Encyclopedia of Mathematics and Its Applications Volume 8, ed. G.-C. Rota (Addison-Wesley, Reading, Mass., 1981) Section 7.10.
[142] H.W. Galbraith and C.D. Cantrell, The Significance of Nonlinearity in the Natural Sciences, eds. B. Kursunoglu, A. Perlmutter and L. Scott (Plenum, N.Y., 1977).
[143] P.I. Belobrov, G.P. Berman, G.M. Zaslavskii and A.P. Slivinsky, Sov. Phys. JETP 49 (1979) 993.
[144] G.M. Zaslavskii and B.V. Chirikov, Sov. Phys. Usp. 14 (1972) 549.
[145] J.E. Bayfield and P.M. Koch, Phys. Rev. Lett. 33 (1974) 258.
[146] N.B. Delone, B.A. Zon and V.P. Krainov, Sov. Phys. JETP 48 (1978) 223.
[147] J.G. Leopold and I.C. Percival, Phys. Rev. Lett. 41 (1978) 944.
[148] B.I. Meerson, E.A. Oks and P.V. Sasorov, JETP Lett. 29 (1979) 72.
[149] A. Nauts and R.E. Wyatt, Phys. Rev. Lett. 51 (1983) 2238.
[150] T. Hogg and B.A. Huberman, Phys. Rev. Lett. 48 (1982) 711; Phys. Rev. A28 (1983) 22.

Notes added in proof

The number of papers dealing with chaos in quantum optics and electronics has increased dramatically since we began the preparation of this introductory review. We call the reader's attention to the feature issue of J. Opt. Soc. Am. B (January 1985) devoted to instabilities and chaos in active optical media. An international meeting on Instabilities and Dynamics of Lasers and Nonlinear Optical Systems was held at the University of Rochester, 18–21 June 1985. Tutorial papers for the conference will be published by Cambridge University Press. We also recommend the book Chaos, by Hao Bai-Lin (World Scientific Publishing Co., 1984), which consists of an introduction to chaos in both conservative and dissipative systems, a collection of reprinted papers, and an extensive list of references to studies of chaos in various fields.

An interesting development in connection with the stochastic energy growth of driven systems is the work of S. Fishman, D.R. Grempel and R.E. Prange, Phys. Rev. Lett. 49 (1982) 509; Phys. Rev. A29 (1984) 1639. Arguing by analogy with Anderson localization, these authors show that quantum effects tend to suppress the diffusion in phase space predicted classically for certain chaotic systems. This quantum suppression is observed, for instance, in the kicked-rotator model of G. Casati, B.V. Chirikov, F.M. Izrailev and J. Ford. (See Stochastic Behavior in Classical and Quantum Hamiltonian Systems, eds. G. Casati and J. Ford, Springer Lecture Notes in Physics 93 (1979).) The possible implications of chaos for the classical principle of determinism, the ergodic principle, and quantum mechanics have been discussed for nonspecialists by P.W. Milonni in the Proceedings of the Workshop on the Foundations of Physics (University of Puerto Rico, 11–16 March 1985).